

An Investigation of Target Poisoning during Reactive Magnetron Sputtering

Dominik Güttler

April 2009

Wissenschaftlich-Technische Berichte
FZD-515
April 2009

Dominik Güttler

**An Investigation of Target Poisoning
during Ractive Magnetron Sputtering**



**Forschungszentrum
Dresden Rossendorf**

Institut für Ionenstrahlphysik und Materialforschung
Forschungszentrum Dresden-Rossendorf e.V.

An Investigation of Target Poisoning during Reactive Magnetron Sputtering

von der
Fakultät Mathematik und Naturwissenschaften
der Technischen Universität Dresden
genehmigte

Dissertation

zur Erlangung des akademischen Grades
Doctor rerum naturalium
(Dr. rer. nat.)

vorgelegt von
Dominik Güttler

geboren am 18.01.1972
in Marienberg, Deutschland

Dresden 2008

Eingereicht am 18. August 2008

1. Gutachter: Prof. Dr. W. Möller
2. Gutachter: Prof. Dr. J. M. Schneider
3. Gutachter: Prof. Dr. S. Berg

Verteidigt am 12. März 2009

Contents

Abstract	1
1 Introduction	3
1.1 Magnetron sputter deposition	3
1.2 Reactive magnetron sputtering	4
2 Fundamentals of plasma physics	8
2.1 Plasma definitions and classification	8
2.1.1 Definitions	8
2.1.2 Maxwellian energy distribution	10
2.1.3 Debye shielding and Debye length	11
2.2 Collisions in plasmas	12
2.2.1 Collision cross-section	12
2.2.2 Binary elastic collision	13
2.2.3 Main collision processes	13
2.3 Motion of charged particles	16
2.3.1 Constant magnetic field	16
2.3.2 Constant electric and magnetic field	17
2.3.3 Spatial variation of magnetic field	18
2.4 Plasma boundary	19
2.4.1 Electrostatic sheath	19
2.4.2 Plasma potential	22
2.4.3 Sheath potential at a floating wall	22
2.4.4 Negatively biased wall	23
2.5 Plasma surface interaction	24
2.5.1 Ion Bombardment	24
2.5.2 Neutral Bombardment	30
2.6 Low temperature plasmas	31
2.6.1 DC plasmas	31
2.6.2 DC magnetron discharge	33
2.7 Reactive magnetron sputtering	36

3	Modeling of plasma target interaction during reactive sputtering	39
3.1	Plasma modeling	39
3.2	Surface modeling	42
3.2.1	Fluxes towards the target	42
3.2.2	Mechanisms of plasma particles - surface interaction	44
3.2.3	Nitrogen incorporation at the target surface	45
3.3	Modeling of reactive sputtering	47
3.3.1	Gas balance	48
3.3.2	Target balance	49
3.3.3	Substrate balance	52
3.3.4	Reactive gas consumption	53
3.3.5	Results of modeling	54
4	Experimental Setup	60
5	Analysing methods	62
5.1	Ion beam analysis	62
5.2	Mass spectrometry	64
5.2.1	Details of the mass spectrometer	64
5.2.2	Sensitivity of the mass spectrometer	66
5.2.3	Details of operation	67
6	Results and discussion I (Ion beam analysis)	68
6.1	Nitrogen incorporation at target race track	68
6.2	Lateral variation of target poisoning	71
7	Results and discussion II (Mass spectrometry)	75
7.1	Plasma characterization by means of mass spectrometry	75
7.1.1	Appearance of the magnetron plasma	75
7.1.2	Mass spectrum at deposition conditions	75
7.1.3	Behavior of reactive gas partial pressure during sputtering	77
7.1.4	Determination of plasma potential	79
7.1.5	Threshold ionization mass spectrometry of N-radicals	81
7.2	Energy distribution functions of sputtered Titanium	84
7.2.1	Operating details of mass spectrometry	84
7.2.2	Results	85
7.2.3	Discussion	87
8	Conclusions	95
9	Appendix	98
9.1	Abbreviations	98
9.2	Target temperature during magnetron operation	100
9.3	Typical process parameters during magnetron operation	100
9.4	Simulation parameters	101
	List of Tables	102

List of Figures	102
Bibliography	105

Abstract

Objective of the present work is a broad investigation of the so called "target poisoning" during magnetron deposition of TiN in an Ar/N₂ atmosphere. Investigations include real-time in-situ ion beam analysis of nitrogen incorporation at the Ti sputter target during the deposition process and the analysis of particle fluxes towards and from the target by means of energy resolved mass spectrometry.

For experiments a planar, circular DC magnetron, equipped with a 2 inch titanium target was installed in an ultrahigh vacuum chamber which was attached to the beam line system of a 5 MV tandem accelerator. A manipulator allows to move the magnetron vertically and thereby the lateral investigation of the target surface. During magnetron operation the inert and reactive gas flow were adjusted using mass flow controllers resulting in an operating pressure of about 0.3 Pa. The argon flow was fixed, whereas the nitrogen flow was varied to realize different states of target poisoning. In a first step the mass spectrometer was used to verify and measure basic plasma properties e.g. the residual gas composition, the behavior of reactive gas partial pressure, the plasma potential and the dissociation degree of reactive gas molecules.

Based on the non-uniform appearance of the magnetron discharge further measurements were performed in order to discuss the role of varying particle fluxes across the target during the poisoning process. Energy and yield of sputtered particles were analyzed laterally resolved, which allows to describe the surface composition of the target. The energy resolving mass spectrometer was placed at substrate position and the target surface was scanned by changing the magnetron position correspondingly. It was found, that the obtained energy distributions (EDF) of sputtered particles are influenced by their origin, showing significant differences between the center and the erosion zone of the target. These results are interpreted in terms of laterally different states of target poisoning, which results in a variation of the surface binding energy. Consequently the observed energy shift of the EDF indicates the metallic or already poisoned fraction on target surface. Furthermore the EDF's obtained in reactive sputtering mode are broadened. Thus a superposition of two components, which correspond to the metallic and compound fractions of the surface, is assumed. The conclusion of this treatment is an discrete variation of surface binding energy during the transition from metallic to compound target composition. The reactive gas target coverage as derived from the sputtered energy distributions is in reasonable agreement with predictions from model calculations.

The target uptake of nitrogen was determined by means of ion beam analysis using the ¹⁴N(d,α)¹²C nuclear reaction. Measurements at varying nitrogen gas flow directly demonstrate the poisoning effect. The reactive gas uptake saturates at a maximum nitrogen areal

density of about $1 \cdot 10^{16} \text{ cm}^{-2}$ which corresponds to the stoichiometric limit of a $\sim 3 \text{ nm}$ TiN layer. At sufficiently low reactive gas flow a scan across the target surface discloses a pronounced lateral variation of target poisoning, with a lower areal density in the target race track compared to the target center and edge. Again the findings are reproduced by model calculations, which confirm that the balance of reactive gas injection and sputter erosion is shifted towards erosion in the race track.

Accomplished computer simulations of the reactive sputtering process are similar to Berg's well known model. Though based on experimental findings the algorithm was extended to an analytical two layer model which includes the adsorption of reactive gas as well as its different kinds of implantation. A distribution of ion current density across the target diameter is introduced, which allows a more detailed characterization of the processes at the surface. Experimental results and computer simulation have shown that at sufficiently low reactive gas flow, metallic and compound fractions may exist together on the target surface, which is in contradiction to previous simulations, where a homogeneous reactive gas coverage is assumed. Based on the results the dominant mechanisms of nitrogen incorporation at different target locations and at varying reactive gas admixture were identified.

1 Introduction

Thin film and surface techniques have become a key technology, which find places in various fields of modern living today. Thin film products are manifoldly employed and their wide span of applications reaches from microelectronics up to large area optical coatings on architectural glass. All of these areas very often place high demands on quality, precision and an efficient production, so that there is also a wide spectrum of highly developed film deposition methods. Most of these methods are based on depositions from the vapor phase, which can be subdivided into physical and chemical methods. In chemical vapor deposition (CVD) a so called precursor gas reacts at the hot substrate surface and releases the atoms of interest. Physical vapor depositions (PVD) as e.g. thermal evaporation, pulsed laser deposition and sputter deposition are characterized by a locally well defined particle source and a free flight of these particles in vacuum to the substrate. If the vapor from a solid source is created in the presence of a glow discharge or plasma the deposition process is classified as plasma assisted physical vapor deposition (PAPVD). Sputter deposition is such plasma assisted process and a variety of different techniques has been developed in the last decades based on that principle. Sputter deposition has become an established state of the art process for the deposition of a wide range of technological important coatings. Hard and wear resistant coatings as titanium nitride, titanium carbide and boron nitride used to improve the properties of cutting tools or act protective on mechanically stressed machine parts. Transparent conductive oxide (TCO) layers as tin oxide or zinc oxide are used as electrodes in new flat screens and as contacts in solar cells. As a last example large area coatings consisting of titanium oxide, silicon- oxide and nitride and aluminum oxide layer stacks give architectural glasses new optical properties in terms of heat resistivity and reflectivity.

1.1 Magnetron sputter deposition

Sputtering of surface atoms has been discovered already 1852 by W.R. Grove [1] during his investigation of gas discharges but it took a while until its potential for thin film deposition was recognized and most technological application only developed during the last few decades.

During sputter deposition the deposited material is ejected from a cathode (target) under the bombardment of energetic particles. In the PAPVD deposition the primary particle

for sputtering are supplied by a gas discharge which is induced close to the target. The sputtered material condensates at the substrate and forms a thin layer.

Sputter deposition initially played only a minor role compared to e.g. thermal evaporation, due to rather low deposition rates of the technique. It was characterized by low ionization efficiencies in the plasma and often marked by inferior film properties and substrate heating. [2] These limitations have been overcome with the invention of magnetron sputtering. [3–7] In a magnetron discharge high deposition rates are achieved by superposing a magnetic field close to the target. This field confines the motion of secondary electrons to near the target surface and enhances their residence time within the discharge. As a result a higher plasma density at lower inert gas pressure can be achieved in magnetron sputtering, what brings numerous advantages for process efficiency and quality of deposited films. Planar magnetron sputtering has become the most widely used sputtering configuration and magnetrons are used today routinely to rapidly deposit high quality thin films.

The easiness of production of high quality films at high deposition rates is ensured in particular for depositing metal films in the direct current (DC) sputtering mode from elemental, metallic sputter targets. The advantages of magnetron sputtering are summarized: [8]

- The high density plasma from which ions can be extracted results in an enhanced deposition rate with a lower potential on the target than with the DC diode configuration.
- At sufficiently low pressures, sputtered particles are transported from the target to the substrate without gas phase collisions. This results in a high sputtering rate with no thermalization of sputtered particles.
- The method is scalable so that even large areas can be deposited with very good thickness uniformity. The process shows good controllability and long-term stability, which enables a cost efficient deposition on industrial scale.

One disadvantage of the planar magnetron configuration is that the plasma is not uniform over the target surface. Therefore non-uniform deposition conditions in terms of layers thickness and film morphology can be expected on the substrate position. This requires often an additional motion of the substrate with respect to the target. Furthermore the non-uniform plasma leads to a non-uniform target utilization, sometimes with only 30% of the target material being used. For planar magnetron configuration the sputter-erosion path is a closed circle called "race track" (RT). In order to overcome this problem different approaches have been chosen. In one commercial design, the race track configuration is formed on the surface of a rotating tube to give the rotatable cylindrical magnetron. In other designs the magnetic field is moved behind the target.

1.2 Reactive magnetron sputtering

As mentioned above there is a technological demand of numerous compound coatings. These films can be deposited during sputtering of alloy and ceramic targets, respectively. The stoichiometric composition of these targets has to be well defined and adapted to the desired

film composition, what makes these targets rather expensive. Due to different sputtering yields of the elements within the compound target the stoichiometry of the deposited film and of the target may deviate strongly, which may require additionally a lot of experiments before a routinely industrial process can be started.

In the case of a non-conductive compound layer, the positive plasma ions impinging on the target lead to accumulation of charge, which may result in electrical breakdown or arcing. A large part of the discharge current is concentrated then in a small surface volume segment and causes local evaporation. [3] Arcing generally leads to unstable, undefined process condition and may even interrupt the discharge. Furthermore the so ejected macro-particles causes inhomogeneities and defects in the deposited layer, what finally makes a DC magnetron deposition for these materials completely inapplicable.

Charging of the magnetron target can be avoided by means of radio frequency processing (RF), where a rapidly alternating potential is applied to the sputter target. The ion current is interrupted frequently and the target is neutralized by the electron current during the cycle with positive voltage applied. However this method is comparable expensive due to very low deposition rates and higher investment costs. Further the applicability for large area deposition is restricted.

Compound films can be also deposited with the reactive sputtering technique [9–12]. Here an elemental target is exposed to a discharge of inert gas in the presence of some fraction of reactive gases such as oxygen, nitrogen and e.g. methane. The sputtered material reacts on the substrate surface with the reactive gas, which additionally is chemically activated by the plasma. A wide range of compound materials such as oxides, nitrides and carbides can be produced by this technique and the composition of the deposited films can be adjusted by the amount of added reactive gas to the discharge. Two deposition modes can be identified for the process. Sputtering in the metallic mode with low amount of reactive gas added to the discharge often leads to substoichiometric films and sputtering at high reactive gas addition in the compound mode results in stoichiometric or even in over-stoichiometric composition of the deposited film. [13] In the transition the of these two modes process characteristics as discharge voltage, deposition rate and film composition show a complex non-linear behavior. In particular the reactive gas partial pressure may vary one order of magnitude within the process transition. The principles of reactive sputtering will be introduced more detailed in section 2.7.

The process behavior described above and the resulting instabilities are caused by the so called "target poisoning", which means that the compound layer is not only formed at the substrate side as desired but also on the target. The process behavior during reactive sputtering is mainly determined by the conditions of the target surface and its degree of poisoning. The target surface again is influenced by the power and current densities of the discharge as well as by the reactive gas partial pressure, as the balance of plasma species arriving at the target is given by these parameters. The changed target composition in the compound mode generally causes a drastic drop of deposition rate up to a factor of ten. The attempt to deposit stoichiometric films at high rates, however, leads to unstable process conditions since the process has to be driven into the transition region between the metallic and compound operation mode. Therefore various techniques have been developed in order to stabilize the process conditions. [14, 15] Investigations show that a decrease of the target size or an increased throughput of the system vacuum pump act positive on

the process stability. [12, 16, 17] Finally fast feedback control systems measure the partial reactive gas pressure or the plasma composition and adjust the gas inlet very quickly in order to operate with otherwise unstable process parameters. However many of these techniques are nevertheless a limitation for the process, which are practically not applicable or increase the costs for the film deposition. Thus target poisoning still remains a major drawback in reactive sputtering. Therefore, in parallel to the development of stabilization methods, the process of target poisoning itself has become an object of research. Investigations aim to identify the major mechanisms of target - plasma interaction, which are responsible for target poisoning. Further a reliable model of the reactive sputtering process is needed, which predicts important quantities such as deposition rates and film composition as function of the basic input parameters as target power and reactive gas flow. Finally ways may be found to avoid or lower the target poisoning due to an improved understanding of mechanisms and dependencies.

Out of these considerations the aims of the present works arose, as:

- Magnetron discharges are strongly non-uniform. Regions of different plasma densities exist above the magnetron target and therefore the arrival of plasma species and background gas molecules at the target surface varies across the surface. A laterally resolved ion beam analysis (IBA) of the target surface characterizes the degree of target coverage (target poisoning). The comparison of IBA results with the flux variation of plasma ions and reactive gas molecules should allow to identify the main mechanisms of target poisoning which are e.g. direct implantation of reactive gas ions, chemisorption of reactive gas species at the target surface and recoil implantation of adsorbed reactive gas.
- In order to quantify the different mechanisms of target poisoning, the ratio between the different gas species (ions, radicals, neutral molecules) has to be known. Therefore the composition of the reactive plasma has to be determined by mass spectrometry and global plasma modeling. Further the dominating species, which are responsible for target poisoning should be identified. These can be:
 - reactive gas molecules from gas kinetic flux
 - reactive gas radicals
 - reactive gas ions
- A model of reactive sputtering based on particle flux balances of sputtered and reactive gas particles has already been published 1986 [18]. This well established model is still valid and has been developed further in the last years. It is applicable e.g. for the modeling of processing with several reactive gases and for reactive co sputtering. An overview is given in reference [19].
The concentrations of reactive gas and compound material, respectively, as obtained from ion beam investigations of the target surface should be quantified also by modeling of the reactive sputtering process. Therefore the existing model has to be extended. Since the amount of reactive gas incorporation depends e.g. on the target

current density, which is strongly non-uniform for magnetron discharges, a lateral variation of target poisoning can be expected. The model therefore has to contain the ion current distribution across the target surface in order to evaluate the laterally resolved ion beam investigations.

In order to quantify the ion- and radical fluxes from the plasma towards the target surface, global plasma modeling will be accomplished, which describes ionization- and dissociation mechanisms of plasma species. The interaction of these species with the target surface can be depicted by means of TRIDYN computer simulation, from which e.g. the yields of particle implantation and sputtering and thereby the particle flux balances can be derived. The results from both, TRIDYN simulations and global plasma modeling have to be inserted into the modeling of reactive sputtering.

- On the base of the above mentioned experiments, laterally resolved measurements of the amount and the energy distribution functions (EDF's) of sputtered particles may also improve the understanding of plasma-target interaction. Therefore it should be checked if the composition of the target surface can also be characterized by energy resolved mass spectrometry of sputtered particles. Furthermore the EDF's of sputtered particles should be analyzed in order to show how the lateral varying ion current distribution and the lateral variation of target poisoning affects the EDF's.

A variation of reactive gas incorporation across the target would influence the EDF of sputtered particles, as the compound formation results in a variation of the surface binding energy. Further the inhomogeneous plasma itself is a source of laterally varying ion fluxes and possibly ion energies, which may affect the film growth on a substrate. Therefore the present work aims to characterize the sputtered particle fluxes with energy-resolving mass spectrometry.

- Finally an improved understanding of fundamental processes on the target surface during target poisoning as well as an identification of the main poisoning mechanisms and species may open up possibilities to lower or avoid target poisoning.

2 Fundamentals of plasma physics

2.1 Plasma definitions and classification

2.1.1 Definitions

Plasma is often referred to as the fourth state of matter. It is defined as a partially ionized gas consisting of equal numbers of positive and negative charges, hence it is neutral in average ("quasi-neutral"). If the charged particle density is high enough, the particles exhibit collective properties.

In most cases the plasma consists of neutral atoms and molecules, positive ions and electrons. The essential mechanisms in the plasma are excitation and relaxation, ionization and recombination, caused due to collisions of plasma species. The most efficient process of ionization is the collision of electrons and atoms. There is a minimum energy requirement for ionization process to occur, equal to the energy of the most weakly bound electron from the atom, which is the ionization potential.

To sustain a stationary plasma the rate of ionization has to be balanced by a loss of charged particles to the environment and by recombination of ions and electrons. The steady state is characterized by a common charged particle density $n_e \approx n_i \approx n$. The balance of loss rate and ionization defines a mean confinement time of charged particles in the plasma.

Plasma species thermalize due to kinetic energy transfer in elastic collisions. As the mechanism is most efficient for particles with equal masses, the electron and heavy particle ensemble will not thermalize efficiently. This allows to define separate temperatures T_e, T_i and T_n for electrons, ions and neutrals, respectively.

Since the amount of collisions in low pressure plasmas is not sufficiently large and energy transfer between electrons and heavy ions and neutrals, respectively, is very low, no thermalization between both subsystems takes place. Thus heavy particles may even stay close to room temperature, while electrons remain at higher temperatures.

Plasmas with $T_i \approx T_n \ll T_e$ are called **non-thermal**, whereas **thermal** plasmas are characterized by $T_i \approx T_e$.

In plasma physics, particle temperature is mostly expressed by the energy equivalent $k_B T$, with k_B denoting the Boltzmann constant.

$$k_B T = 1 \text{ eV} \cong T = 11604 \text{ K} \tag{2.1}$$

Further classifications of plasmas are with respect to electron temperature, pressure and particle density, respectively. One distinguishes between **low temperature** plasmas, where T_e is in the order of a few eV and **high temperature** plasmas with $T_e > \text{keV}$, **low pressure** plasmas at pressures below $\approx 100 \text{ Pa}$ and **high pressure** plasmas above $\approx 10^4 \text{ Pa}$.

Figure 2.1 identifies different kinds of plasmas over a wide range of densities and temperatures. [20]

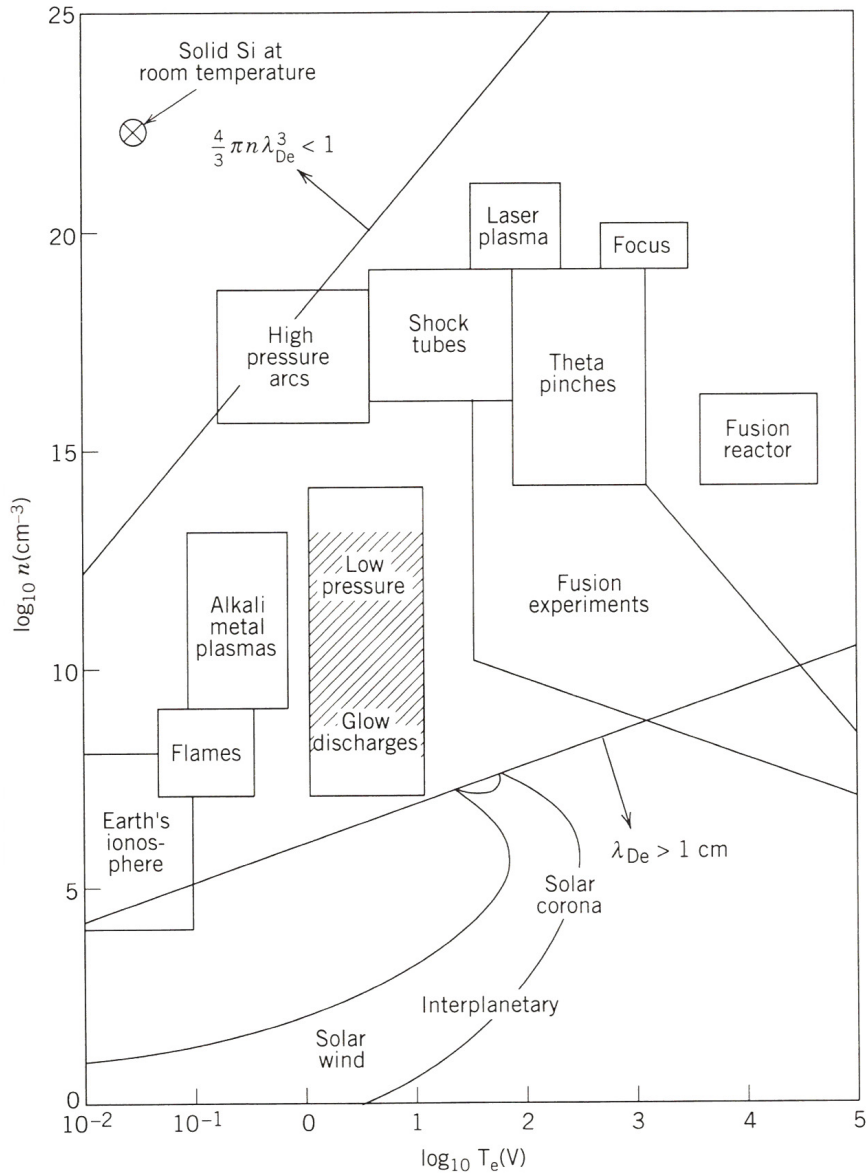


Figure 2.1: Space and laboratory plasmas on a n versus T_e diagram, as taken from reference [20]

As it is shown in fig.2.1, electron temperatures in processing plasmas are in the range of 1 eV - 10 eV for low pressure discharge and around 0.1 eV - 2 eV for high pressure plasmas, respectively. These values are below the ionization threshold of common gases as

Ar ($E_i = 15.8$ eV) and N_2 ($E_i = 15.6$ eV), so that ionization and dissociation occur in processing plasmas through the high-energy tail of the electron energy distribution, which will be discussed in the next paragraph.

2.1.2 Maxwellian energy distribution

The different classifications in terms of plasma temperature are done considering a mean energy or a mean velocity, respectively. Thus plasma species have a distribution of velocities, which can be simplistically characterized by the Maxwellian distribution function. The distribution, which maximizes entropy of the system, is the result of multiple collisions during random motion of particles. The normalized distribution over the three-dimensional velocity space is given by

$$f(\vec{v}) = \left(\frac{m}{2\pi k_B T}\right)^{3/2} \exp\left(-\frac{mv^2}{2k_B T}\right) \quad (2.2)$$

The mean kinetic energy $\langle E \rangle$ and mean velocity $\langle v \rangle$ can be derived from eq. 2.2 and result to

$$\langle E \rangle = \int \frac{1}{2} m \vec{v}^2 f(\vec{v}) d^3 \vec{v} = \frac{3}{2} k_B T \quad (2.3)$$

$$\langle v \rangle = \int \vec{v} f(\vec{v}) d^3 \vec{v} = \sqrt{\frac{8k_B T}{\pi m}} \quad (2.4)$$

Eq. 2.2 can be transformed into the energy distribution

$$\begin{aligned} f(E) &= 4\pi v^2 f(v) \left| \frac{dv}{dE} \right| \\ &= \frac{2}{\sqrt{\pi}} \sqrt{E} (k_B T)^{\frac{3}{2}} \exp\left(-\frac{E}{k_B T}\right) \end{aligned} \quad (2.5)$$

In figure 2.2 the Maxwellian energy distribution is displayed for plasma species (e.g. electrons) at temperatures of $k_B T = 5$ eV and $k_B T = 10$ eV, respectively. The ionization threshold of $E_i = 15.6$ eV is significantly higher than the most probable energy of the electrons at distribution maxima of 2.5 eV and 4.7 eV, respectively. It can be seen that ionization is produced by the high energy tail of the distribution. An integration of equation 2.5 from the Ar ionization energy up to high electron energies show that for $T_e = 5$ eV approximately 10% and for $T_e = 10$ eV approximately 33% of electrons are above the threshold energy.

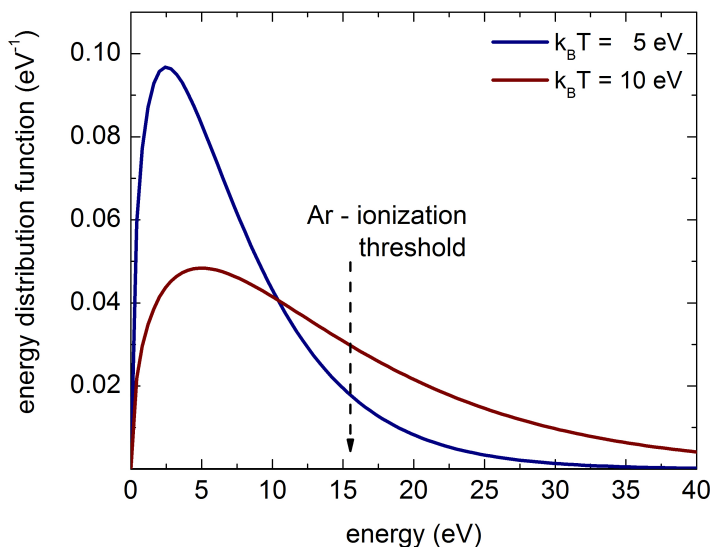


Figure 2.2: Maxwellian energy distribution function for plasma particles with temperatures of $k_B T = 5$ eV and $k_B T = 10$ eV, respectively. The arrow marks the threshold energy, which is required to ionize Ar by electron impact.

2.1.3 Debye shielding and Debye length

Debye shielding is an important collective property of plasma particles which guaranties quasi-neutrality. For a sufficiently high particle density, free charges, especially the more mobile electrons, will move in response to the influence of a particular charge in such a way that their net Coulomb interaction will sum to zero.

Since this mechanism is only true on average the considered linear dimension of the discharge has to be large compared to the **Debye length**, which is a characteristic length scale in a plasma. The Debye length λ_D is the distance over which significant charge densities can spontaneously exist. [6]

$$\lambda_D = \sqrt{\frac{k_B T_e \epsilon_0}{n_e e^2}} \quad (2.6)$$

A particular charge in the plasma interact with all other charged particles only within a sphere with radius λ_D . Outside this sphere, the detailed nature of the interaction becomes immaterial and the net interaction is zero.

Correspondingly, quasi-neutrality is assured, when the number of particles in a plasma is large compared to the number of charged particles in the Debye sphere.

$$N \gg \frac{4}{3} \pi \lambda_D^3 n_e \quad (2.7)$$

Choosing an electron temperature of $T_e = 5$ eV and charged particle densities $n_i = n_e = 10^{10}$ cm³, λ_D has a value of $\approx 1.7 \cdot 10^{-2}$ cm.

2.2 Collisions in plasmas

Even though there exists in general a neutral ground state in technical processing plasmas, which can be described by the gas laws, the prime features of discharges is that of ionization. The different processing plasmas make use of ionization in different ways. For example, in sputtering, the main requirement is a supply of ions, which can be accelerated onto a target surface. In plasma etching a process is needed that dissociates stable gas molecules into chemically active species, which can react with a substrate. So that on one hand particle collisions are desired in plasmas which create these different species, on the other hand collisions are required in order to sustain a stable discharge.

In the following different kind of collisions and collision cross-sections will be discussed, in order to describe plasma properties like ionization degree, and particle transport in plasmas.

2.2.1 Collision cross-section

For a moving particle in an ensemble of identical or different particles with atomic density n , the average number N_C of collision processes in a path length interval Δs is given by

$$\Delta N_C = n\sigma\Delta s \quad (2.8)$$

where σ denotes the collision cross-section and has a dimension of an area.

The mean free path λ_C is the average distance, which a gas atom can travel without any collision with other gas atoms.

$$\lambda_C = \frac{1}{n\sigma} \quad (2.9)$$

The probability $P(s)$ of a gas atom traveling a distance s without any collision becomes

$$P(s) = \exp\left(-\frac{s}{\lambda_C}\right) \quad (2.10)$$

Assuming a target - substrate distance of 5 cm and a mean free path length λ_C of 5 cm for Titanium sputtered in an Ar atmosphere at a pressure of 0.3 Pa gives a probability for a sputtered particle to undergo one collision of

$$P(s) = \exp\left(-\frac{5}{5}\right) = 0.37 \quad (2.11)$$

2.2.2 Binary elastic collision

Collision processes can be divided into elastic and inelastic types. In elastic collisions there is an interchange of kinetic energies only between the colliding partners, whereas in the inelastic type also internal energy changes.

In the simplest assumption, the collisions between plasma particles can be described as binary collisions between hard spheres. Many body interactions can be neglected for the most plasmas, due to large mean free path length.

The energy transfer in an elastic collision of two particles of masses m_i and m_t is given then by conservation of linear momentum and energy. Assume that m_t is initially at rest ($v_t = 0$) and that m_i collides with an velocity v_i and an angle θ , then the conservation of momentum is given by

$$m_i v_i \cos \theta = m_i u_i + m_t u_t \quad (2.12)$$

and the equation for the conservation of energy is

$$\frac{1}{2} m_i v_i^2 = \frac{1}{2} m_i (u_i^2 + v_i^2 \sin^2 \theta) + \frac{1}{2} m_t u_t^2 \quad (2.13)$$

where $u_{i,t}$ denote particle energies after collisions. The fractional energy transferred from m_i to m_t results then in (confer e.g. [6])

$$\frac{E_t}{E_i} = \frac{4m_i m_t}{(m_i + m_t)^2} \cos^2 \theta \quad (2.14)$$

The term $4m_i m_t / (m_i + m_t)^2$ is called the energy transfer factor, which has a maximum of unity when $m_i = m_t$. The efficient energy transfer between particles of equal masses explains the development of Maxwellian energy distribution, where a large amount of colliding particles are thermalized around a mean energy value.

2.2.3 Main collision processes

Each plasma contains electrons, various types of ions, neutral atoms and molecules and photons. In the following the most important interactions in glow discharges between these species are given.

Electron impact ionization

The general character of weakly ionized plasmas is determined by the dominance of electron - neutral collisions.

The electron impact ionization in which the primary electron removes an electron from the atom A and produces an ion A^+ and a further electron, is the most important process in sustaining the glow discharge.

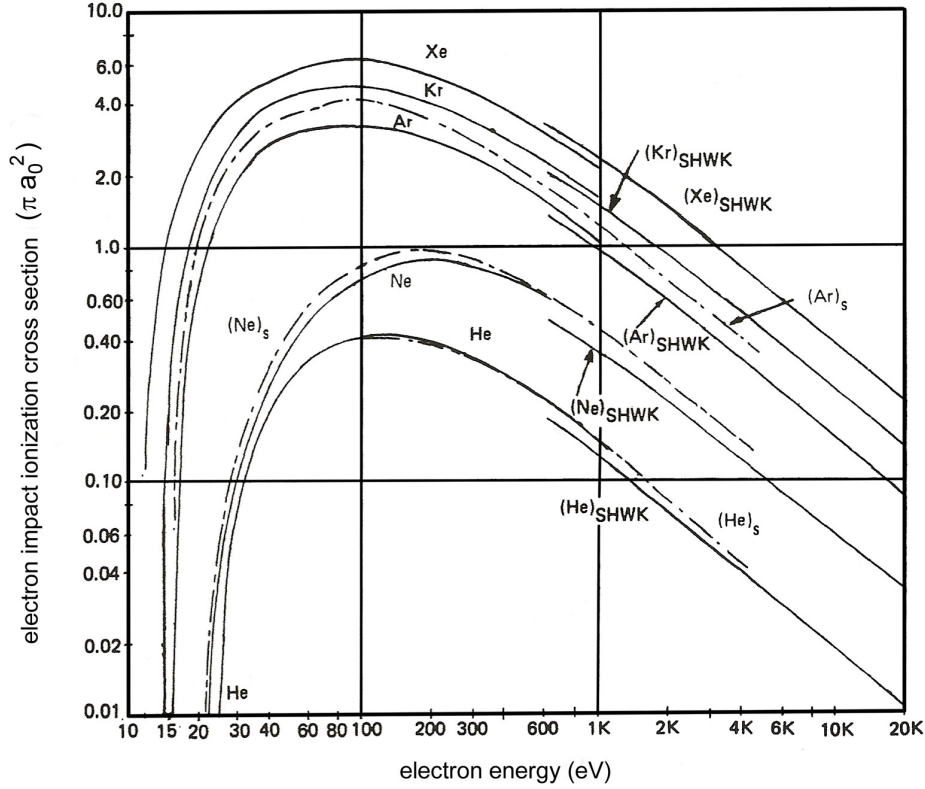


Figure 2.3: Overview of cross sections for electron impact ionization of the noble gases, as taken from reference [6]. Various data have been derived from experiments by Rapp et al. [21], Smith (S) [22] and Schram et al. (SHWK) [23]. ($\pi a_0^2 = 8.82 \times 10^{-17} \text{ cm}^2$) [24]

Figure 2.3 shows the behavior of the ionization cross-section for the noble gases [6]. It can be seen, that there is a minimum electron energy required for an ionization process. This threshold energy is equal to the potential energy of the most weakly bounded electron in the atomic shell. Above the threshold energy, the cross-section raises up to a maximum around 100 eV.

Dissociation

When an electron collides with a molecule, electron impact dissociation according to (2.16) can occur, which also may be accompanied by ionization (2.17). In dissociation processes the breaking apart of molecules AB takes place in the following way





In such reactions chemically reactive radicals and ions are formed which may react to form additional species or undergo surface reactions, as in etching or deposition processes.

Excitation and relaxation

In an excitation process the incoming electron transfers energy, which would enable the knock on electron to jump to a higher energy level within the atom. This process is characterized by quantum absorption of energy.



One of the characteristic features of plasmas is the glow, which is due to relaxation of electronically excited states A^* . These excited states are rather unstable and de-excite inverse to the excitation described above. Each energetic transition is accompanied by the emission of a photon of specific energy equal to the difference ΔE of the atom specific quantum levels. This emission gives discharges of different gases a characteristic color. But the spectroscopy of photons with optical techniques is also a powerful tool in order to detect various chemical elements in the discharge.

Collisions of neutrals

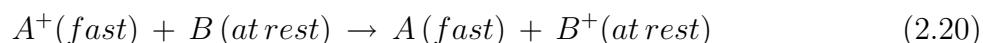
Neutral particles in a plasma are presented by the non-ionized fraction of their parent gas, but may also originate from electron impact dissociation of molecules and from plasma-chemical processes. For the collision of these particles, a hard sphere approximation can be applied. The collision cross-section is given by

$$\sigma = \pi(r_A + r_B)^2 \quad (2.19)$$

where r_A and r_B denote the atomic radii of colliding partners. These cross-sections are typically in the range $(2...5) * 10^{-15} \text{ cm}^2$.

Resonant charge transfer

Resonant charge transfer takes place, when an ion collides with a neutral in particular when the ion is fast compared to the neutral. But also in the boundary layer of a low temperature plasma with low ion energies, the charge transfer cross-section can become very large.



The resonant charge transfer between identical molecules has a lower probability, since many channels of vibrational and rotational excitation of the molecule are existent.

Penning ionization

The penning process



can become a significant ionization mechanism when highly excited, metastable atoms are present in the plasma. The excitation energy of the excited atom has to be higher than the ionization threshold of the collision partner. For the collision of a metastable He atom with an excitation energy of approximately 20 eV, the ionization cross-section of Ar reaches a value of $\approx 10^{-15} \text{ cm}^2$.

2.3 Motion of charged particles

Ions and electrons in a plasma will move in response to electric and magnetic fields. These fields primarily arise from external sources like electrodes and magnets but also result from collisional interaction among the particle.

Particle in the presence of an electric Field \vec{E} and magnetic field \vec{B} with charge q and velocity \vec{v} will experience a force \vec{F} given by the Lorentz equation

$$\vec{F} = m \frac{d\vec{v}}{dt} = q(\vec{E} + \vec{v} \times \vec{B}) \quad (2.22)$$

2.3.1 Constant magnetic field

Suppose a constant magnetic field in \vec{e}_z direction and zero electric field, the axial force in \vec{e}_z direction vanishes and the Lorentz force equation becomes

$$\frac{dv_x}{dt} = \frac{q}{m} v_y B \quad , \quad \frac{dv_y}{dt} = -\frac{q}{m} v_x B \quad \text{and} \quad \frac{dv_z}{dt} = 0 \quad (2.23)$$

Inserting equation 2.23 into 2.23 yields in

$$\frac{d^2 v_x}{dt^2} = \frac{q}{m} \frac{dv_y}{dt} B = \frac{q}{m} \left(\frac{q}{m} v_x B \right) B \quad (2.24)$$

which becomes with the cyclotron frequency

$$\omega_C = \frac{|q|}{m} B \quad (2.25)$$

$$\frac{d^2 v_x}{dt^2} = \omega_C^2 v_x = 0 \quad \text{and} \quad \frac{d^2 v_y}{dt^2} = \omega_C^2 v_y = 0 \quad (2.26)$$

The solutions of equations 2.26 can be written as

$$v_x = -v_{\perp} \sin \omega_C t \quad \text{and} \quad v_y = \pm v_{\perp} \cos \omega_C t \quad (2.27)$$

and finally

$$x = \frac{v_{\perp}}{\omega_C} \cos \omega_C t = r_L \cos \omega_C t \quad \text{and} \quad y = \pm \frac{v_{\perp}}{\omega_C} \sin \omega_C t = \pm r_L \sin \omega_C t \quad (2.28)$$

where

$$r_L = \frac{v_{\perp}}{\omega_C} = \frac{mv_{\perp}}{|q|B} \quad (2.29)$$

is called the Larmor radius which is given by the initial velocity component v_{\perp} perpendicular to the magnetic field.

2.3.2 Constant electric and magnetic field

In the presence of an additional constant and uniform electric field \vec{E} the Lorentz equation 2.22 becomes

$$\frac{dv_x}{dt} = \frac{q}{m}(E_x + v_y B) \quad , \quad \frac{dv_y}{dt} = \frac{q}{m}(E_y - v_x B) \quad \text{and} \quad \frac{dv_z}{dt} = \frac{q}{m}E_z \quad (2.30)$$

with the solutions

$$v_x = -v_{\perp} \sin \omega_C t + \frac{E_y}{B} \quad , \quad v_y = \pm v_{\perp} \cos \omega_C t - \frac{E_x}{B} \quad \text{and} \quad v_z = \frac{q}{m}E_z t \quad (2.31)$$

The path of a charged particle is a combination of uniform circular motion plus a drift velocity, called an $\vec{E} \times \vec{B}$ drift \vec{v}_D .

$$\vec{v}_D = \frac{1}{B}(E_y \vec{e}_x - E_x \vec{e}_y) = \frac{\vec{E} \times \vec{B}}{B^2} \quad (2.32)$$

The drift is directed perpendicular to both, the electric and magnetic field. Further it is independent of the charge and its sign.

2.3.3 Spatial variation of magnetic field

A gyrating charge carries a magnetic momentum μ , which is defined as $\mu = IA$ where the current $I = q/t$ is determined by the charge q and its time for one gyration. A is the area encircled by the charge orbit. A sketch of the magnetic field configuration and the particle orbit is displayed in figure 2.4.

Using equations 2.25 and 2.29, the magnetic momentum is given by

$$\mu = \frac{e}{2\pi\omega_C} \pi r_L^2 = \frac{\frac{1}{2}mv_{\perp}^2}{B} = \frac{W_{\perp}}{B} \quad (2.33)$$

Suppose a particle motion along the magnetic field lines B_z , the total kinetic energy W of the particle

$$W = W_{\perp} + W_z = \text{const} \quad (2.34)$$

is conserved because the magnetic field does no work. This constancy of μ has important consequences in magnetic mirroring of charged particles and in confining the electrons in cyclotron resonance or magnetron discharges.

As B_z increases, W_{\perp} increases to keep μ constant. The increase in W_{\perp} occurs on expense of W_z , thus the particle can be reflected when $W_{\perp} = W$ ($W_z = 0$).

There is an axial force F_z which acts on the center of the particle orbit and retards the spiral motion towards the region of higher B -field. If the particle moves a distance dz , F_z becomes then

$$\begin{aligned} dW_z = F_z dz &= -\frac{W_{\perp}}{B_z} dB_z \\ F_z &= -\mu \frac{dB_z}{dz} \end{aligned} \quad (2.35)$$

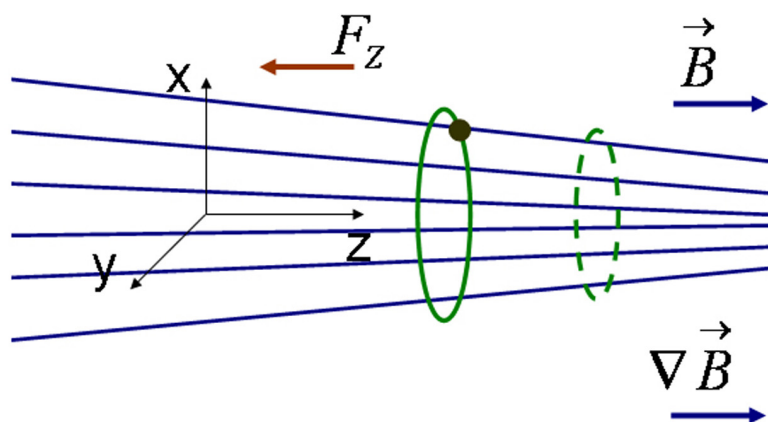


Figure 2.4: Parallel force F_z on a charged particle due to a magnetic field gradient dB_z/dz

2.4 Plasma boundary

In practical plasma devices walls confine the discharge expansion. The analysis of discharge properties at walls and boundaries is important in particular for materials processing because the surface of the material being processed interacts directly with the plasma like a solid boundary.

2.4.1 Electrostatic sheath

Suppose a plasma in front of a wall, which may be part of a vacuum vessel or a substrate. When ions and electrons hit the wall they will be lost from the plasma. As electrons generally have much higher thermal velocities than ions, they will preferentially leave the plasma and charge the plasma slightly positive. As a result an electrostatic potential develops, which retards the electron flux so that only electrons of the high-energy tail of the distribution function still reach the wall. Simultaneously, this potential barrier for electrons accelerates ions, until a new equilibrium state is established, which equalizes electron and ion losses. Because of the shielding that occurs over distances greater than the Debye length, the quasi neutrality within the plasma bulk is not disturbed by the additional potentials. However due to different densities of ions n_i and electrons n_e , the quasi neutrality is no longer fulfilled in the sheath region. The development of an electrostatic sheath is schematically depicted in figure 2.5.

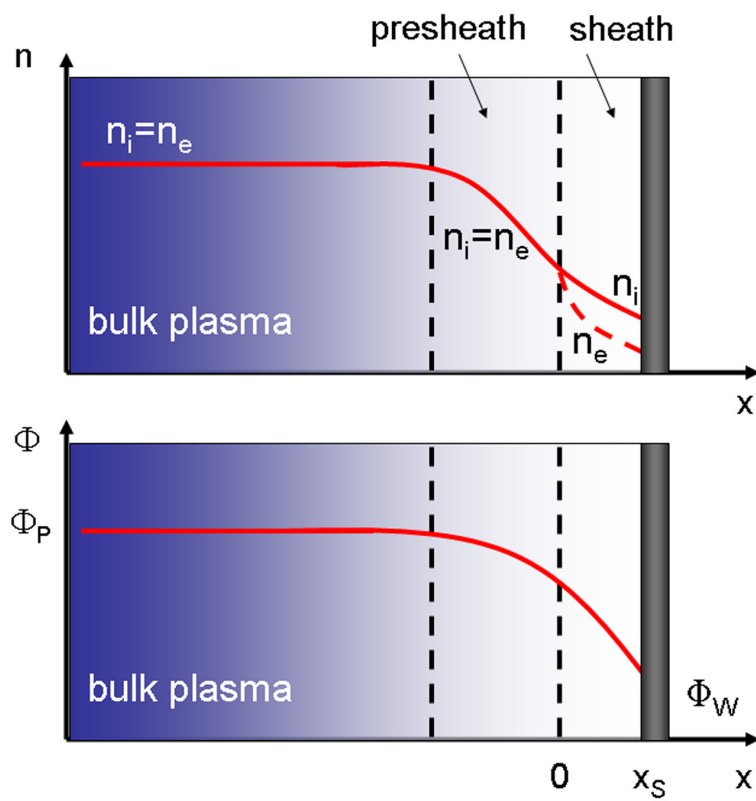


Figure 2.5: Schematic of ion- and electron densities and the electrostatic potential in front of a wall

Assume a collision less sheath the ion energy conservation gives

$$\frac{1}{2}m_i v_{i0}^2 = \frac{1}{2}m_i (v_i(x))^2 + e\Phi(x) \quad (2.36)$$

where m_i is the ion mass, $\Phi(x)$ is the electrostatic potential at position x and v_{i0} is the velocity of ions entering the sheath. The ion continuity equation requires

$$n_{i0}v_{i0} = n_i(x)v_i(x) \quad (2.37)$$

combining these equations gives the ion density $n_i(x)$ at position x

$$n_i(x) = n_0 \sqrt{1 - \frac{2e\Phi(x)}{m_i v_{i0}^2}} \quad (2.38)$$

The electron density is given by the Boltzmann relation

$$n_e(x) = n_{e0} \exp\left(\frac{e\Phi(x)}{k_B T_e}\right) \quad (2.39)$$

In order to find an expression for the potential $\Phi(x)$, from the uncompensated charge in the sheath, Poisson's equation has to be solved

$$\varepsilon_0 \frac{d^2\Phi}{dx^2} = e(n_e - n_i) = e n_0 \left[\exp\left(\frac{e\Phi}{k_B T_e}\right) - \left(1 - \frac{2e\Phi(x)}{m_i v_{i0}^2}\right)^{-1/2} \right] \quad (2.40)$$

In order for the sheath to repel electrons, the potential must be monotonically decreasing with increasing x . This will only be the case if $n_i(x) > n_e(x)$ for all x in the sheath. This condition corresponds to

$$\exp\left(\frac{e\Phi}{k_B T_e}\right) < \left(1 - \frac{2e\Phi(x)}{m_i v_{i0}^2}\right)^{-1/2} \quad (2.41)$$

which becomes for small $|\Phi|$

$$1 + \frac{e\Phi}{k_B T_e} < 1 + \frac{e\Phi(x)}{m_i v_{i0}^2} \quad (2.42)$$

and since $\Phi < 0$

$$\frac{1}{k_B T_e} > \frac{1}{m_i v_{i0}^2} \quad (2.43)$$

The expression

$$v_{i0} \geq v_B = \sqrt{\frac{k_B T_e}{m_i}} \quad (2.44)$$

is the Bohm-criterion. Conservation laws and electrostatics can only be fulfilled if the ions enter the sheath with a velocity equal or larger than the Bohm-velocity v_B . In a low-pressure plasma with $kT_i \ll kT_e$, v_B is much larger than the ion thermal velocity. To give the ions this minimum directed velocity v_B there must be a small finite electric field prior the sheath, where the ions get accelerated. This required region is called the pre sheath.

2.4.2 Plasma potential

Due to the interaction between plasma and wall, the plasma potential Φ_p builds up with respect to sheath boundary (see fig. 2.5). It is responsible for accelerating the ions to the Bohm velocity and can be calculated

$$\frac{m_i}{2} v_B^2 = e\Phi_P \quad (2.45)$$

to

$$\Phi_P = \frac{k_B T_e}{2e} \quad (2.46)$$

which is half the electron temperature when quoted in electron volts.

The density of electrons and ions at the sheath boundary, $x=0$, is then reduced compared to the bulk density and is then found from the Boltzmann relation

$$n_{eS} = n_e \exp\left(-\frac{1}{2}\right) \approx 0.61n_e \quad (2.47)$$

2.4.3 Sheath potential at a floating wall

In stationary state no net current is drawn to a floating wall and electron and ion fluxes balance one another. In absence of any collisions the ion flux through the sheath must be constant and is given by

$$j_i = j_B = n_e v_B \exp\left(-\frac{\Phi_W}{k_B T_e}\right) \quad (2.48)$$

The electron flux at the wall is given by

$$j_{eS} = \frac{1}{4}n_e\langle v_e \rangle \exp\left(-\frac{\Phi_W}{k_B T_e}\right) \quad (2.49)$$

where $\langle v_e \rangle = (8eT_e/\pi m)^{1/2}$ is the mean electron speed and Φ_W is the potential of the wall with respect to the sheath-pre sheath edge at $x=0$.

After substituting for the Bohm velocity from 2.44 and equating the fluxes

$$\sqrt{\frac{k_B T_e}{m_i}} = \frac{1}{4} \sqrt{\frac{8k_B T_e}{\pi m_e}} \exp\left(-\frac{e\Phi_W}{k_B T_e}\right). \quad (2.50)$$

So that solving for Φ_W gives

$$\Phi_W = -\frac{k_B T_e}{2e} \log \frac{m_i}{2\pi m_e} \quad (2.51)$$

Combining equations 2.46 and 2.51, the resulting floating potential is

$$\Phi_{fl} = \Phi_P - \Phi_W = \frac{k_B T_e}{2e} \left(1 + \log \frac{m_i}{2\pi m_e}\right) \quad (2.52)$$

Thus, the energy of ions $E_i = e\Phi_{fl}$ impinging a floating substrate is in the order of 10 eV even if no external voltage is applied to the plasma.

2.4.4 Negatively biased wall

If a high voltage V_0 is applied to an electrode immersed into the plasma the ions will be accelerated by the electric field. Since the applied potential V_0 is large, Φ_{fl} and the initial ion energy can be neglected, in comparison. Equations 2.36 and 2.37 for energy and flux conservation then reduce to

$$\frac{1}{2}m_i(v_i(x))^2 = -e\Phi(x) \quad (2.53)$$

and

$$j_B = en_i(x)v_i(x) \quad (2.54)$$

where j_B denotes the ion current which is constant throughout the sheath. This yields in an ion density

$$n_i(x) = \frac{1}{e} j_B \sqrt{-\frac{2e\Phi(x)}{m_i}}. \quad (2.55)$$

Since the electron density in the sheath can be neglected due to the strong repulsion by the negative potential, Poissons equation can be written

$$\frac{d^2\Phi(x)}{dx^2} = -\frac{1}{\varepsilon_0} j_B \sqrt{-\frac{2e\Phi(x)}{m_i}} \quad (2.56)$$

This finally leads to Child-Langmuirs law of space charged limited flux of charged particles

$$j_B = \frac{4}{9} \varepsilon_0 \sqrt{\frac{2e}{m_i}} \frac{V_0^{3/2}}{x_S^2} \quad (2.57)$$

which describes the current between two electrodes as a function of the potential difference between them. It is confirmed, that the sheath thickness increases with the voltage, whereas the ion flux remains constant. Substituting j_B the shield thickness x_S is given by

$$x_S = \frac{\sqrt{2}}{3} \exp(1/2) \lambda_D \left(\frac{2eV_0}{k_B T_e} \right)^{3/4} \quad (2.58)$$

The expression for the potential in the high voltage shield is

$$\Phi = -V_0 \left(\frac{x}{x_S} \right)^{4/3} \quad (2.59)$$

2.5 Plasma surface interaction

Plasma discharges are used to modify the surface properties of materials and various techniques are applied in which the diverse interaction of several plasma species are utilized. In the following the main mechanisms are discussed, in which plasma species may act on a surface.

2.5.1 Ion Bombardment

Interaction of ions with surfaces

Ions from plasma, which approach the surface of a solid gain in kinetic energy in the potential drop of the plasma sheath. In result one or all of the phenomena displayed in figure 2.6 may

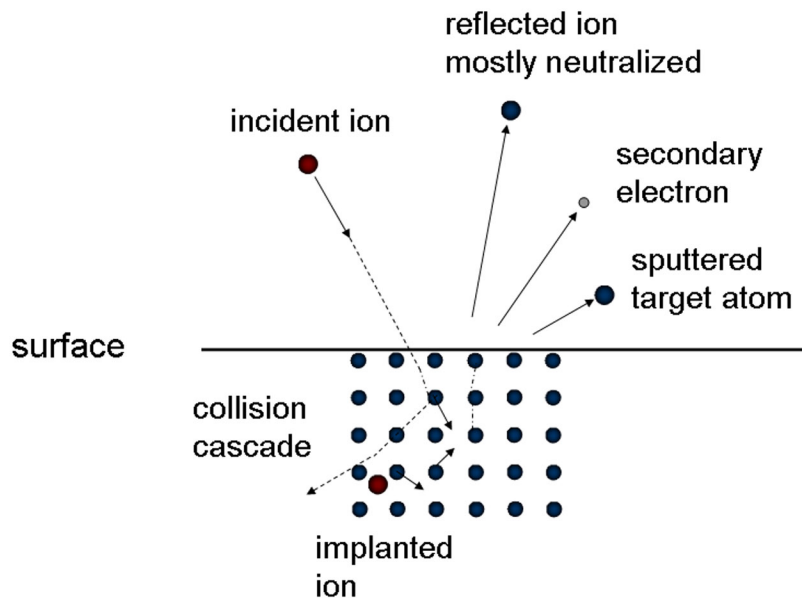


Figure 2.6: Interaction of ions with a surface

occur.

- The ion enters the subsurface region where it loses its energy by collisions with atomic cores and by the interaction with electrons of the solid. The ion finally becomes implanted into the solid subsurface.
- At lower ion energies and especially for light ions the momentum of the ion can get reversed by a subsequence of nuclear collisions, so that the ion leaves the surface again before being stopped.
- The impinging ion may produce secondary electrons, which get repulsed by the applied negative target potential.
- At sufficiently high enough energies the ion impact causes collision cascades in which atoms may be displaced from their lattice sites. Cascade atoms can be ejected through the surface which is called **sputtering**.

Implantation

Ions with high enough kinetic energy (> 100 eV) which impact on a solid can transmit through the solid surface. They interact with the target material through elastic collisions with the screened Coulomb-potential of the atom cores. Furthermore they undergo so-called inelastic interactions with the target electrons. From both processes ions lose energy along their

path. The energy loss per unit path length dE/ds is denoted as stopping cross section S , which is normalized to the atomic density n of the solid material. [25]

$$S = -\frac{1}{n} \frac{dE}{ds} \quad (2.60)$$

Due to above processes the stopping of an ion can be divided into a nuclear and a electronic fraction

$$S = S_n + S_e \quad (2.61)$$

In the energy range and ion-target material combinations most relevant in technical sputtering processes, S_n is dominating, so that S_e can be neglected for these cases.

As a consequence of stopping due to multiple collisions within the solid, each individual incident ion forms a random trajectory see figure 2.7. Stopping of ion is responsible for the total path length but mostly the projected range R_P is of interest since it characterizes the implantation depth with respect to the surface.

For a continuous ion bombardment from the plasma and in particular for shallow implantation depth the implanted ion concentration in the volume increases. Initially, the implantation profile can be described according to

$$c_i(x, \phi) = \frac{1}{n} f_R(x) \cdot \phi \quad (2.62)$$

where c_i is the concentration of implanted ions, $f_R(x)$ denotes the range distribution function and ϕ denotes the implanted ion fluence.

The concentration of the implanted species is mostly limited. So a maximum concentration can be reached when a stoichiometric compound is formed during implantation of reactive species. Furthermore often the maximum inventory of gaseous ions in a solid is limited. Such behavior can be considered by a simple model of local saturation, which assumes that any implanted ion will be released immediately as it becomes implanted into a region where a maximum concentration $c_{i,max}$ has already been reached. The implantation profile is then given by

$$c_i(x, \phi) = \begin{cases} \frac{1}{n} f_R(x) \cdot \phi & : c_i \ll c_{i,max} \\ c_{i,max} & : c_i \geq c_{i,max} \end{cases} \quad (2.63)$$

The profile is schematically displayed in figure 2.8. Above a critical ion fluence, reemission starts since the maximum concentration is reached. A rectangular implantation profile forms into a depth given by the maximum ion range.

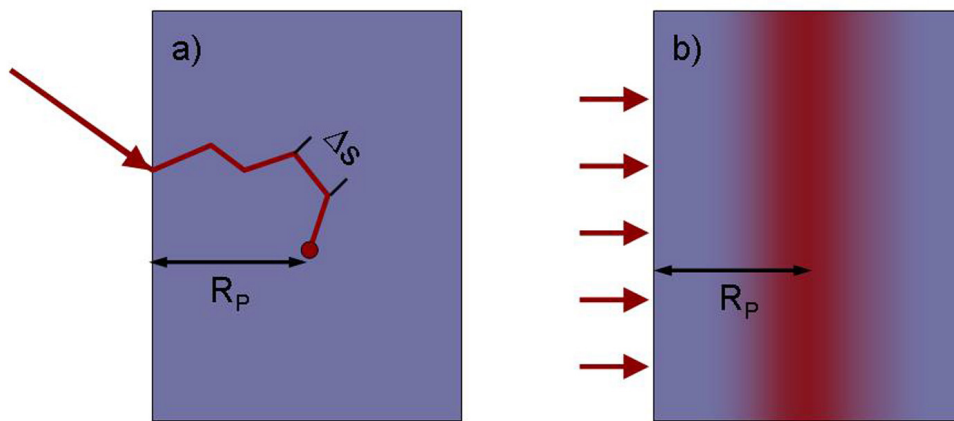


Figure 2.7: a) Schematic of an ion track and b) Schematic of range distribution at normal incidence and projected range R_P

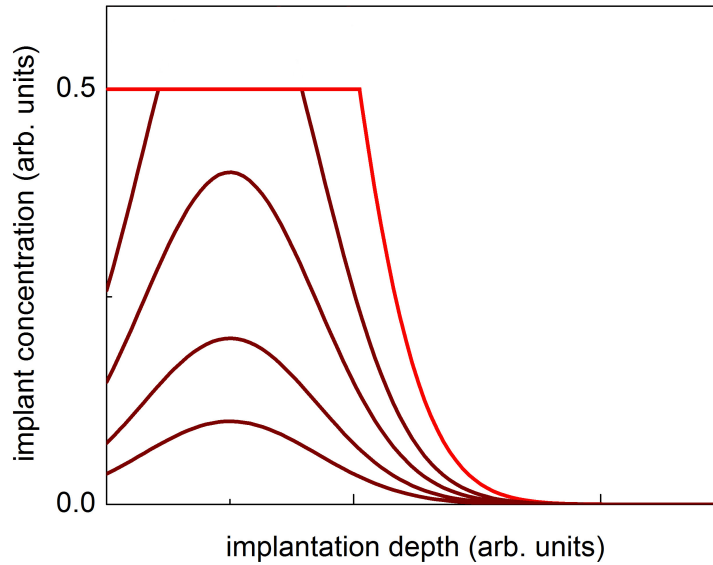


Figure 2.8: Schematic of concentration profile according to the model of local saturation. A Gaussian range distribution has been assumed for four different ion fluences.

Recoil implantation

Fast ions transfer their energy in nuclear collisions to the atoms of the material, thus creating recoil atoms. If the transferred energy is sufficiently large, these primary recoils will move along a trajectory similar to that of the incident ion and may again undergo collisions. At sufficiently large energies collision cascades are generated by multiple recoil collisions. As a result, the recoil atoms will be transported deeper into the material, where it finally comes to rest according to its initial energy. A relation between the incident ion energy and number of displaced recoil atoms in atomic collisions can be found e.g. in reference [26].

Sputtering

Sputtering is the ejection of target atoms under the influence of impinging high energetic ions. The process requires a momentum reversal, which is often realized in a series of binary collisions between the target atoms. Furthermore ejected atoms need to have a minimum initial energy to overcome the surface binding energy. The surface binding energy can be approximated by the sublimation enthalpy of the solid U_S , with values between 2 eV and 8 eV for elemental solids.

The sputtering yield can be defined as the ratio

$$Y_S = \frac{j_s}{j_i} = \frac{\text{sputtered particle flux}}{\text{incident ion flux}} \quad (2.64)$$

Derived from transport theory the Sigmund formula for the sputtering yield is [27]

$$Y_S(E_0) = \frac{4.2 \cdot 10^{14} \text{ cm}^2}{U_S} \cdot \zeta\left(\frac{m_t}{m_i}\right) \cdot S_n(E_0) \quad (2.65)$$

where $\zeta(m_t/m_i)$ a function of the target-to-ion mass ratio, varies from 0.15 to 0.8. $S_n(E_0)$ is the initial nuclear stopping of the incoming ion in the target material.

Energy distribution of sputtered particles

Generally all sputtered particles are neutralized, so that they will not gain in or lose energy within the plasma sheath. Thus their energy E_S is given by the probabilistic nature of sputtering process. The resulting energy distribution of sputtered atoms can be described by the Thompson formula [28, 29]

$$f(E_S) \propto \frac{E_S}{(E_S + U_S)^3} \quad (2.66)$$

As it is shown in figure 2.9 the energy distribution of particles, sputtered from a solid with $U_S=8$ eV, peaks at an energy $E_S = U_S/2=4$ eV and exhibits a long high energy tail.

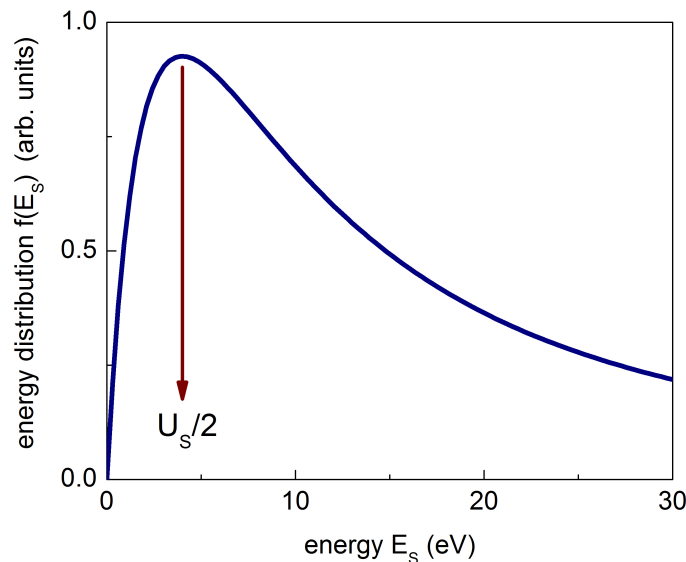


Figure 2.9: Energy distribution of sputtered atoms according to the Thompson formula. The energy distribution peaks at an energy of $U_S/2$ and exhibits a long high energy tail

2.5.2 Neutral Bombardment

At the pressures appropriate in technical plasma applications the mean free path length of gas molecules is in the order of the dimensions of the vacuum system. The surfaces are affected by frequent gas collisions, thus the gas-surface interaction plays an important role for process behavior.

Assume the Maxwellian velocity distribution $f(\vec{v})$ (see eq. (2.2)) of the molecules, the gas kinetic flux j_g to a surface can be derived from kinetic gas theory. The flux per unit area is

$$j_g = \frac{1}{4}n\langle v \rangle \quad (2.67)$$

where n is the particle density and $\langle v \rangle$ is the mean particle speed (cf. eq. (2.4)). With the partial pressure p_g of the gas species

$$p_g = nk_B T \quad (2.68)$$

the resulting flux j_g becomes

$$j_g = \frac{p_g}{\sqrt{2\pi m_g k_B T}} \quad (2.69)$$

where the index g stands for a certain gas species, e.g. the inert gas or a reactive gas within the plasma. The partial pressure and the atomic (molecular) mass of the respective gases are denoted with p_g and m_g , respectively.

The flux j_g sets an upper limit on the rate at which material can accumulate on the surface. The attachment of atoms or molecules on the surface of a solid is called adsorption, while desorption is the reverse process. Adsorption again is generally classified as **physisorption**, where the adsorbate adheres to the surface only through weak intermolecular Van der Waals forces, and **chemisorption**. Chemisorption is characterized by a stronger, covalent bond between adsorbate and surface. Both processes mostly occur only up to one monolayer.

Gas species impinging on a solid surface can only be trapped if their energy is low enough. In order to express the probabilistic nature of the gas-surface interaction, the amount of adsorbed molecules can be written as $S \cdot j_g$. S , which is confined between 0 and 1, is called the sticking coefficient. Generally S is a function of the temperature, the surface roughness and the surface compound fraction θ .

The surface adsorption can be described with the Langmuir kinetics [30]. Here the adsorption is proportional to the extent of the uncovered surface fraction $(1 - \theta)x$. Thus it is common to introduce a initial sticking coefficient S_0 with the relation $S = S_0(1 - \theta)$.

A general function of a coverage dependent sticking coefficient was formulated by Kisliuk [31, 32] and is given by

$$S = S_0 \left(1 + k \frac{\theta}{1 - \theta} \right)^{-1} \quad (2.70)$$

which becomes the Langmuir kinetics for $k = 1$. For $k < 1$ equation 2.70 reflects the experimental findings for the sticking of low energetic molecules [33]. Figure 2.10 shows the sticking function of eq. 2.70 for different parameters k .

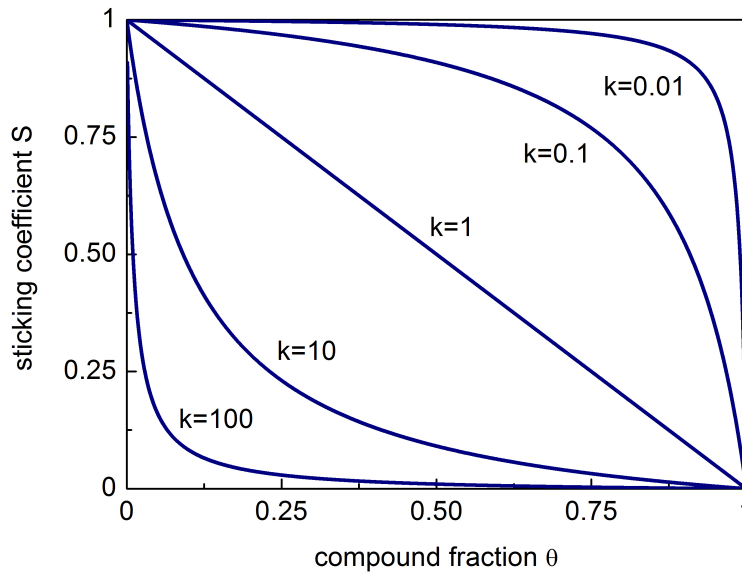


Figure 2.10: Sticking coefficient as a function of compound surface fraction θ for different values of k .

2.6 Low temperature plasmas

2.6.1 DC plasmas

A simple way to produce a glow discharge is by applying a potential between two electrodes, which are placed inside a vacuum vessel. At certain conditions for the gas pressure and the applied voltage a plasma can be established through an avalanche like ionization of gas neutrals. This ionization processes require the initially existence of electrons, which naturally occur by e.g. cosmic radiation. The electric field between the electrodes will accelerate the electrons towards the anode and as a result the electrons gain sufficient energy to ionize the gas atoms. This will lead to a multiplication of the number of electrons, which can be described by the Townsend's first ionization coefficient α . It represents the relative increase in electron flux j_e per unit path length.

$$dj_e = \alpha j_e dx \quad (2.71)$$

with the solution

$$j_e(d) = j_e(0) \exp(\alpha d) \quad (2.72)$$

which determines the current arising from an electron current $j_e(0)$ emitted from the cathode at position $x=0$. An electron production which is necessary for a maintenance of the discharge is continuously provided by ion-induced production of secondary electrons during the ion impact at the cathode. With the secondary electron emission coefficient (SEEC) γ_e , the electron production can be written as

$$j_e(0) = \gamma_e j_i(0) \quad (2.73)$$

As one ion is also produced in the cascade with each electron

$$j_i(0) - j_i(d) = j_e(d) - j_e(0) = j_e(0)(\exp(\alpha d) - 1) \quad (2.74)$$

The Townsend coefficient α can also be interpreted as net ionization probability per unit path length multiplied by the probability that the collision will generate ions. Thus α can be written as

$$\alpha = \frac{1}{\lambda} \exp\left(\frac{-U_i}{\lambda e E}\right) \quad (2.75)$$

where λ denotes the collision mean free path and $\lambda e E$ is the energy gained by electrons between the collision.

Since the mean free path is inversely proportional to the gas pressure $\lambda \propto p^{-1}$, α becomes

$$\alpha = A p \exp\left(-B \frac{pd}{V}\right) \quad (2.76)$$

Here, A and B are constants which depend on the gas. The electric field E was replaced by the applied Voltage V and by the distance d between electrodes.

For a condition referred to as breakdown the electron multiplication is very efficient and $j_e(d)$ becomes much larger than $j_e(0)$. The ion flux at the anode $j_i(d)$ can be neglected than on the left hand side of equation 2.74 and the breakthrough condition results as

$$\alpha d = \log\left(1 + \frac{1}{\gamma_e}\right) \quad (2.77)$$

Together with equation 2.76 the breakdown voltage V_B yields in

$$V_B = \frac{Bpd}{\log(Apd) - \log\left(\log\left(1 + \frac{1}{\gamma_e}\right)\right)} \quad (2.78)$$

which is known as Paschen's law. The breakdown voltage depends on the product of pressure p and electrode distance d and weakly with the cathode material, which defines the SEEC. For large products of pd , the breakdown voltage V_B is proportional to pd , the electric field must scale linearly with the pressure. For very small products pd , there are only few collisions and V_B must rise in order to increase the probability of breakdown per collision. A plot of the Paschen law is shown in figure 2.11. The minimum voltage required for an ignition of the discharge is called the Paschen minimum which can be found at a pressure-distance product

$$pd|_{V_{min}} = \frac{1}{A} \log\left(1 + \frac{1}{\gamma_e}\right) \quad (2.79)$$

2.6.2 DC magnetron discharge

As it is shown in figure 2.11 the pressure required to maintain a plasma in a simple two-electrodes system is rather high. This limits the setup for applications like thin film deposition techniques by sputtering. The higher pressure and hence the reduced collision mean free path represents disadvantages for the process, since sputtered atoms get scattered away on their path to the substrate which reduces the deposition rate. Furthermore sputtered particles suffer an energy loss in collisions which deteriorates the film properties in many cases.

In order to increase the probability for electron impact ionization at simultaneously reduced pressure magnetron sputter systems were developed. In such configurations a magnetic field is superposed transversal to the electric field, what creates a electron trap. The electrons are confined by the magnetic field. A lot of magnetron designs have been continuously developed and figure 2.12 shows only one of possible configuration, which represents a planar cylindrical DC magnetron. Two permanent magnets below the cathode, one cylindrical magnet in the center and a ring shaped outer magnet create a magnetic field in a geometry similar to a half torus. Above the cathode (magnetron target) the $\vec{E} \times \vec{B}$ field yields to a gyration of electrons around the magnetic field lines connected with a drift motion around the target center (cf. equations (2.29) and (2.32)). Applying a DC voltage of a few 100 V the plasma can be ignited and a bright plasma ring appears above the cathode, which is embedded into a plasma of lower density.

The lower working gas pressure which can be reduced by a factor in the order of 10 compared to a simple diode discharge will avoid the scattering of sputtered atoms. Furthermore ions from the plasma gain in the full energy according to the target voltage, when trespassing the cathode sheath without any collision. This increases not only the sputter yield but also the production of secondary electrons. These electrons are accelerated back into the plasma, get trapped by the magnetic field according to the Lorentz force (see eq. (2.22)) and lose their energy by collision with gas atoms. Again with an energy according to the cathode voltage, electrons are able to create a number

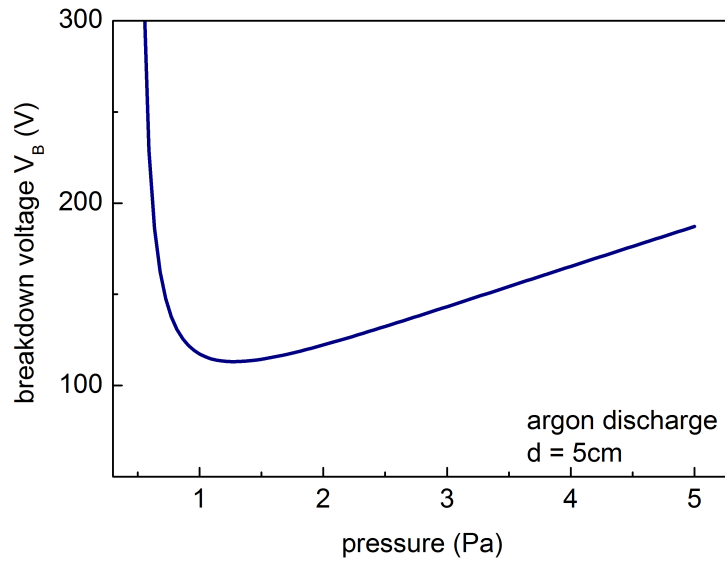


Figure 2.11: Paschen law of the breakdown voltage V_B as function of the pressure. The distance between the electrodes is 5 cm. For an argon discharge $A=1.02 \text{ (Pa cm)}^{-1}$ and $B=17.7 \text{ V (Pa cm)}^{-1}$. The SEEC is assumed to be 0.1 which is typical for a dc discharge.

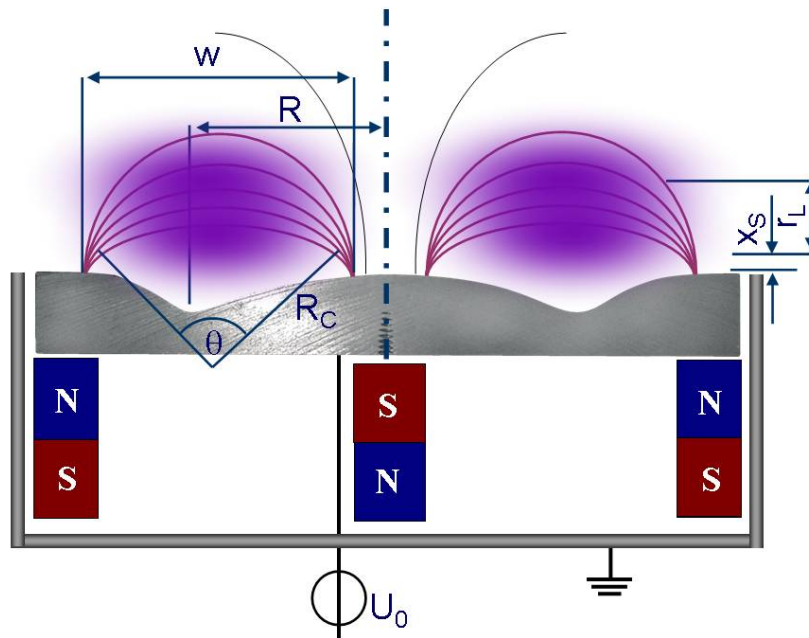


Figure 2.12: Schematic of a planar cylindrical DC magnetron. The applied cathode (target) voltage accelerate the ions, which are increasingly produced in the plasma ring above the cathode. Target atoms get sputtered by this ion bombardment and condense at the substrate surface opposite the target (not shown).

$$N = \frac{eV_0}{U_{i,eff}} \approx \frac{eV_0}{2U_i} \quad (2.80)$$

of ion-electron pairs. $U_{i,eff}$ denotes the average amount of energy spent per ionization event. It is about twice the ionization potential since electrons also lose energy by other processes than ionization within the plasma. Furthermore some of the electrons strike back at the target before losing their full energy, which is accounted for by an effective SEEC. A estimation yields

$$\gamma_{e,eff} \approx \frac{\gamma_e}{2} \quad (2.81)$$

Assume that all created ions leave the plasma towards the target. Then in stationary state, the number of ions produced per unit time is equal to the ion current I_i at the target.

$$I_i \gamma_{e,eff} N = I_i \quad \text{or} \quad \gamma_{e,eff} N = 1 \quad (2.82)$$

Together with equations (2.80) and (2.81) this yields to an estimation for the target voltage

$$V_0 \approx \frac{4U_i}{e\gamma_e} \quad (2.83)$$

which is about 600 V assuming an ionization potential of 15 eV and a typical SEEC of 0.1. The voltage is higher by a factor of about 2 as observed in experiments, which is partly due to the fact that additional ionization by thermal electrons is neglected above. Furthermore the assumption of steady state ion balance in equation (2.82) does not take into account any flux of ions towards the surrounding walls.

The gyro radius of the electrons r_L determines the axial extension of the plasma ring and can be calculated according to equation (2.29)

$$r_L = \frac{v_e}{\omega_{C_e}} = \frac{1}{B} \sqrt{\frac{2m_e V_0}{e}} \quad (2.84)$$

A magnetic field of 200 mT and a voltage of 300 V results in a gyroradius of about 1 cm for electrons and a radius of about 3 m for ions.

Referring to figure 2.12 the mean height of the plasma ring is equal to the gyration radius. The limiting field line can be approximated by a circle segment with an opening angle θ and radius R_C

$$\sin \theta/2 = \frac{w/2}{R_C} \quad \text{and} \quad r_L + R_C \cos \theta/2 = R_C \quad (2.85)$$

Combining these two expression yields a width of the plasma ring

$$w = 2\sqrt{r_L(2R_C - r_L)} \quad (2.86)$$

The ions are almost uninfluenced by the magnetic field, as shown in equation (2.84) and a typical operating pressure of 0.5 Pa allows to utilize the collisionless Child-Langmuir law (eq. 2.57) to describe the ion flux towards the magnetron target. On the other hand, from geometry considerations above the ion flux j_i is given by

$$j_i = \frac{I_i}{2\pi e R w} \quad (2.87)$$

as the current I_i is only determined by the ion flux to the cathode and the SEEC is small. With the parameters $I_i=0.3$ A, $R=1.3$ cm and $w=2$ cm the resulting average current density j_i is about 6 mA/cm².

The ion density n_i within the plasma ring can be estimated using the Bohm-flux (eq. (2.44)) and inserting $j_i= 50$ mA cm⁻² and an electron temperature of 1 eV, both as obtained from experiments (see sections 3.2.1 and 7.1.4).

$$n_i = \frac{j_i}{0.61 e v_B} \quad (2.88)$$

yields in an ion density above the erosion zone of $n_i \approx 3 \cdot 10^{12}$ cm⁻³, which is a typical value for low pressure discharges, in particular when considering the region of magnetic electron confinement.

2.7 Reactive magnetron sputtering

Metallic thin films can easily produced by sputtering metal targets in a DC discharge. Though this method is not feasible if compound materials or dielectrics should be fabricated, since sputtering of compound and in particular dielectric materials would charge the target. This would disturb the deposition process decisive or may finally stop the DC discharge. In order to avoid target charging, compound materials are sputtered in radio frequency (RF) discharges. This method requires additional equipment and exhibits, compared to DC sputtering lower deposition rates, due to the applied power pulses. Furthermore compound materials possess in general higher surface binding energies and, thereby a reduced sputter yield.

Reactive DC [3, 9–12, 14, 34] sputtering instead is a very common and efficient method for deposition of compound materials, such as oxides, nitrides and ceramics. The deposition takes place here through sputtering of elemental or alloyed targets in a working gas that contains a reactive gas component (e.g. O₂, N₂, C₂H₂). The resulting thin film is a compound formed from sputtered target material and the reactive gas. During deposition, the plasma itself becomes a chemically active environment, where the excitation of reactants takes place.

Advantages of reactive sputtering from elemental targets are attributed to several factors

- Insulating films can be deposited in a DC discharge at a high rate and on an industrial scale [35–37] without the need of complex and expensive RF systems.
- It is possible to produce a wide range of thin compound films of controllable stoichiometry and composition [38] by varying the reactive gas partial pressure.
- Elemental targets are usually more easily purified, hence higher quality films become available at lower prices.
- A higher thermal conductivity of metallic target allows an efficient cooling and, thereby to extend the applied power. This makes the process scalable for different applications.

Despite of the simplicity of the concept, reactive sputtering is a complex and non-linear process. For the deposition of high quality coatings with defined stoichiometry, parameters like the particle density in the stream of sputtered material, the reactive gas partial pressure (p_{rg}) and the plasma density must be kept as constant as possible. However, reactive sputtering is impeded by the effect of target poisoning, which means that a compound film is not only formed on the substrate as desired, but also on the sputter target. This results in a significantly reduced sputter yield of the target material and influences the major process parameters. According to the condition of the target surface, in particular of the erosion zone, two different stable operating modes of the magnetron discharge exist, the metallic mode and the compound mode. The transition between these two states is associated with an unstable operation regime and a hysteresis of the reactive gas partial pressure (and deposition rate) at increasing/decreasing reactive gas flow. Figure 2.13 shows schematically the operating modes during reactive sputter deposition at constant power and constant partial pressure of inert gas.

The metallic mode is characterized by a high deposition rate and thereby a high reactive gas consumption. The gettering rate by the sputtered metal is higher than the reactive gas flow rate into the sputtering chamber and hence all available reactive gas is consumed. At increasing reactive gas flow no change in p_{rg} can be observed in figure 2.13. Typically sputtering in this regime leads to understoichiometric films.

When the reactive gas flow reaches the critical value (b), the available reactive gas exceeds the rate of sputtered metal. The reactive gas covers then the target surface and a gas-metal compound forms, which has a higher surface binding energy than the pure metal. As a consequence the sputtering yield drops and again less reactive gas will be consumed, so that p_{rg} increases rapidly up to point (c). A further increase of reactive gas flow leads to a linearly response of p_{rg} . Decreasing now the reactive gas flow and following the red arrow in figure 2.13, p_{rg} decreases linearly beyond point (c). This is because the sputter yield and thereby the reactive gas consumption of the still poisoned target is low, so that p_{rg} remains high even at a lower gas flow, compared to the metallic mode (green arrow). Only at point (d) p_{rg} is low enough, that the compound layer at the target becomes removed through sputtering.

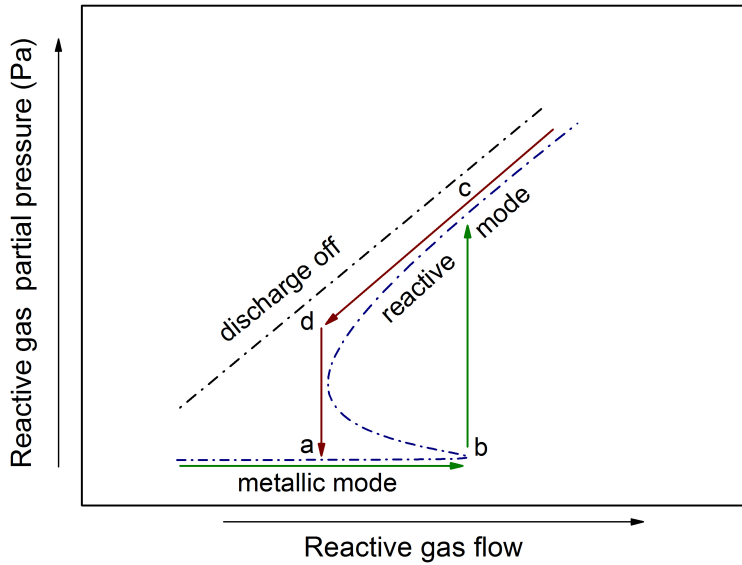


Figure 2.13: Schematic of the hysteresis behavior of reactive gas partial pressure during the increase (green arrows) and decrease (red arrows) of reactive gas flow, as obtainable for magnetron sputtering without any process stabilization. The blue, dashed-dotted line shows the theoretical behavior of reactive gas partial pressure and the black, dashed-dotted line represents the partial pressure with the discharge switched off.

The sputtering yield of the target and thereby the gas consumption increases and causes a sudden drop in p_{rg} (point (a)).

The points (a,b,c,d) confine the hysteresis area, which is characterized by unstable process conditions [39]. Within this area e.g. p_{rg} may jump between two or three values at one certain reactive gas flow value, what makes the deposition of qualitative defined layers, without any means of process control, impossible. Therefore several attempts have been made to stabilize the process in the transition mode and reduce the hysteresis effect. Process stabilization allows to fabricate thin films of a specified stoichiometry in the otherwise forbidden range of reactive gas flow between points (a) and (b). [12,14,15,38]. However target poisoning still remains a major problem in reactive sputtering, since the various techniques of process stabilization always increase the industrial costs in thin film production [3,34].

3 Modeling of plasma target interaction during reactive sputtering

3.1 Plasma modeling

The present section will introduce simple plasma modeling, which allows to quantify the inert and reactive gas particle fluxes from the plasma towards the magnetron target. The results will be employed in chapter 3.3 as input quantities for modeling of reactive sputtering.

The plasma model introduced here can be also found in reference [43]. The stationary global model describes the ion and radical fluxes, which impinge on the target surface of a cylindrical planar DC magnetron. Referring to the typical geometrical appearance of a magnetron discharge, shown in figure 2.12, the plasma is approximated in the model by a homogeneous ring above the target. Within this ring ionization and dissociation of gas species result mainly from fast electrons, which are generated at the target by ion induced secondary electron emission. These electrons are accelerated in the electric field of the magnetron target, which is given by the operation voltage V_t of the magnetron plus a small contribution of the plasma potential (see section 7.1.4). Reactions from thermal electrons are neglected in the model, since their contribution is less than 10%. The accelerated electrons are captured by the magnetic field of the magnetron. They spiral along the magnetic field lines and lose their energy by subsequent collisions with the inert and reactive gases. The possible electron-impact reactions for inert and reactive gases are shown in table 3.1.

For each reaction of type r the number of events along the path of one electron is given by

Table 3.1: Electron-impact reactions with their threshold energies and corresponding references for the cross section data

No.	Reaction	Threshold energy (eV)	Ref.
1	$\text{Ar} \rightarrow \text{Ar}^+$	15.8	[40]
2	$\text{Xe} \rightarrow \text{Xe}^+$	12.1	[21]
3	$\text{N}_2 \rightarrow \text{N}_2^+$	15.6	[41]
4	$\text{N}_2 \rightarrow \text{N}^+ + \text{N}^0$	24.4	[40]
5	$\text{N}_2 \rightarrow \text{N}^0 + \text{N}^0$	9.8	[42]

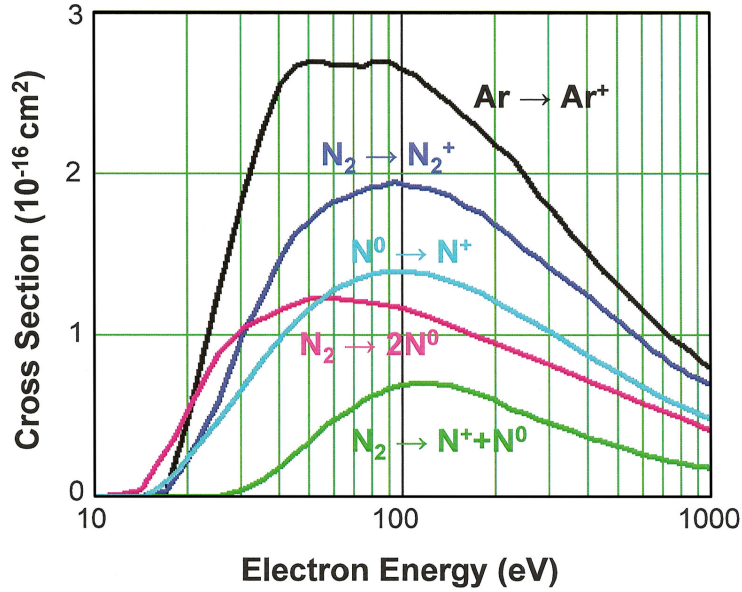


Figure 3.1: Cross section for electron impact ionization and dissociation of Ar and N₂, respectively, versus electron energy. The data were taken from references listed in table 3.1

$$N_r = \int n_r \sigma_r(E) dl \quad (3.1)$$

where n_r denotes the atomic density of gas species (Ar, Xe or N₂) and $\sigma_r(E)$ is the reaction cross section as a function of the electron energy E , which decreases along the path l of the electron. Figure 3.1 shows the progression of σ_r versus the electron energy for different gas species. The data were taken from the references listed in table 3.1.

It is more appropriate now to transform integral (3.1) from path length into an energy integral. This yields

$$N_r = n_r \int_{E_r^{th}}^{eV_t} \left(\frac{dE}{dl} \right)^{-1} \sigma_r(E) dE \quad (3.2)$$

where the integration extends from the initial electron energy eV_t down to the threshold energy E_r^{th} of the respective reaction. dE/dl denotes the energy loss of the electron per unit path length, which is given by the energy transfer in each possible reaction. With the average energy transfer $T_i(E)$ for the reaction i at the electron energy E it is

$$\frac{dE}{dl}(E) = \sum_{all\ i} n_i T_i(E) \sigma_i(E) \quad (3.3)$$

A rough approximation of the energy transfer per reaction is $T_i(E) = 2E_i^{th}$ [20] and by

combining equations (3.1) - (3.3) the number of events per electron becomes

$$N_r = n_r \int_{E_r^{th}}^{eV_i} \frac{\sigma_r(E)}{\sum_{all\ i} n_i T_i(E) \sigma_i(E)} \quad (3.4)$$

The individual ion flux, resulting from the ion production process r , is given than by the expression

$$j_r^{ion} = \gamma_{eff} j_{ion}^{tot} N_r \quad (3.5)$$

where $\gamma_{eff} j_{ion}^{tot}$ expresses the flux of electrons into the plasma. The secondary electron emission coefficient (SEEC) γ_{eff} is assumed to be independent of the impinging ion species. j_{ion}^{tot} the total ion flux to the target is known from the experiment. Assuming that all created ions are accelerated towards the target, the summation over all ion species yields in the self-consistency relation

$$\gamma_{eff} \cdot \sum_r N_r^{ion} = 1 \quad (3.6)$$

The index $r=1,3,4$ and $r=2,3,4$ stands for for the Ar/N₂ and Xe/N₂ discharges, respectively (see table 3.1). Since this relation defines the effective SEEC at given target voltage and gas consumption, no further knowledge about the secondary electron emission, which strongly depends of the surface composition, is required.

The analog to equation 3.5 for the N^0 radicals, which are created through dissociation and dissociative ionization, respectively, finally reads

$$j_{N^0} = \frac{\gamma_{eff}}{2} (2N_4 + N_5), \quad (3.7)$$

with the reasonable assumption, that about half of the generated radicals arrive at the target surface.

In accordance with the experiments, which will be introduced in chapter 6, a total gas pressure of 0.3 Pa and a nitrogen addition between 0% and 25% was applied in the modeling. Further a target voltage of 350 V and an average target current of 15 mA/cm² was inserted into the model. Any variation of target voltage due to the addition of nitrogen has been neglected. From equation 3.6 an effective SEEC of around 0.1 for the Ar/N₂ gas mixture was found, which is in agreement with literature [20, 44]. For the Xe/N₂ discharge plasma modeling yields an effective SEEC of $\gamma_{eff} \sim 0.045$ which is lower than for the Ar/N₂ system by roughly a factor of two. The lower SEEC corresponds to an increased target voltage during magnetron operation, which can be observed in experiments (see sec. 6.1). Furthermore the different values of γ_{eff} are in qualitative agreement with literature, where a decreasing SEEC at increasing ion mass is reported. [20, 45] These first results already demonstrate the accuracy of the model and confirm the reasonability of included assumption and simplification.

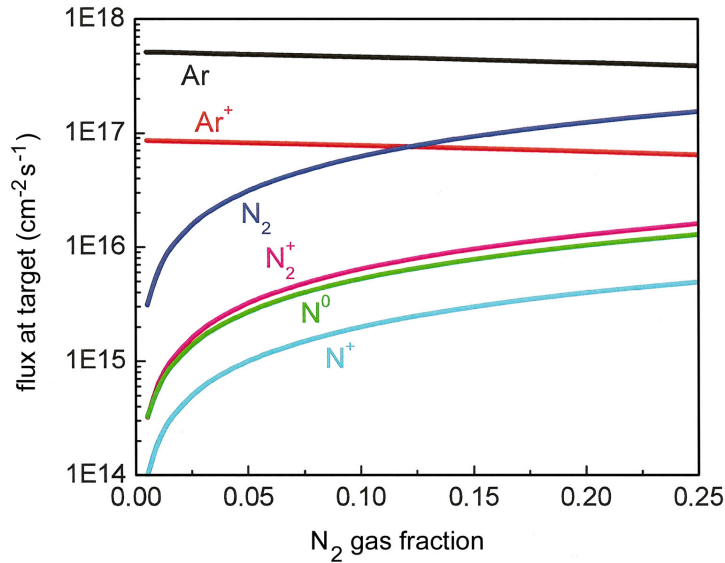


Figure 3.2: Gas kinetic fluxes (Ar and N₂) of plasma produced species arriving at the target surface versus nitrogen addition to the process gas, as obtained from plasma modeling.

Figure 3.2 shows the results of the plasma modeling for an Ar/N₂ discharge. For completeness the gas kinetic fluxes of inert gas atoms and N₂ molecules are also included in graph 3.2. The latter fluxes can be derived from equation (2.69), which is introduced in section 2.5.2. For the present modeling again the masses and partial pressures of the respective gases are inserted in accordance with the experiments. Further a gas temperature T of 50 meV is assumed during magnetron operation. [46] From figure 3.2 it is apparent, that at low nitrogen addition (<10%) the Ar ion flux is higher than the gas-kinetic flux of nitrogen molecules. The ion bombardment is dominated by the argon ions. The ratio of the nitrogen and argon ion fluxes is in reasonable agreement with the partial pressure ratio of the respective gases. The ratio of N₂⁺ to N⁺ ions is about 3, which is in reasonable agreement with experimental data. [47,48] The flux of N⁰ radicals is roughly half of the N₂⁺ flux and is smaller than the flux of N₂ molecules by little more than one order of magnitude ($j_N/j_{N_2} \approx 0.08$). It is noted that the contribution of reactive gas radicals and molecules fluxes are further influenced by the target sticking coefficient of these species, which will be discussed further in section 3.3.5.

3.2 Surface modeling

3.2.1 Fluxes towards the target

For modeling the incident particle fluxes can be taken from the global plasma model introduced in section 3.1. As the quantities of impinging fluxes were calculated there, the lateral

distribution across the target diameter will be discussed in this section.

Figure 3.3 shows schematically the plasma species, which are involved in the reactive deposition process. Due to the inhomogeneous plasma above the target the ion fluxes have their maxima in the race track region, whereas there is an uniform distribution of impinging neutrals across the target diameter.

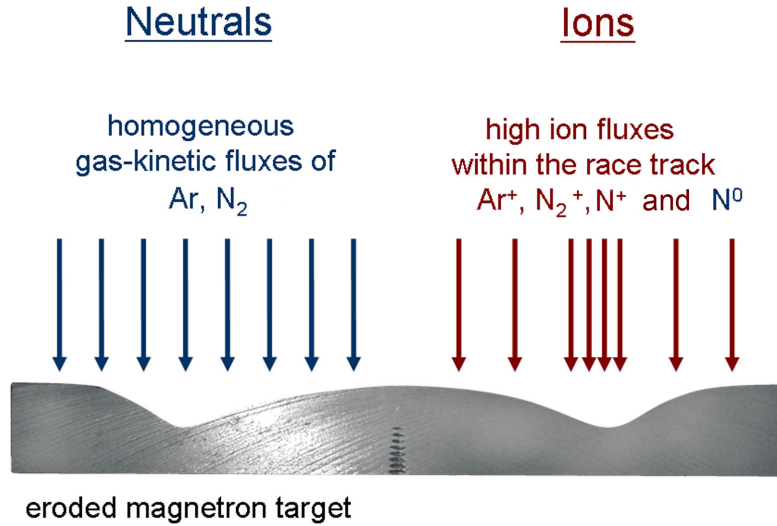


Figure 3.3: Schematic of lateral variation of plasma species fluxes towards the target surface

In figure 3.3 the cross sectional view of an eroded sputter target is imaged. The radial distribution of ion current density, which is shown in figure 3.4, has been derived from such surface erosion profile. The Ti target was sputtered for this purpose approximately 17h in pure Ar atmosphere. The measured erosion depth $e(r)$ along the target radius R was converted directly into a current density distribution $j(r)$. The distribution $j(r)$ was normalized to the measured target current during magnetron sputtering.

$$I_t = \int_0^R j(r) 2\pi r dr \quad (3.8)$$

A magnetron operation in constant current mode at 300 mA target current leads to the current density, which is shown in figure 3.4.

It is noted here, that the measured target current I_t was corrected by the amount of emitted secondary electrons. With an emission coefficient of $\gamma = 0.1$ [20, 44], the ion current at the target $I_t = 300$ mA reduces to an effective current

$$I_{eff} = I_t(1 - \gamma) \quad (3.9)$$

of ≈ 270 mA, which is considered for the modeling of reactive sputtering described below.

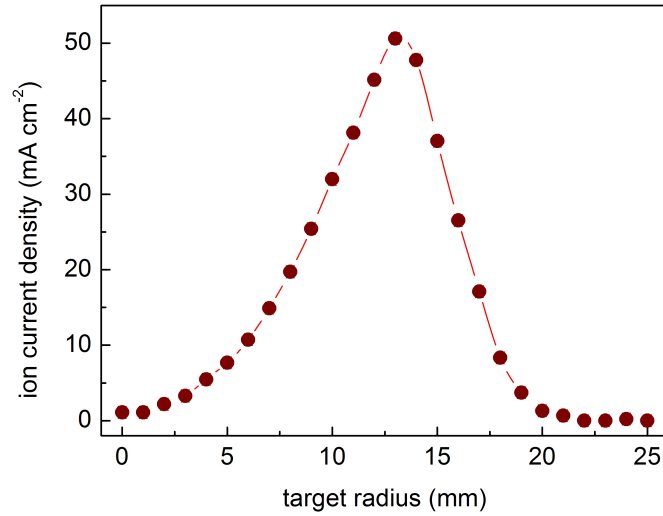


Figure 3.4: Ion current density as derived from the erosion profile of a Ti sputter target after long time magnetron operation for 17 h with Ar inert gas only.

3.2.2 Mechanisms of plasma particles - surface interaction

The above denoted plasma species strike the target surface through different processes, which are listed qualitatively for Ar/N_2 and Xe/N_2 discharges in Table 3.2 together with the kinetic energies of each species. The energy of the neutral molecular and atomic nitrogen does not allow any surface penetration. For these species only adsorption at the target surface is considered. Inert gas neutrals are assumed to be reflected from the target surface.

In spite of the neutral atoms and molecules, ions created in the plasma can gain in energy by the target potential. These particles affect the target surface with their high kinetic energy by direct ion implantation, furthermore they cause surface sputtering and recoil implantation. The latter acts not only on adsorbed species, but may also transport implanted

Table 3.2: Atomic and molecular species taking part in plasma surface interaction at the target, with their approximate incident energies and the corresponding interaction process.

Plasma Species	Approx. energy	Processes
N_2	50 meV	adsorption
N^0	eV	adsorption
N_2^+	$eV_t/2$ (2 atoms)	implantation, recoil implantation, sputtering
N^+	eV_t	implantation, recoil implantation, sputtering
Ar^+, Xe^+	eV_t	sputtering, recoil implantation

nitrogen into larger depths of the bulk. It is assumed for the modeling that reactive gas ions remain implanted in the subsurface up to the stoichiometric limit, whereas any incorporation of inert gas ions is neglected. Further it should be noted that molecular reactive gas ions split into two atoms with half of the initial energy when impinging the target surface. The depth on which the ion bombardment phenomena influences the target surface can be estimated by the range distributions of the involved ions, which are shown in figure 3.5. The data were obtained from static binary collision simulation using standard TRIM computer simulation [49] for ion energies of 350 eV in fig.3.5(a) and 500 eV in fig.3.5(b). The mean projected ranges are between 1 nm and 1.5 nm depth, with slightly higher ion ranges during magnetron operation in Xe/N_2 gas mixture, due to the higher target voltage.

From the obtained range distributions a thickness of the nitrated target surface layer of only a few nm can be expected. Atomic nitrogen ions penetrate most deeply, however the resulting depth profile of implanted nitrogen will be influenced only to a minor extent by this species, since it exhibit the lowest fluxes as described above (see fig.3.2).

3.2.3 Nitrogen incorporation at the target surface

Due to the above atomic processes, an initially purely metallic target surface becomes nitrated ("poisoned") at increasing time or fluence of the bombarding particles. At sufficiently large fluence, a dynamic stationary state evolves with a constant subsurface nitrogen profile, which is given by the balance of nitrogen injection by ion implantation and combined adsorption and recoil implantation, and nitrogen removal by surface sputtering.

Figure 3.6 shows the development of implantation depth profile of nitrogen ions. The data were calculated with dynamic binary collision computer simulation program TRIDYN [50, 51]. Different depth profiles at increasing ion fluences are shown for medium reactive gas addition and unity sticking coefficient of N_2 . At low ion fluence, the profile is dominated by a surface peak due to adsorption and recoil implantation. At higher ion fluences, a contribution of ion implantation becomes visible at a depth of around 1.5 nm, which reflects mainly the range profile of N_2^+ . At high ion fluence of N_2^+ the depth profile saturates towards a rectangular shape. The saturated depth profile shows a tail which may be attributed to multiple recoil implantation and some contributions of N^+ ions.

The almost rectangular, stationary implantation depth profile results from the equilibrium of ion implantation under simultaneous surface erosion. The maximum depth of 2.5 nm is larger than indicated in figure 3.5. This deviation is primarily caused by the dynamic simulation of surface composition which is only partially nitrated in contrast of stoichiometric TiN for which the data of figure 3.5 have been calculated. From the depth profile, which is shown in figure 3.6 a maximum depth of nitrogen of 2.5 nm can be derived, which will be used in the analytical model of reactive sputtering, described below.

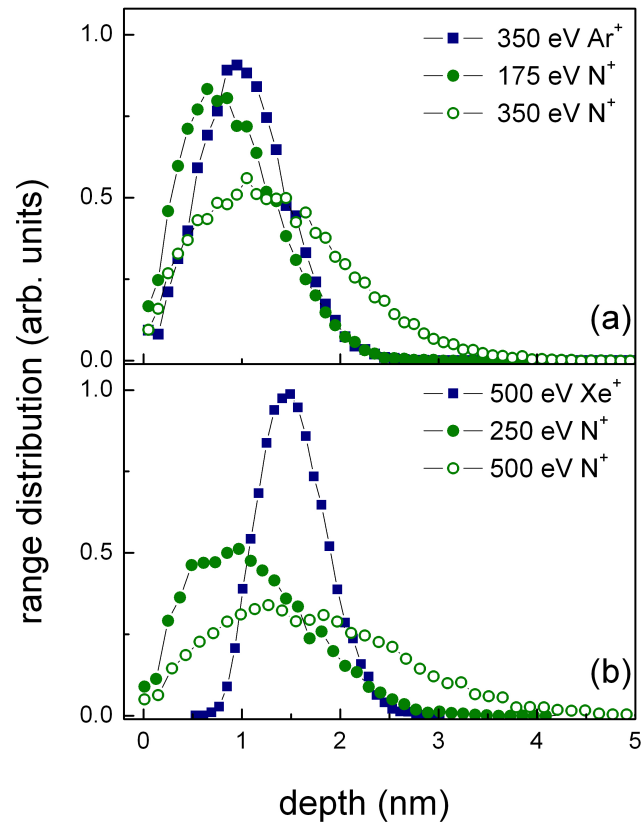


Figure 3.5: Static ion range distribution of plasma species incident on TiN for magnetron operation in Ar/N_2 gas mixture at ≈ 350 V target voltage (a) and Xe/N_2 gas mixture at ≈ 500 V target voltage (b), respectively. (N_2^+ ions split into two atoms of 175 eV and 250 eV, respectively) The data have been obtained from TRIM binary collision computer simulation

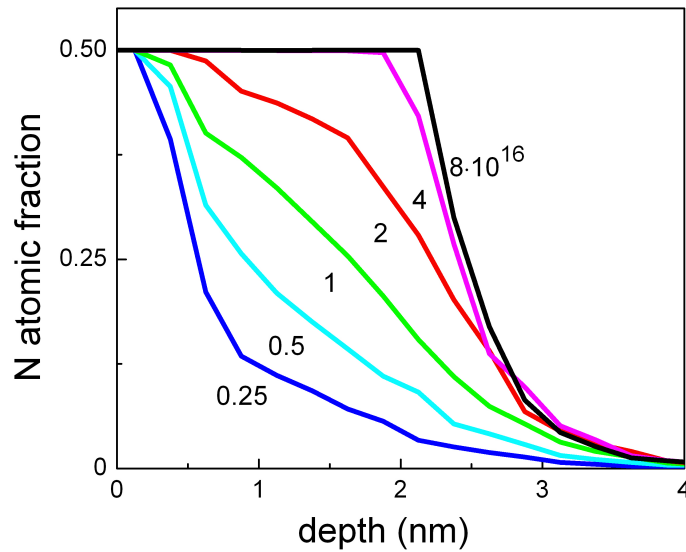


Figure 3.6: Nitrogen depth profiles at increasing total ion fluence for a reactive gas addition of 15 mol% and a sticking coefficient = 1 of molecular nitrogen

3.3 Modeling of reactive sputtering

An early theoretical description of the reactive sputtering process has been formulated by Berg et al. [16, 19, 52]. The model includes the reactive gas balance during thin film growth and target poisoning to predict the optimum operating parameters as well as instabilities of the process. The reactive gas balance is determined by the inlet and outlet flows and by the consumption due to layer deposition at the chamber walls, the substrate and the sputtering target. The consumption at these surfaces was treated within an adsorbed-layer model. Recently, it turned out both from experiment [53–56] and computer simulation [57, 58], that up to ten monolayer of reactive gas are incorporated into the target surface, which was ascribed to direct implantation of reactive gas and recoil implantation of adsorbed reactive gas atoms mainly by inert gas ion bombardment.

The model introduced here is based upon the principles formulated by Berg and Larson [16, 52]. Correlated with experimental findings [53–56] of several groups and further theoretical considerations (e.g. [57]) this model was extended and improved. Whereas the early formulation by Berg treated only an adsorbed layer model at the target surface, recently Kubart et al. [58] published a description, which includes plasma-target interactions like

- adsorption of reactive gas molecules at target surface
- direct implantation of reactive gas ions

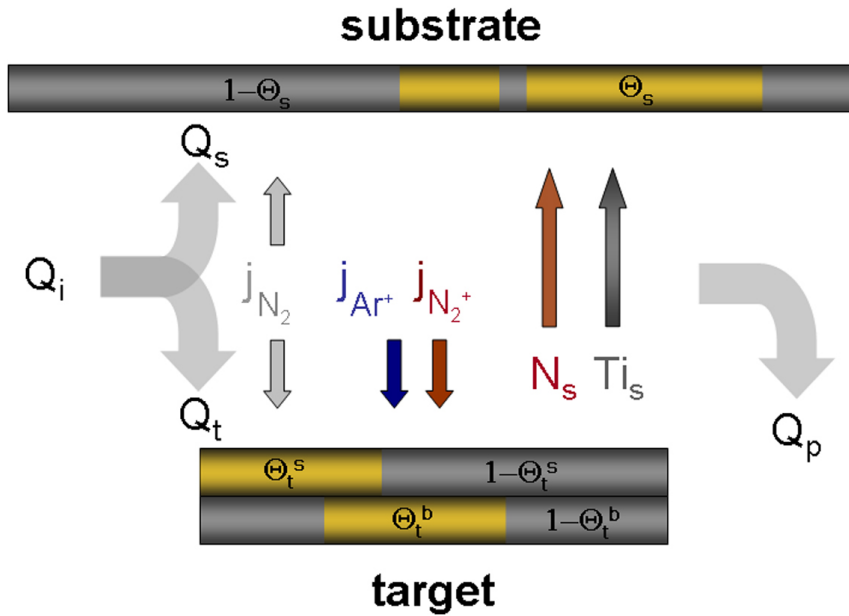


Figure 3.7: Schematic of particle fluxes during reactive sputtering. Shown are the target and substrate area, both with nitrated regions $\theta_{t,s}$ and metallic regions $(1 - \theta_{t,s})$, respectively. The target is divided into a surface and bulk layer, denoted by $\theta^{s,b}$. The total reactive gas consumption Q_i at steady state is equal to the consumptions caused by gettering at the target area Q_t and surface area Q_s and the flow that passes out the pump.

- recoil implantation of adsorbed reactive gas atoms mainly due to inert gas bombardment

This model involves a system of up to 10 layers to describe the temporal evolution of reactive gas depth profiles in the target subsurface region during magnetron sputtering. Applying this formalism only to the stationary state, it reduces to a two-layer system with a surface layer and only one underlying bulk layer. Furthermore the substrate area including all the walls of the deposition system contribute to the particle balance as well by consuming sputtered material and reactive gas. Considering target and substrate balance situations allows self-consistent modeling of reactive magnetron sputtering. The following sections will introduce the model.

3.3.1 Gas balance

The reactive gas partial pressure p_{N_2} within the deposition system is a crucial parameter in reactive sputtering. As mentioned above, there exists a complex non-linear dependence

between this parameter and the introduced reactive gas flow.

Figure 3.7 shows how the incoming gas flow Q_i , can be divided primarily into three flows. The balance between these flows determine the complex relation between p_{N_2} and Q_i . For steady state condition

$$Q_i = Q_t + Q_s + Q_p \quad (3.10)$$

where Q_t denotes the flow of reactive molecules towards the target surface, Q_s is the flow to substrate and chamber walls and Q_p is the reactive gas flow, which is not gettered at any surface and passes out through the vacuum pump. It is the task of the modelling to calculate the particle fluxes at the target and substrate areas, in order to determine the reactive gas flows $Q_t(p_{N_2})$ and $Q_s(p_{N_2})$.

As described in section 2.5.2 a probability for the adsorption of reactive gas molecules has to be introduced since not all nitrogen molecules resulting from equation (2.69) are consumed by the surfaces of the system. This is considered by the introduction of sticking coefficients S_t and S_s for the target and substrate area, respectively, into the model equations. A more detailed discussion follows in section 3.3.5.

3.3.2 Target balance

For the calculation of the particle balance at stationary state a two layer system is introduced, consisting of a surface monolayer and one underlying bulk layer. Both layers are composed from a compound fraction denoted with θ^s and θ^b , respectively, and a metallic fraction. The balance situation of the reactive gas incorporation is determined by various mechanisms. the stationary balance equation of the topmost target layer is

$$2j_{N_2}S_t(1 - \theta_t^s) + j_i x \theta_t^b (Y_{mc}\theta_t^s + Y_{mm}(1 - \theta_t^s)) - j_i Y_{gc}\theta_t^s - j_i Y_r \theta_t^s (1 - \theta_t^b) = 0 \quad (3.11)$$

where x denotes the stoichiometry of the compound MeN_x , with Me standing for the metal component.

The surface layer gains reactive gas atoms by adsorption of the molecular gas on the metallic fraction $(1 - \theta_t^s)$ with the zero-coverage sticking S_t (term I in equation (3.11)). Each molecule delivers 2 atoms to the surface, thus the factor of two is inserted. By sputtering metal atoms from both, metallic fraction (yield Y_{mm}) and compound fraction (yield Y_{mc}) the bulk material is exposed to the surface (term II). Depending on the previous bulk composition this process is an additional source of reactive gas, which may increase the compound fraction at the surface layer. The removal of reactive gas atoms occurs through sputtering from the compound fraction (with a sputtering yield Y_{gc}) and due to recoil implantation into the bulk material (with a yield Y_r), as long as the bulk is still partly metallic. These mechanisms are represented by term III and IV, respectively. The ion current density displayed in figure 3.4 contains primarily contributions from Ar^+ and N_2^+ ions, however any distinction in terms of sputtering and recoil implantation is neglected in the model. This simplification is less severe as the N_2^+ flux is significantly smaller than the Ar^+ flux. Thus, $j_i = j_{Ar^+} + j_{N_2^+}$

denoting the ion current density. Furthermore any multiple recoil implantation and the recoil implantation of metal atoms are discarded.

The equation for the balance situation of the underlying bulk is given by

$$2j_{N_2^+}(1 - \theta_t^b) + j_i Y_r \theta_t^s (1 - \theta_t^b) - j_i x \theta_t^b (Y_{mc} \theta_t^s + Y_{mm} (1 - \theta_t^s)) = 0 \quad (3.12)$$

It includes the implantation of reactive gas ions, which is represented by term one. Since the amount of reactive gas being implanted into the surface layer is very small (see figure 3.5) this contribution is neglected in equation (3.11). Term two stands for the increase of reactive gas due to recoil implantation from the surface into the bulk. Equation (3.12) contains also a transfer term (term III). This time sputtering at the surface replaces compound material in the bulk layer with pure metal from the target bulk (see eq. (3.11)).

It is assumed that adsorption, direct ion implantation and recoil implantation of reactive gas atoms only occur at the metallic target fraction. Therefore both equations contain saturation terms $(1 - \theta_t^{s,b})$. With increasing concentration of reactive gas, adsorption, recoil implantation and ion implantation are increasingly suppressed. As the energetic events will take place independent of the bulk concentration, this corresponds physically to a back-reflection of recoil atoms into the surface layer and to the reemission of implanted atoms into the vacuum. The transport is increasingly limited at increasing compound fraction, which physically corresponds to a suppression of short-range diffusion.

To calculate the compound fractions θ_t^s and θ_t^b for the surface and bulk layer, respectively, equation (3.12) can be inserted into equation (3.11) what results in a quadratic equation for the surface composition.

$$\alpha \beta \theta_t^{s2} - (\epsilon + \alpha \delta + \beta \gamma) \theta_t^s - \left(\frac{4j_{N_2^+}^2}{j_i^2} - \gamma \delta \right) = 0 \quad (3.13)$$

with the abbreviations

$$\begin{aligned} \alpha &= 2S_t \frac{j_{N_2}}{j_i} + Y_{gc}, & \beta &= x(Y_{mm} - Y_{mc}) - Y_r, \\ \gamma &= 2S_t \frac{j_{N_2}}{j_i} + \frac{j_{N_2^+}}{j_i}, & \delta &= 2 \frac{j_{N_2^+}}{j_i} + x Y_{mm} \\ \text{and} & & \epsilon &= 2 \frac{j_{N_2^+}}{j_i} Y_r \end{aligned} \quad (3.14)$$

For the solution of equations (3.13) - (3.14) the particle fluxes j_i , $j_{N_2^+}$ and j_{N_2} have to be entered. The gas kinetic flux j_{N_2} was calculated using equation (2.69). The total ion flux j_i can be derived from the effective target current as described in section 3.2.1 on page 42. The flux of reactive gas ions was assumed to be directly proportional to the ratio of partial pressures of reactive gas p_{N_2} to inert gas p_{Ar} and their ionization cross sections σ_{Ar} and σ_{rg} .

$$j_{N_2^+} = \frac{\sigma_{N_2} p_{N_2}}{\sigma_{N_2} p_{N_2} + \sigma_{Ar} p_{Ar}} j_i \quad (3.15)$$

The ratio of ionization cross sections is obtained by averaging the cross sections given in figure 2.3 over an energy range extending from the ionization threshold to the target voltage.

$$\frac{\sigma_{Ar}}{\sigma_{N_2}} = 1.35. \quad (3.16)$$

The yields for sputtering and recoil implantation were taken from specific TRIDYN simulation runs. The sputtering yield from the compound, $Y_{gc}=0.275$ and $Y_{mc}=0.07$ are the results from simulations at high nitrogen addition, where a stoichiometric TiN profile has been formed. The pure metal sputtering yield $Y_{mm}=0.45$ has been obtained from simulation at low nitrogen flow, where the yield was extrapolated towards zero reactive gas fluence. Ti sputtering yields sputtered from both, Ti and TiN under Ar^+ bombardment at energies between 400 eV and 700 eV have been published by Ranjan et al [59]. These data were obtained both from experiments and TRIM.SP [49, 60] computer simulation. The present value for Y_{mm} at an energy of 350 eV is in good agreement with the data in [59], whereas the present yield for Ti sputtered from compound Y_{mc} seems to be significantly lower. However this is attributed to a different experimental situation, in which the yield is measured at stationary sputtering of TiN in a pure Ar^+ beam. Under this conditions the nitrogen concentration at the surface decreases due to preferential sputtering. TRIDYN calculations were performed with adapted parameters [43], resulting in a calculated yield with a 30 % deviation from the value in [59]. The simulations show that the sputtering of stoichiometric TiN, which is relevant for the present modeling, reduces the Ti yield by a factor of around 3 with respect to $Ti_{0.75}N_{0.25}$, thus the present yields are reasonably consistent with those published in reference [59].

The recoil implantation yield again was obtained from TRIDYN simulation. A monolayer of TiN was bombarded with a low fluence of pure Ar^+ ions, which results in $Y_r=0.53$. Figure 3.8 displays the nitrogen depth profile from which the yield was calculated as the difference of the integrated nitrogen areal density and the nitrogen areal density in the surface monolayer, normalized to the Ar^+ fluence.

As it is shown in section 3.2.1, the ion flux towards the target is not homogeneously distributed. However, the balance situation at the target surface is strongly influenced by the ratio between bombarding ions and the molecular flux of neutrals. A more detailed description including the radial dependence of the target composition, the sputter yield and the reactive gas consumption can be achieved by inserting the measured ion current density distribution, as shown in figure 3.4, into the theoretical model.

For this purpose, the target area A_t is decomposed into 25 concentric rings with outer and inner radii r_i and r_{i-1} , which are influenced by the different particle fluxes.

$$A_t = \sum_{i=1}^{25} (\pi r_i^2 - \pi r_{i-1}^2) \quad (3.17)$$

The target compound fractions θ_t^s and θ_t^b , can be calculated as function of the radial position by solving equations (3.11) and (3.12) for each of these rings. This was realized with a loop algorithm in the simulation program.

The total nitrogen incorporation (in terms of an areal density) was derived by multiplying

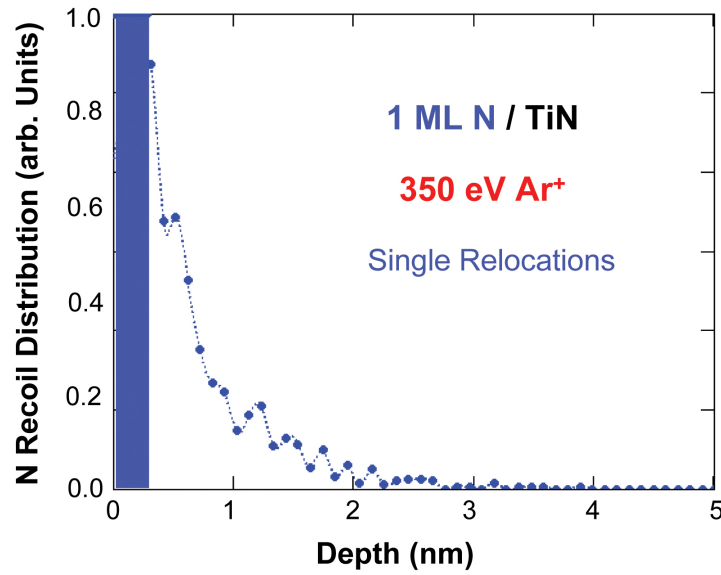


Figure 3.8: Nitrogen recoil distribution

θ_t^s and θ_t^b with the particle density within the compound. By definition, the surface layer corresponds to one atomic monolayer. Further, the atomic density n_N of nitrogen in the stoichiometric compound is equal to the molecular density $n_{TiN} = 5.07 \cdot 10^{22} \text{ cm}^{-3}$ of TiN. The reactive atom areal density of nitrogen is then in a reasonable approximation $n_{TiN}^{2/3}$ and the nitrogen areal density in the surface monolayer is

$$\nu_N^s = n_{TiN}^{2/3} \theta_t^s \quad (3.18)$$

A larger uncertainty arises from the thickness of the bulk layer, which can be estimated from the penetration depth of the ions. From the stationary nitrogen profile shown in figure 2.8, which was calculated with TRIDYN, a depth of $d \approx 2.5 \text{ nm}$ can be derived. Subtracting from this the thickness $n_{TiN}^{-1/3}$ of the stoichiometric surface monolayer, results in a bulk layer thickness of $d \approx 2.23 \text{ nm}$. The nitrogen areal density within this bulk region is then

$$\nu_N^b = d n_{TiN} \theta_t^b. \quad (3.19)$$

3.3.3 Substrate balance

The substrate area, which also includes the walls of the vacuum chamber is influenced by different particle fluxes. The balance situation of these fluxes is described in equation 3.20, where it is assumed that all the material is deposited homogeneously at the substrate area. The reactive gas supply to the substrate occurs mainly through chemisorption of nitrogen molecules from the background reactive gas partial pressure (term I). Furthermore there is a flux of sputtered reactive gas atoms contributing to the reactive gas supply (term II). Since

the energy of the sputtered atomic nitrogen is higher, different sticking coefficients S_{s_m} and S_{s_a} are introduced in equation (3.20) for the molecules and sputtered atoms, respectively. The compound fraction θ_s formed at the substrate is reduced by the deposition of sputtered metal onto the compound (term III). The balance equation for the substrate area finally reads

$$2j_{N_2}S_{s_m}(1 - \theta_s)A_s + S_{s_a}\Gamma_N(1 - \theta_s) - \Gamma_{Ti}\theta_s = 0 \quad (3.20)$$

with the amount of sputtered nitrogen atoms Γ_N per unit of time

$$\Gamma_N = \sum_{i=0}^{25} jY_{gc}\theta_{t_i}^s A_{t_i} \quad (3.21)$$

and the amount of sputtered titanium atoms Γ_{Ti} per unit of time

$$\Gamma_{Ti} = \sum_{i=0}^{25} jx(Y_{mc}\theta_{t_i}^s + Y_{mm}(1 - \theta_{t_i}^s))A_{t_i} \quad (3.22)$$

The fraction $\Gamma_N(1 - \theta_s)$ of sputtered nitrogen is deposited onto the metallic part of the substrate and converts it into the compound fraction θ_s . Sputtered nitrogen which reaches the fraction θ_s of reacted material, does not change the situation at the substrate and is neglected in the balance equation (3.20). The fraction $\Gamma_{Ti}\theta_s$ increases the amount of non-reacted target material at the substrate.

The different target regions (rings) with the area A_{t_i} contribute with a certain amount of sputtered material accordingly to the ion current density distribution shown in figure 3.4. The total yield of incoming fluxes at the substrate is the sum of all these contributions which are represented in equation (3.21) and (3.22), respectively.

3.3.4 Reactive gas consumption

From equations (3.13) and (3.20) finally it is possible to calculate the reactive gas consumption of the sputter system. Quantities of the process as the behavior of reactive gas partial pressure, the deposition rate and the target composition are predictable as function of the reactive gas flow into the vacuum chamber.

For the sputter target the consumption Q_t is given again as the sum of contributions of each target area A_{t_i} .

$$Q_t = \sum_{i=1}^{25} (2j_{N_2}S_t(1 - \theta_{t_i}^s) + 2j_{N_2^+}(1 - \theta_{t_i}^b) - j_iY_{gc}\theta_{t_i}^s)A_{t_i} \quad (3.23)$$

Term (I) in (3.23) describes the sticking of nitrogen molecules at the metallic target surface. The implantation of N into the target bulk is included in term (II) and term (III) considers the removal of reactive gas from the target area.

The reactive gas consumption of the substrate area Q_s is given as

$$Q_s = (2j_{N_2}S_{s_m}(1 - \theta_s)A_s + S_{s_a}\Gamma_N(1 - \theta_s)) \quad (3.24)$$

where term (I) in (3.24) denotes the gettering of nitrogen molecules at the metallic substrate area A_s and term (II) includes the total amount of sputtered atomic nitrogen Γ_N (see eq. (3.21)), which again is consumed by the metallic part of the substrate area.

Finally the throughput of the pump Q_p can be easily calculated. It is

$$Q_p = \frac{p_{N_2}}{k_b T} S \quad (3.25)$$

with p_{N_2} the reactive gas partial pressure and S the pumping speed of the vacuum pump. For the steady state the total gas consumption Q_{total} must be equal to the ingoing reactive gas flow as denoted in equation 3.10.

$$Q_i = Q_{total} = Q_t + Q_s + Q_p \quad (3.26)$$

3.3.5 Results of modeling

The established relation for $Q_i(p_{N_2})$ allows to model the behavior of nitrogen partial pressure p_{N_2} as a function of the applied nitrogen gas flow into the sputter chamber. One result of modeling is displayed in figure 3.9, where the nitrogen partial pressure (a) and the amount of sputtered titanium (b) are calculated for a homogeneous (constant) ion current distribution across the target (dashed-dotted line) and for the inhomogeneous ion current distribution $j(r)$ (solid line), which is shown in figure 3.4, respectively.

Figure 3.9 shows that, as the N_2 gas flow is increased from a low level, its partial pressure (b) remains almost constant at a low value of around 0.001 Pa. All of the reactive gas will be consumed in the reaction with the pure titanium being sputtered from the target. Under this condition the sputter target is metallic and the sputter yield (a) remains high at around $0.8 \cdot 10^{17}$ Ti s^{-1} . When the gas flow reaches the critical value of around 0.9 sccm the gas flow rate into the chamber becomes higher than the gettering rate of the pure metal, a TiN compound layer forms on the target surface. This reaction occurs very quickly and is connected with a significantly drop of the sputter rate. As it is shown in figure 3.9(a) the sputter yield for the TiN system reduces by a factor of around 4. In the consequence less reactive gas is consumed by the sputtered Ti and the reactive gas partial pressure increases rapidly up to 0.03 Pa. Both calculations in (a) and (b) show the typical, abrupt change in the sputter rate and in p_{N_2} as well as their hysteresis behavior, which is described in section 2.7.

The width of the hysteresis is a measure of the process stability. A smaller hysteresis corresponds to an improved process stability. The higher ion current density, which is confined on a small area, can be considered as a smaller effective target size. Referring to constant magnetron power the target remains still metallic even at higher reactive gas flows, due to enhanced sputtering within the region of higher current density. This leads to a higher sputter rate and higher reactive gas consumption. An improved operating stability

and limitation of the hysteresis effect due to the use of a smaller target have been introduced as a method for process stabilization in references [11, 17].

Influence of the pumping speed

Figure 3.10(a) shows another possibility to achieve stable operating conditions, which has been described by numerous authors in e.g. [38, 61–63]. Here the behavior of the reactive gas partial pressure p_{N_2} is plotted as function of the reactive gas flow, for different values of pumping speed of the system vacuum pump. It is shown, that with increasing pumping speed the width of hysteresis becomes smaller, whereas the critical value of reactive gas flow remains constant at around 0.55 sccm. In the compound mode, p_{N_2} is linearly connected with the applied reactive gas flow. The gradient of p_{N_2} in this mode, decreases for higher values of pumping speed and enables thereby a gradual transition from the metallic to the compound deposition mode. At high pumping speed the reactive gas consumption of the vacuum pump is high enough, that it dominates the consumption by the growing TiN layer at the substrate area and, thereby, the behavior of p_{N_2} .

Figure 3.10(b) shows a comparison between simulation and experimental data, which were recorded with the calibrated mass spectrometer during reactive sputtering. The model parameters include the experimentally determined pumping speed of 60 l/s, the ion current density $j(r)$ (see figure 3.4) and a substrate area of 0.15 m², which is reasonable since, the walls of the vacuum vessel are affected by sputtered material to a large extend, due to the absence of a properly substrate in front of the magnetron.

The result of modeling is in good agreement with the experimental data. In particular the critical reactive gas flow value for the transition from metallic to compound mode, but also the magnitude and gradient of partial pressure increase are very well described by the model. The simulated pressure values are slightly below the experimental points, which cannot only be ascribed to the deficiencies in the model, but also in a systematic error during the calibration of the mass spectrometer and during the measurement of the partial pressure. One uncertainty for instance arises since the spectrometer had to be calibrated with the magnetron and, thereby, the plasma switched off, whereas it was exposed to the nitrogen ions created in the plasma during sputtering.

Effect of variable sticking coefficient of N_2 molecules

The nitrogen incorporation at the target is strongly influenced by the sticking of nitrogen ions, molecules, and radicals. In general, the sticking coefficient, which denotes the retained fraction of the incoming flux, decreases with the incorporation or coverage of the implanted and adsorbed species, respectively. A definition of the sticking coefficient, which is required in any surface models, can be described as introduced in section 2.5.2.

As it is shown in figure 3.6, nitrogen ions penetrate into the surface up to around 2.5 nm. The sticking coefficient of incoming ion flux, is given by the fraction, which is not collisionally reflected from the surface. According to TRIM computer simulation [49] the reflected fraction of nitrogen ions in the present range of ion energies is around 15%, so that the

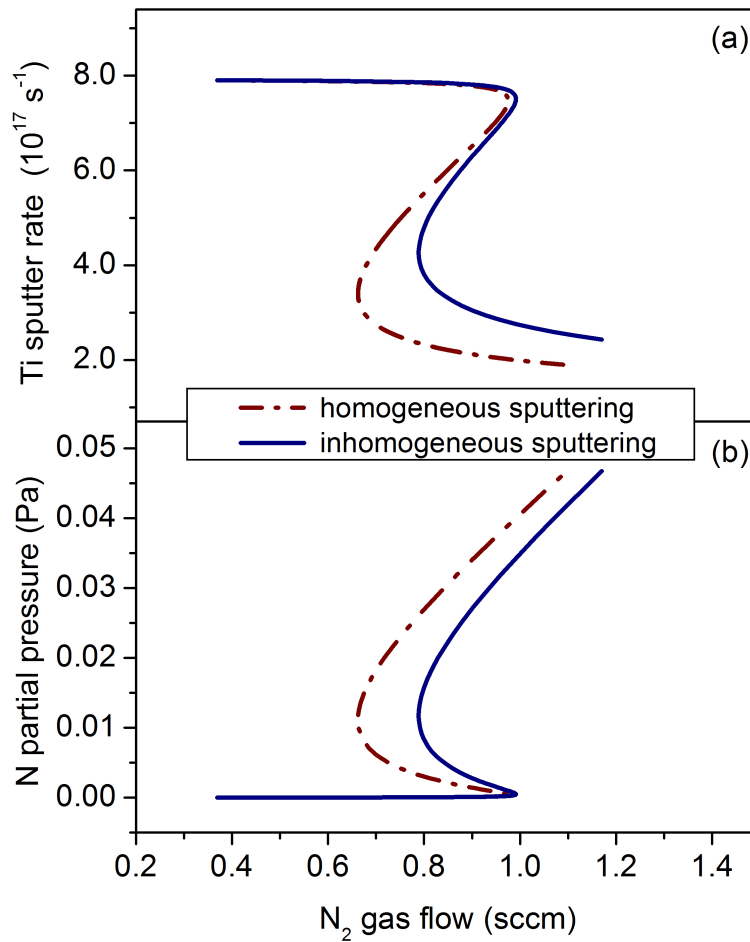


Figure 3.9: Modeling of Ti sputter rate (a) and reactive gas partial pressure (b) during reactive sputtering for a homogeneous (red, dashed-dotted line) and inhomogeneous (blue, solid line) ion current distribution across the target. The parameters used in the simulation can be found in table 9.2.

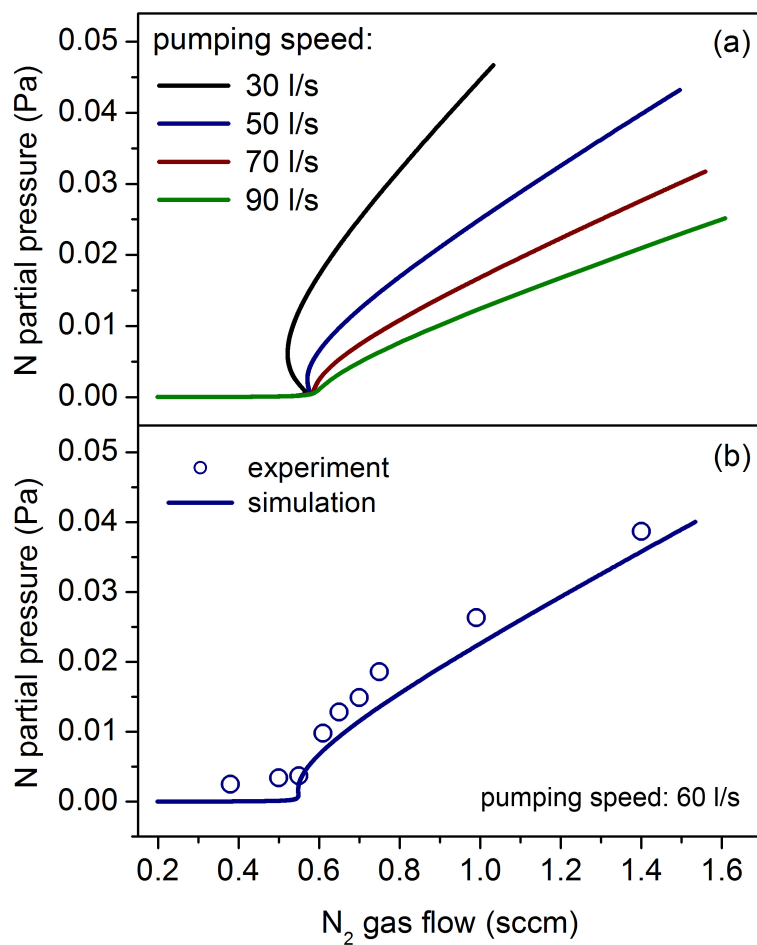


Figure 3.10: a) Modeling of partial pressure at different values of pumping speed of the vacuum pump. b) Comparison with experimental data as measured with the calibrated mass spectrometer. The parameters used in the simulation can be found in table 9.2.

sticking coefficient at the pure metallic surface is treated as unity here. Hence almost all of the impinging ions are implanted in the target material.

For the zero-coverage sticking coefficient of nitrogen molecules around room temperature, data from indirect experiments are given in literature [64,65], which scatter widely between ~ 0.1 and ~ 0.8 with a mean value of ~ 0.3 . The latter is also given in reference [64] as the zero-coverage limit of a dependence on the coverage. Thus, in view of this uncertainty, the model will be applied and discussed in this section for the limits of zero and unity sticking, and consider the intermediate value of 0.3 as probably most realistic one for comparison with experiment.

In figure 3.11 (a) the nitrogen areal density at race track position versus reactive gas addition is calculated for a unity sticking coefficient S_t . The nitrogen content decomposed into contributions of the topmost surface layer and the bulk layer. The stationary nitrogen profile in figure 3.6 exhibits a depth of ~ 2.5 nm, which corresponds to a bulk layer thickness of 2.23 nm, as shown above. As this is significantly larger than the monolayer thickness, the total nitrogen inventory is dominated by the bulk layer contribution at typical magnetron powers. In the saturated regime, where the stoichiometric limit is reached and TiN has formed at the target, the nitrogen areal density in the topmost surface layer is $\sim 1 \cdot 10^{15}$ cm $^{-2}$, whereas the areal density in the bulk is $\sim 8.5 \cdot 10^{15}$ cm $^{-2}$.

Figure 3.11(b) shows the compound (TiN) surface (θ_s) and volume (θ_b) fractions, with the options of zero and unity molecular sticking at the target surface. At unity sticking of nitrogen molecules, both the surface layer and the bulk layer converges towards saturation above a reactive gas flow of around 2.5 sccm. At zero sticking, the amount of formed compound is considerably lower and shows a weaker tendency of saturation within the present range of nitrogen addition. The lower amount of compound in the bulk layer demonstrates the important role of recoil implantation of adsorbed nitrogen into this region, since this is the only mechanism, which is suppressed at zero sticking of molecules. Furthermore in this case, the only addition of nitrogen at the surface takes place due to sputtering, which transfers the bulk layer into the surface layer and exposes thereby TiN compound from the bulk to the surface. The amount of compound material at the surface layer compared to that one in the bulk layer differ more for the case of zero sticking. In this case the surface is cleaned by sputtering and adsorption as important nitrogen source is missing.

As it was shown already in graph 3.10, the results of modeling are in good agreement with experimental findings. Reactive gas partial pressure and critical points of reactive gas flow as well as the hysteresis behavior are well described by the two layer model. In the chapters 6 and 7, the model is applied further to quantify the experimental results of ion beam analysis and mass spectrometry.

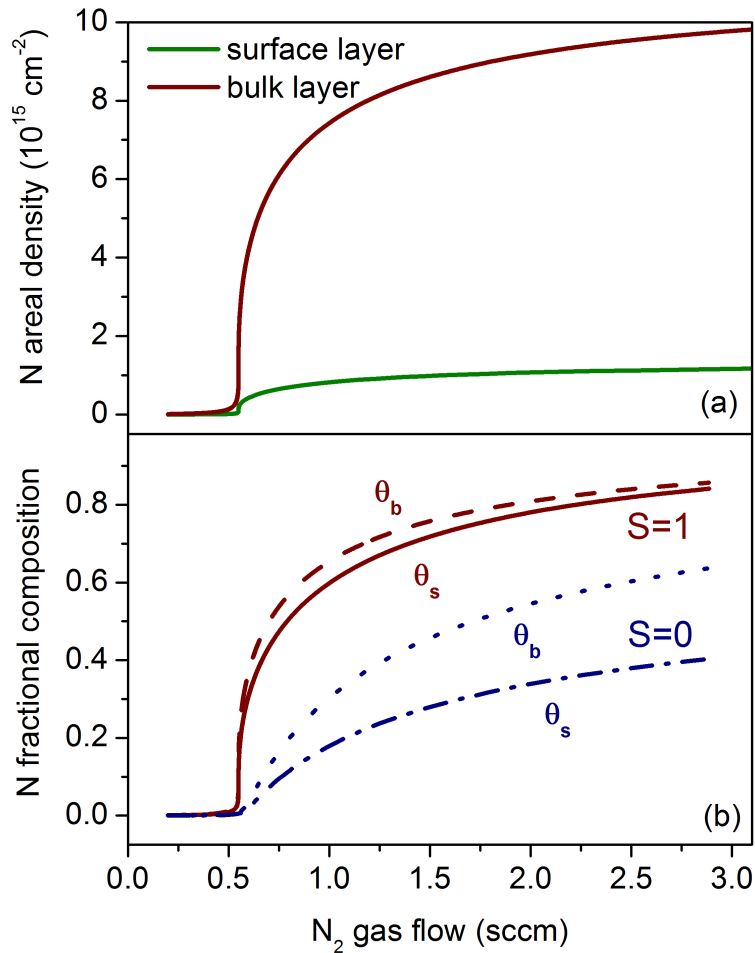


Figure 3.11: (a) Comparison of nitrogen areal densities for surface layer (green line) and bulk material (red line) of the Ti target exposed to an Ar/ N_2 plasma at increasing nitrogen addition. Both calculation are performed for unity sticking values $S_t = 1$ of N_2 molecules. (b) Compound (TiN) surface (θ_s) and volume (θ_b) fractions at the Ti target surface again at increasing reactive gas flow. Results are compared for unity (solid and dashed lines) and zero (dashed-dotted and dotted lines) sticking of N_2 molecules. All data are simulated for the erosion zone of the target. (parameters see table 9.2)

4 Experimental Setup

The investigation of target poisoning during reactive magnetron sputtering includes the analysis of reactive gas coverage of the magnetron target as well as a study of particle fluxes towards and from the target surface.

Figure 4.1 shows the setup that allows to combine ion beam analysis of the target surface and mass spectrometry in order to characterize the reactive sputter process. Since these particle fluxes resulting from the plasma-target interaction, the target surface composition as well as the plasma properties are of interest for the investigations.

For the experiments a standard sputter configuration was installed in an ultrahigh vacuum chamber which was attached to the beam line system of a 5 MV tandem accelerator. The planar circular dc magnetron of 5 cm diameter was equipped with a 99.995 % purity titanium target and positioned in the center of the vacuum chamber. An energy resolving mass spectrometer (HIDEN EQP 500) was placed in front of the magnetron at usual substrate position at a distance of 5 cm. A manipulator allows moving the magnetron vertically with respect to the axis of the mass spectrometer and the ion beam line what allows a laterally resolved investigation with both techniques.

During magnetron operation, a 10 sccm argon flow was maintained, whereas the nitrogen flow was varied between 0 and 3 sccm in order to realize different states of target poisoning. Both gas flows were adjusted using mass flow controllers resulting in an operating pressure between 0.3 Pa and 0.35 Pa. The base pressure in the 50 liters vacuum chamber of $\sim 1 \cdot 10^{-6}$ Pa was reached using a turbo pump with a maximum pumping speed of around 190 l/s. The throughput of the pump was controlled by a throttle valve to lower values as required for magnetron operation. Figure 4.2 displays the pumping speed of the system versus the aperture of the valve. A typical aperture of ~ 0.2 during magnetron operation at ~ 0.3 Pa, results in a pumping speed of around 60 l/s.

Due to differential pumping a beam line pressure of $< 10^{-4}$ Pa was realized during magnetron operation. For pressure control two vacuum gauges were installed. A pirany gauge covers the range between 0.1 to 10^{-7} Pa and a capacitance gauge provides values with a higher accuracy in the range from 1 Pa to 10^{-3} Pa which is relevant for the sputter deposition process.

Typical parameters applied during magnetron operation are summarized in table 9.1 in the appendix.

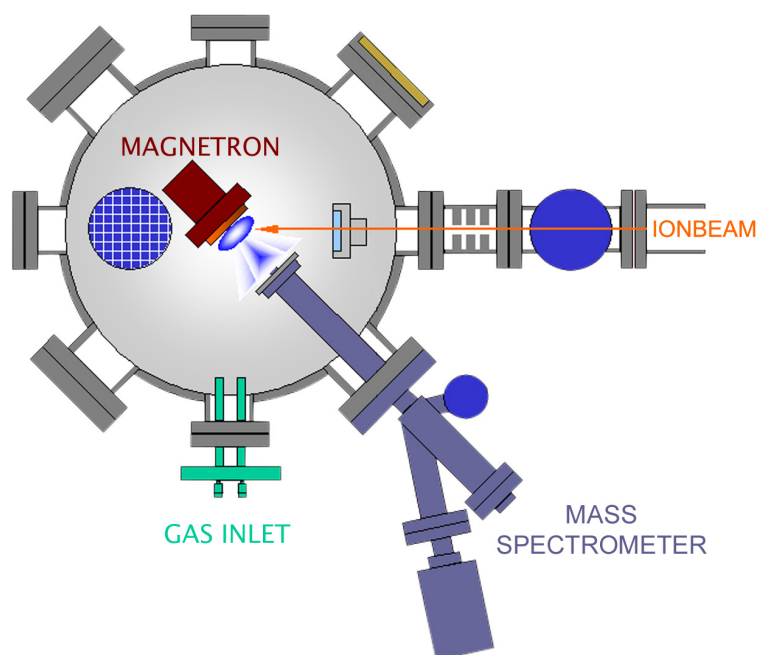


Figure 4.1: Experimental Setup with the 2 inch magnetron placed vertically moveable in the center of a high vacuum chamber. The energy resolved mass spectrometer is installed at usually substrate position at a distance of around 5 cm.

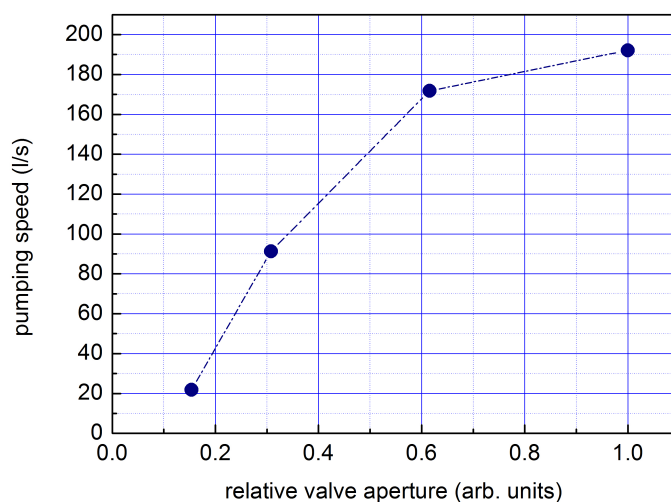


Figure 4.2: Pumping speed of the turpo pump versus valve aperture

5 Analysing methods

5.1 Ion beam analysis

Ion beam analysis enables the characterization of the target surface during magnetron operation. It is a well suited analyzing tool since ion beam itself as well as the detected α particles possess energies in the order of several MeV, so that any influence of the magnetron discharge and the involved electrical-magnetic fields can be neglected.

In Figure 5.1 a schematic view of the detector setup is shown. The analyzing beam of 1.8 MeV deuterium ions (D^+) with a typical current of 30 nA was directed onto the target surface. The ion beam is collimated to a spot of $1 \times 1 \text{ mm}^2$, which defines the lateral resolution of the analysis.

The nitrogen incorporation at the target surface was analyzed using the $^{14}\text{N}(\text{d},\alpha_0)^{12}\text{C}$ and $^{14}\text{N}(\text{d},\alpha_1)^{12}\text{C}^*$ nuclear reactions. The α particle yields from these reactions were measured by means of a surface barrier detector, which was placed at a distance of 82 mm from the target under a back scattering angle of $\theta = 150^\circ$. With an effective detector area of $A = 150 \text{ mm}^2$ a solid angle $\Omega = 0.016 \text{ sr}$ is covered. The detector was covered by a thin aluminum foil in order to prevent any contact with the plasma. The foil was replaced periodically since the film deposition on the foil would cause an excessive energy loss of the emitted α particles, which would smear out the peak areas of the spectra.

In general the cross section for an NRA experiment cannot be written down in an analytical way, since it varies strongly with the scattering geometry and the energy of projectiles. For common analysis reactions for several elements the cross sections are published in references [66–68], from which the experimental conditions can be chosen. By Pellegrino et al. [69] cross sections of $\sigma(E, \theta, \alpha_0) = 1.6 \text{ mbarn sr}^{-1}$ and $\sigma(E, \theta, \alpha_1) = 3.8 \text{ mbarn sr}^{-1}$ are denoted for the setup shown in figure 5.1 and a deuterium D^+ energy of 1.8 MeV.

Due to the low cross section of the nuclear reaction, the convenience of the present experiment is hampered by long analysis times of 20 min and more, which still yield no more than about 200 counts of the α spectra. This, however, does not deteriorate other than the statistical quality of the results as all measurements have been performed in stationary state.

Assuming only a thin nitrogen layer at the target surface, which is reasonable for compound formation under sputtering conditions, the yield Y of α particles can be derived from equation (5.1):

$$Y = \sigma(E, \theta) \cdot \Omega \cdot I \cdot n \cdot d \quad (5.1)$$

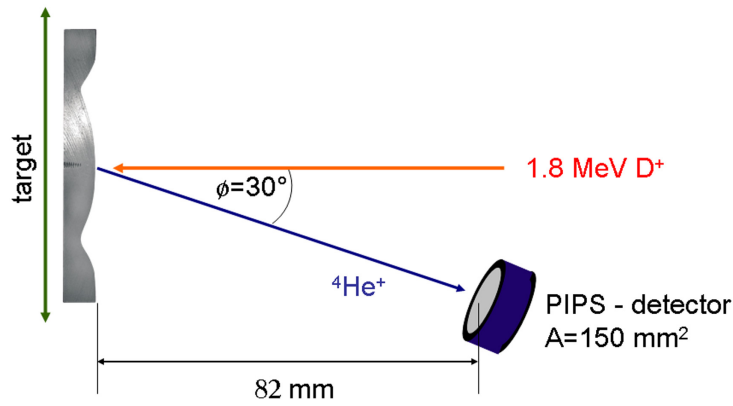


Figure 5.1: Schematic of the arrangement of magnetron target, detector and ion beam direction. The surface barrier detector with an effective area of $A=150 \text{ mm}^2$ was placed at a backscattering angle of $\Theta=150^\circ$ referring to the ion beam axis. The distance between target and detector was 82 mm, what results in a solid angle of $\Omega=0.016 \text{ sr}$.

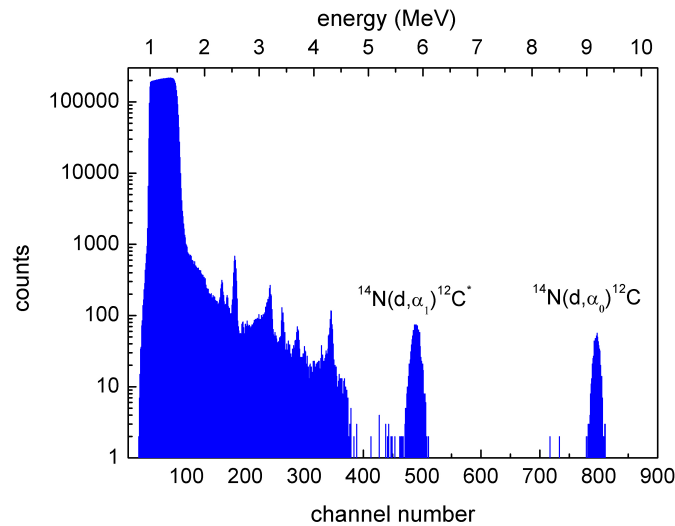


Figure 5.2: NRA spectrum as obtained during the analysis of target nitrogen incorporation. The analyzed $\alpha_{0,1}$ particles spectra are background free due to their high energies. At lower energies elastically reflected Deuterons and protons of various reaction channels can be observed.

The integral yield of the peaks is proportional to the areal density $n_A = n \cdot d$ of nitrogen in the target surface, where n denotes the atomic density and d is the layer thickness. With the differential cross sections $\sigma(\alpha_0)$ and $\sigma(\alpha_1)$, the solid angle covered by the detector $\Omega = 0.016 \text{ sr}$, the flux of impinging $\text{D}^+ \text{I} \approx 200 \cdot 10^9 \text{ s}^{-1}$ and an areal atomic density of $n_A = 1 \cdot 10^{16} \cdot \text{cm}^{-2}$ nitrogen atoms, a yield of $\approx 0.18 \text{ s}^{-1}$ can be expected as a sum from both $^{14}\text{N}(\text{d},\alpha_0,1)^{12}\text{C}$ reaction channels. Due to the high Q-value of the employed nuclear reaction, background free energy spectra are obtained at ≈ 9 and $\approx 6 \text{ MeV}$ for the α_0 and α_1 reaction channels (see fig. 5.2). The calibration of the areal density was performed by means of a Ti sample which has been implanted with a well-defined dose of $(1 \pm 0.02) \cdot 10^{17} \text{ N}^+ \text{ cm}^{-2}$ at 50 keV resulting in a mean depth of $\approx 60 \text{ nm}$. By time-dependent analysis of the nitrogen areal density of the calibration target and the magnetron target (with the magnetron switched off), it was assured that the ion beam does not induce any release of nitrogen retained in the targets.

Figure 5.2 shows a NRA spectrum obtained from the calibration target.

5.2 Mass spectrometry

The composition and properties of the magnetron plasma as well as yield and energy distribution function of sputtered particles were analyzed by means of the energy resolving mass spectrometer HIDDEN EQP 500.

It was placed in a distance of 5 cm from the magnetron at usual substrate position. In the pressure range of 0.3 Pa during magnetron deposition, the gas kinetic mean free path length is several cm and thereby close to the distance between the target and the mass spectrometer orifice, so that neutral-neutral or ion-neutral collisions affect the measurements only to a minor extent. Due to differential pumping, a base pressure of $\approx 1 \times 10^{-6} \text{ Pa}$ was maintained inside the spectrometer during the deposition process. This enlarges the mean free path of a particle inside the spectrometer up to several metres what is much larger than the dimensions of the device, so that gas phase collisions inside the spectrometer can be neglected again.

The mass spectrometer is made up of four distinct elements, which are introduced in the following section.

5.2.1 Details of the mass spectrometer

- Spectrometer orifice, electron source and ion optics

The first part consists of the sampling orifice (extractor) with an aperture of 100 μm in diameter. Extractor and first electrodes can be biased to a positive potential, which may be usually applied to prevent positive ions from entering the spectrometer. In the presented experiments this was found to be inappropriate, since in particular recorded energy distributions were affected by this parameter. An electron source for the electron impact ionization of neutral particles is placed behind the extractor tube. In residual gas analysis mode (RGA) neutral species with thermal energy of $\approx 50 \text{ meV}$ diffuse from the plasma into the spectrometer and get ionized by the electron source. Ions are formed at an additional potential of 3 V in order to transfer them into the

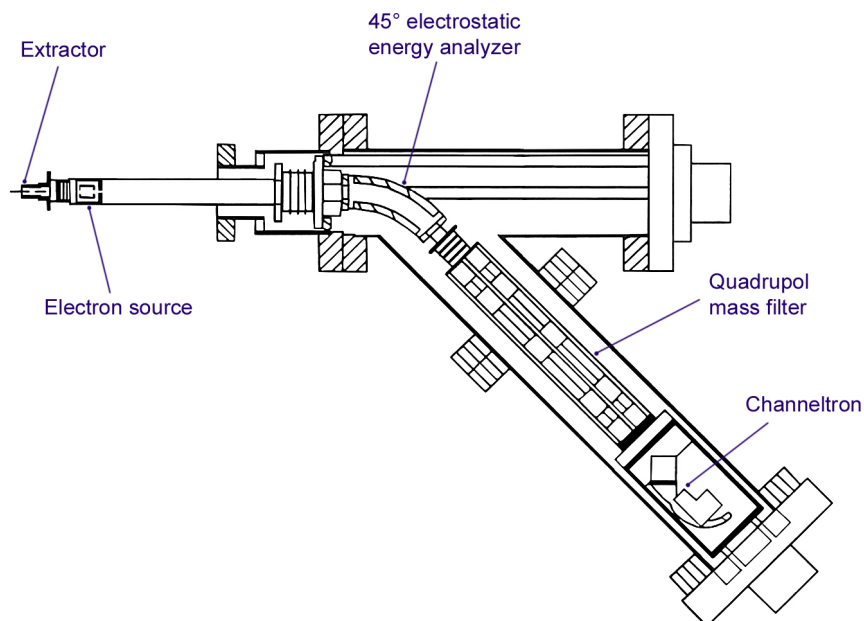


Figure 5.3: Schematic view of the HIDEN EQP 500 energy resolving mass spectrometer

drift space towards the energy filter.

The energy of electrons produced in the source can be adjusted between 10 eV and 120 eV. In general the electron energy is fixed at ~ 100 eV where the electron impact ionization cross section exhibits a maximum for numerous gases as it is shown in figure 2.3. A technique which allows to detect radicals in the plasma is the so called appearance potential method or threshold spectroscopy, where the electron energy across the ionization threshold is scanned [70].

The elements and parts mentioned above determine the acceptance angle, which can be defined as the maximum entrance with respect to the optical axis at which an ion can be accepted by the mass spectrometer. Low et. al [71] denote for a comparable plasma monitor a maximum acceptance angle of $\approx 1^\circ$ for ion energies around 4 eV. This value was calculated using the SIMION software [72]. Transferred to the current setup a lateral resolution of less than 1 mm^2 can be assumed, in order to investigate particles, sputtered from the target surface.

The ion optical units direct the ions into part two, the 45° electrostatic energy analyzer (ESA).

- Electrostatic analyzer (ESA)

The ESA transmits only ions with one specific energy to charge ratio (E/q). Since such a 45° sector field has a constant relative energy resolution $\Delta E/E$, the analyser is set to constant transmit energy in order to obtain a constant energy resolution for all the incoming ions. For this purpose, ions are accelerated or decelerated by the ion

optics before entering the ESA.

- RF quadrupole mass filter

The RF quadrupole mass filter selects ions of a specific mass to charge ratio (m/q), by passing them through superposed RF and DC fields applied to a system of four parallel rods. For ions with a certain m/q stable trajectories exist. To obtain good mass resolution each ion must experience a minimum number of RF cycles and has usually to be decelerated before entering the quadrupole. On the other hand many ions with the correct m/q ratio might get lost due to non-optimum conditions on the entry to the filter as the dwell time within the filter is too long. Therefore the adjusted transit energy through the filter is a compromise between mass resolution and sensitivity.

- SEM Detector (SEM = secondary electron multiplier) / Channeltron

The detection of ions, which have passed all filters, occurs via secondary electron production in the first dynode of the SEM detector. Applying a voltage of ≈ 2000 V to an arrangement of further channel plate these electrons can be multiplied, what amplifies the signal. Since the performance of the SEM depends strongly on the surface composition of the dynodes regular calibrations are crucial for interpreting absolute yields.

Combining the two systems ESA energy filter and RF quadrupole mass filter as it is realized in the HIDEN EQP 500 and scanning the mass at a fixed ion energy enables to detect various ionic species, whereas scanning of the ion energy at a selected mass enables measurements of ion energy distributions.

5.2.2 Sensitivity of the mass spectrometer

The ionization probability in the electron source and the ion trajectories of the system depend on the initial energy of particles entering the spectrometer. Therefore each energy distribution is convoluted with the instrument transmission function.

In particular decelerating ions in an electrostatic field broadens their angular distribution, what causes a drop in ion counting efficiency, because of the acceptance angle. Therefore the transmission for originally fast ions is small compared to that one of slow ions. Furthermore low energy ions are also deflected more easily towards the optical axis than high energy ions, resulting in an larger acceptance angle at lower energies.

Investigating the energy distribution of originally neutral particles (e.g. sputtered particles) one has to consider that the ionization probability scales with the time of flight through the ionization space, which can either be the plasma or the electron source of the spectrometer.

All these facts can be expressed as

$$N(E) = N^0(E) \cdot P_I(E) \cdot T(E) \quad (5.2)$$

where $N(E)$ denotes the recorded ion energy distribution, $N^0(E)$ the originally neutrals energy distribution, $P_I(E)$ the ionization probability and where $T(E)$ is the transmission function of the monitor.

$P_I(E)$ is proportional to the dwell time of the neutral atom within the ionization space and hence $\propto 1/\sqrt{E}$. For $T(E)$ Low et al. [71] published a power law dependence on the initial energy $T(E) \propto E^{-\beta}$ with $\beta \approx 1.5$.

These dependencies were also used in the present work to correct the measured energy distribution functions accordingly.

5.2.3 Details of operation

Two operating modes are available in the mass spectrometer. In residual gas analysis (RGA) mode originally neutral atoms and molecules are analyzed by means of the internal ionizing source which provides ions for mass and energy analysis. In secondary ion mass spectroscopy (SIMS) mode all optics of the spectrometer are optimized for the analysis of externally generated ions. The ionization source is switched off.

6 Results and discussion I (Ion beam analysis)

The following sections introduce ion beam investigations of the stationary nitrogen incorporation in the Ti target. During magnetron operation at constant conditions the analyzing beam of 1.8 MeV D^+ ions was directed onto various positions of the target surface in order to measure a lateral distribution. Further the nitrogen uptake of the target was analyzed at different values of nitrogen addition to the discharge and for magnetron operation using the inert gases argon and xenon, respectively.

6.1 Nitrogen incorporation at target race track

The stationary nitrogen incorporation in the target has been measured during reactive sputtering in Ar/N_2 and Xe/N_2 gas mixture using real-time ion beam analysis [56]. The magnetron was operated in constant current mode at $I = 300$ mA, which results in a target voltage of 350 ± 10 V for the Ar/N_2 gas mixture. The voltage increases slightly during target poisoning and towards higher nitrogen gas flows, respectively. For magnetron operation in a Xe/N_2 the target voltage is significantly higher at ~ 500 V with a more pronounced increase up to 570 V during the transition from metallic to poisoned target mode. As described above, this is attributed to an reduced SEEC due to the higher ion mass. For both discharges the pressure of 0.3 Pa was maintained, by applying a inert gas flow of 10 sccm. The added nitrogen gas flow was varied between 0.6 sccm and 3 sccm, which causes an increase of the total pressure of only up to ~ 0.35 Pa. The nitrogen partial pressures have been also recorded by means of the mass spectrometer.

The measured nitrogen areal densities versus the flow of reactive gas are displayed in figure 6.1 . In both cases, for sputtering in Ar/N_2 and in Xe/N_2 atmosphere the nitrogen incorporation in the target increases quickly even at low nitrogen addition. This is in accordance to the behavior of the nitrogen partial pressure versus nitrogen gas flow, which is shown in figure 3.10(b). At a critical flow value of around 0.55 sccm the nitrogen partial pressure increases abruptly and causes the higher nitrogen uptake of the target. At high reactive gas flow, the nitrogen areal density converges to the saturation value of $\sim 1 \cdot 10^{16} \text{ cm}^{-2}$ for sputtering with argon as inert gas. However, in the present range of nitrogen flow, the experimental data for Xe inert gas show a somewhat lower nitrogen incorporation and a saturation value of $\sim 0.9 \cdot 10^{16} \text{ cm}^{-2}$.

At a first glance and from the viewpoint of ion-surface interaction, the lower nitrogen incorporation from the Xe/N_2 mixture is surprising, since magnetron operation at ~ 570 V

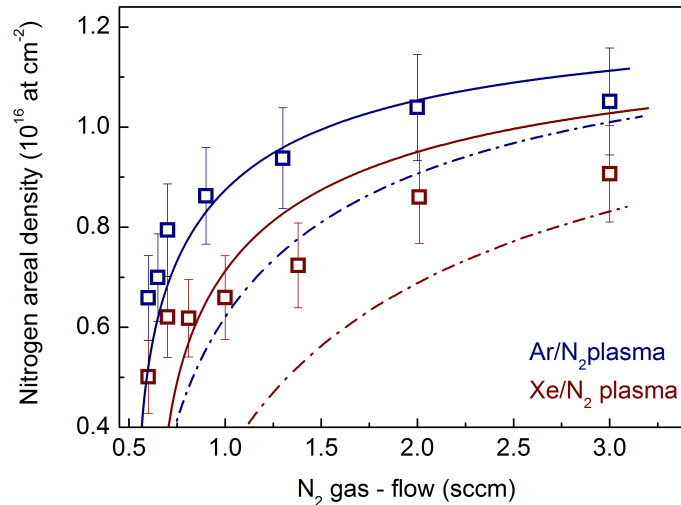


Figure 6.1: Stationary nitrogen areal density versus reactive gas flow measured in the target race track during Ar/N₂ and Xe/N₂ magnetron sputtering, from experiment (squares) and simulation data (lines). The simulation data have been obtained assuming a sticking coefficient of nitrogen molecules of 1 (solid lines) and 0.3 (dashed-dotted lines). During magnetron operation, the inert gas flow was 10 sccm, the total pressure about 0.3 Pa, and the magnetron current 0.3 A.

for Xe/N₂ plasma should cause larger penetration depth of the ionized species and thereby increased nitrogen concentration at saturation. However, as it is shown in figure 3.5 the range of 250 eV nitrogen ions originating from the Xe/N₂ plasma exceeds that one of 175 eV ions from the Ar/N₂ plasma only to a minor extent. Furthermore the range of 570 eV Xe ions is considerably larger than that of 350 eV Ar ions. From this one would expect an amplified contribution of nitrogen recoil implantation, since the higher energy of Xe ions would extend the nitrogen depth profiles to larger depth and thereby increase the areal densities at saturation. However, the energy transfer (cf. equation (2.14)) in a xenon-nitrogen binary collision is only half compared to that one of an argon-nitrogen collision. Therefore the higher energy of Xe ions does not extend the nitrogen depth profiles through recoil implantation. The lower nitrogen incorporation in the Xe case is mainly due to the higher electron impact ionization cross section of Xe as it is shown in figure 2.3. This involves, compared to the Ar case, a higher ratio of inert ion flux to reactive ion flux. Since sputtering is mainly determined by the inert gas ions, the target erosion is enhanced for the Xe/N₂ plasma. This results in a shallower stationary nitrogen depth profile and thereby in a reduced total nitrogen amount. Furthermore, the enhanced sputtering keeps the target surface metallic even at slightly higher nitrogen flows, what reduces the nitrogen incorporation due to recoil implantation in particular at low and intermediate flow values.

Figure 6.1 additionally includes simulation data as obtained from the two-layer model. For the zero-coverage, sticking coefficients of molecular nitrogen, of 0.3 and 1 have been inserted into the simulations. As described in section 3.3.5, the value of 0.3 is considered as the best choice, derived from from experimental data.

For sputtering with both inert gases, the abrupt increase as well as the saturation values

of nitrogen areal densities are well reproduced by the modeling results, although the relative difference between sputtering with Ar and Xe inert gas are somewhat smaller from the modeling. In particular the calculated nitrogen content for Xe/N₂ operation exceeds the experimental data and shows a maximum deviation of $\sim 15\%$ in the present range of reactive gas flows. For the calculation of nitrogen areal densities in both cases, Ar and Xe sputtering, a maximum layer thickness of 2.5 nm has been assumed. This is reasonable since the higher particle energies during sputtering with xenon are compensated by a smaller energy transfer in xenon-nitrogen collisions. As explained above this reduces in particular the recoil implantation depth of nitrogen. Differences in the simulated nitrogen areal densities between Ar and Xe sputtering originate mainly from different values for the sputtering yields ($Y(\text{Ar})$ and $Y(\text{Xe})$), the differences in the yield of recoil implantation ($Y_r(\text{Ar})$ and $Y_r(\text{Xe})$) and from the higher electron impact ionization cross section of Xe compared to Ar ($\sigma_{Xe}/\sigma_{Ar}=2.3$) (cf. figure 2.3 and table 6.1). [21] Uncertainties for the calculated areal densities and especially for the relative difference between argon and xenon operation may arise therefore mainly from the estimation of the ion penetration depth and from the determination of the above listed yields (cf. section 3.3.2).

The results of modeling agree better with the experimental data with a unity sticking coefficient of molecular nitrogen, rather than a value of 0.3 which would be preferable according to experimental data. However, in view of the approximations involved in the model, any preference for the sticking coefficient cannot be derived.

In summary the agreement between the experimental data and model results not only for the individual gas mixtures but also for the relation between both can be regarded as surprisingly good. Deviations from experimental data may arise from the plasma description, which probably comprehends errors larger than 10 %. Errors of the electron impact ionization cross section of plasma species and simplifications of the various particle fluxes towards the target inhibit e.g. in that order of magnitude. Also for the collisional description of the surface interaction with TRIDYN computer simulation errors have to be taken into account, which are larger than the order of 10 %.

Table 6.1: Comparison of parameters, which are used for modeling of nitrogen areal densities versus nitrogen gas flow, displayed in figure 6.1

Parameters	Ar/N ₂	Xe/N ₂
layer thickness	2.5 nm	2.5 nm
Y_{mm}	0.45	0.54
Y_{mc}	0.07	0.07
Y_{gc}	0.28	0.27
Y_r	0.53	0.6
$\sigma_{Ar,Xe}$	2.7	6.3

6.2 Lateral variation of target poisoning

As a consequence of the strongly nonuniform appearance of the magnetron discharge also a nonuniform target poisoning is expected. Therefore laterally resolved *in situ* ion beam analysis has been performed in order to quantify the nitrogen incorporation at the target surface.

For a comparison of the laterally resolved ion beam measurements with the conditions of fluxes towards the target, figure 6.2(a) again shows the radial distribution of the ion current density across the target surface. The current density varies between about 1 mA/cm² and 50 mA/cm² at the target center and the centerline of the racetrack, respectively, and vanishes towards the target edge.

There is a qualitative anti correlation between the distribution of the ion current and the nitrogen areal densities shown in figure 6.2(b). The latter represent stationary distributions after sufficiently long operation time for each parameter setting. To achieve stationary state, the eroded thickness should well exceed the thickness of the nitrated layer. With a sputter yield around 0.4 according to TRIM [60] computer simulations, a current density of about 1 mA/cm² corresponds to sputter removal of $2.5 \cdot 10^{15}$ atoms/(cm²s). Thus, with the observed nitrogen areal density of $\sim 1 \cdot 10^{16}$ /cm², the stationary state is achieved within about 10 s even at the target center.

Figure 6.2(b) shows that the average nitrogen incorporation increases at increasing nitrogen gas flow. At the target center, the nitrogen areal density appears to saturate except for the lowest nitrogen flow. When neglecting sputtering, an upper estimate of the saturation areal density can be obtained assuming the formation of stoichiometric TiN within the range of the incident reactive gas ions. The dominant reactive ion species from the discharge is N²⁺, which, after acceleration by the target voltage and upon impinging the surface, splits into two atoms of half energy. The range distribution of the resulting ~ 175 eV N atoms extends to about 2.5 nm (cf. figure 3.6), which corresponds to a nitrogen areal density of $1.25 \cdot 10^{16}$ /cm² in good agreement with the experimental result.

Towards the centerline of the racetrack, the nitrogen incorporation decreases by ~ 45 % and ~ 10 % for the lowest and highest nitrogen flow, respectively. The radial position of minimum nitrogen incorporation is in good agreement with that of maximum current density. Further towards the edge of the target, the nitrogen areal density increases again in accordance with the decreasing ion flux. However, for the largest nitrogen flows, it increases to a level which is significantly above the saturation level at the target center, although the current density is similar. We ascribe this to some redeposition of Ti and corresponding compound formation in this outer area, although the transport mechanisms of redeposition are not obvious. The redeposition of sputtered material at the edge of the erosion zone has been reported by Rosnagel [73] and is described there by gas phase collisions between sputtered material and inert gas atoms, due to variations in the gas density near the magnetron cathode.

As mentioned in section 3.3.2, the stationary reactive gas incorporation results from a balance of reactive gas deposition and sputter erosion. The three major mechanisms of reactive gas accumulation are chemisorption of reactive gas molecules at the surface, direct implantation of ionized reactive species, and recoil implantation of the chemisorbed species by ion bombardment. Recoil implantation and sputter erosion are mainly due to inert gas ions, as

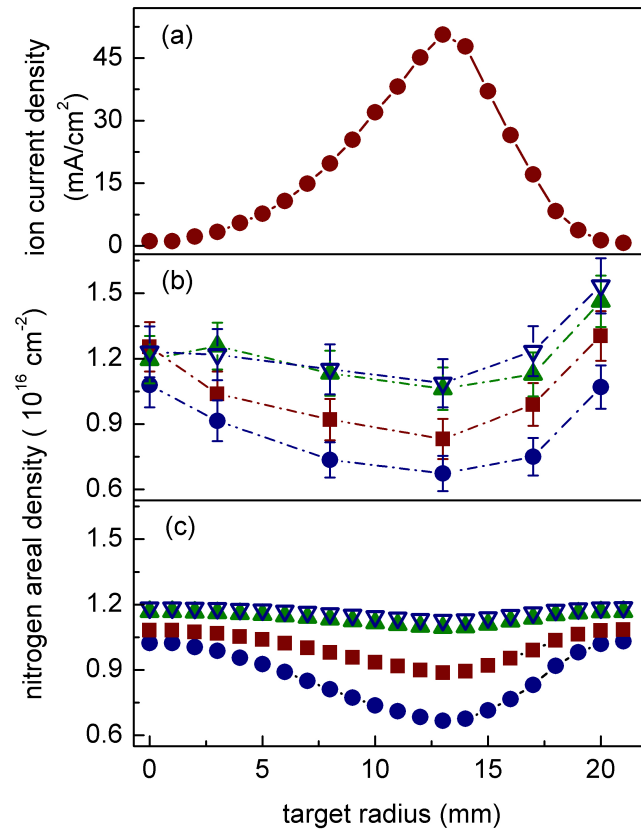


Figure 6.2: Radial distributions of the ion current (a) and of the nitrogen areal density at the target surface at different nitrogen flows [(b) and (c)], as determined from ion beam analysis (b) and from model calculations (c). For (b) and (c), the nitrogen gas flows are 0.65 sccm (dots), 1 sccm (squares), 2 sccm (full triangles), and 2.5 sccm (open triangles). The lines are added to guide the eyes.

the nitrogen addition is relatively small and the electron-impact ionization cross sections of Ar is larger than the one of N₂. [40,41]

As also discussed in figure 3.3 of section 3.2.1, all ion fluxes, and thereby the sputter erosion, follow the radial current distribution of figure 6.2(a), whereas the molecular gas flux arrives uniformly across the target. Thus, if adsorption in connection with recoil implantation plays a significant role for deposition, the deposition-erosion balance is shifted towards erosion in the center of the race track compared to the target center and edge, which results in a reduced nitrogen incorporation.

In order to corroborate this picture again quantitative model calculations have been performed. The compound formation at the surface is modeled by chemisorption of incident reactive gas molecules assuming an unity sticking coefficient on the metallic fraction of the surface. Rather than deriving the reactive gas partial pressure from modeling of the total system gas consumption as introduced in chapter 3.3, it has here been measured by means of the mass spectrometer for each setting of reactive gas flow. This allows to consider only the particle balance situation at the target and makes assumptions concerning the reactive gas exhaust and substrate area dispensable.

Of ions, only Ar⁺ and N₂⁺ are taken into account, which are dominant in the discharge according to the electron-impact ionization cross sections. [40,41] The radially varying total (Ar⁺ plus N₂⁺) ion flux is taken from the radial distribution of figure 6.2(a) as derived from measurements, introduced in section 3.2.1. Furthermore the Ar⁺ to N₂⁺ flux ratio and the yields of surface sputtering and recoil implantation are derived as described in chapter 3.3.

Figure 6.2(c) shows the model prediction of the nitrogen incorporation versus the target radius. At the target center, the experimental results of figure 6.2(b) are reproduced quantitatively. As discussed above, the discrepancy at the target edge is attributed to redeposition of sputtered target material. The sequence of the radial dependencies at different reactive gas flow shows good qualitative agreement between experiment and model results, although the shape of the radial dependencies appears somewhat different with a narrower depression in the race track obtained from the model. In particular for the highest nitrogen flow, the predicted reduction of nitrogen incorporation in the center of the race track is in excellent agreement with the experiment.

The inspection of the nitrogen depth profiles obtained from the model shows that the saturated areal density is associated with the formation of a stoichiometric layer, whereas in the non-saturated region around the race track centerline a constant, sub-stoichiometric nitrogen concentration extends from the surface into the depth. In view of the good agreement with the model results, this picture can be applied with some confidence also to the interpretation of the experimentally observed areal densities.

In the framework of the above modeling, figure 6.3 illustrates the relative contributions of the mechanisms of nitrogen incorporation at different reactive gas flows and target locations, as calculated for the stationary state. In the present range of reactive gas partial pressure, combined chemisorption and recoil implantation dominates over direct ion implantation. This is consistent with the high gas-kinetic flux of nitrogen molecules relative to the flux of N₂⁺ ions, and an efficient transfer of the chemisorbed nitrogen by recoil implantation

into the bulk. At increasing nitrogen partial pressure, the relative contribution of direct ion implantation increases, as the surface becomes increasingly saturated. The latter limits the rate of chemisorption of gas molecules at the surface, and thereby the inward flux by recoil implantation. Comparing the two lines of figure 6.3, the relative contribution of direct ion implantation is somewhat higher in the race track. However, the difference is surprisingly small in view of the ion current distribution, which varies by more than one order of magnitude. This is again attributed to the limitation of combined chemisorption and recoil implantation, which occurs preferentially at the target center and edge. The high ion bombardment in the race track not only increases the relative contribution of direct implantation of reactive ions, but also transfers chemisorbed nitrogen efficiently to the bulk by recoil implantation, so that a high rate of chemisorption is sustained.

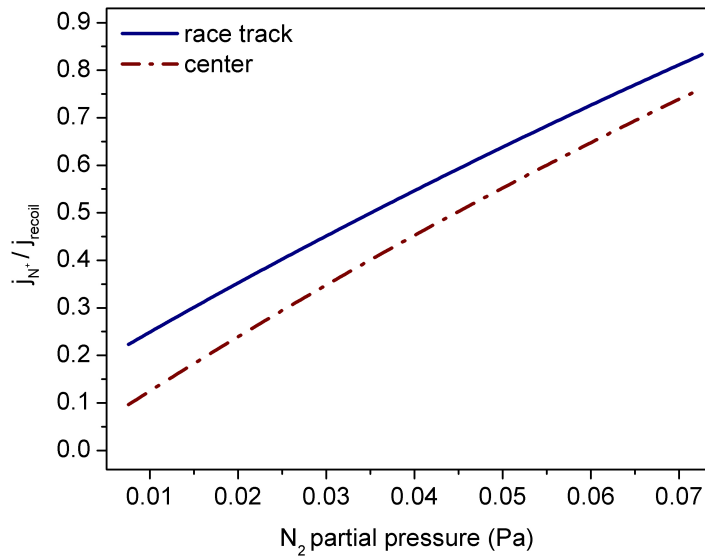


Figure 6.3: Ratio of nitrogen injection by direct ion implantation and recoil implantation from the surface layer vs the nitrogen partial pressure for different target locations. j_N^+ and j_{recoil} denote the respective atomic nitrogen fluxes. The partial pressure of 0.07 Pa corresponds to a reactive gas flow of 2.5 sccm.

7 Results and discussion II (Mass spectrometry)

7.1 Plasma characterization by means of mass spectrometry

The following sections introduce measurements in order to characterize the plasma properties like its composition, the relative amounts of the various species and the potentials arising from the discharge. Thus the results of plasma monitoring are a basis which will be used for the interpretation of the experiments, introduced in section 7.2.

7.1.1 Appearance of the magnetron plasma

Figure 7.1 shows a schematic picture of the optical appearance of the plasma, with strong light intensities being emitted not only from the plasma race track, but also from a plume that originates from the target center. The latter is ascribed to the ionization and excitation by energetic secondary electrons, which are emitted from the target center and accelerated by the operation voltage in the sheath above the target. These electrons, unlike the ones being emitted in the zone of the plasma race track, are not trapped by the magnetic field, but escape along the center field lines, creating there a plasma with a relatively high electron temperature and which reaches the substrate position, whereas the thin, afterglow-like plasma at the substrate position above the race track is only fed by diffusion.

7.1.2 Mass spectrum at deposition conditions

Figure 7.2 shows a typical mass spectrum obtained with the mass spectrometer operated in RGA mode at fixed energy in order to detect particles with thermal energies. The spectra were recorded during magnetron operation in an Ar/N₂ atmosphere (red bars) and with the magnetron switched off (blue bars), respectively. The gas flows into the chamber were kept constant during both measurements. An argon flow of 10 sccm and a nitrogen flow of 0.6 sccm results in a total pressure of about 0.3 Pa. During magnetron operation, the spectrum includes additional contributions from plasma ions. Since the spectrometer efficiency is higher for these ions, a enhanced yield for e.g. Ar and N₂ during magnetron operation

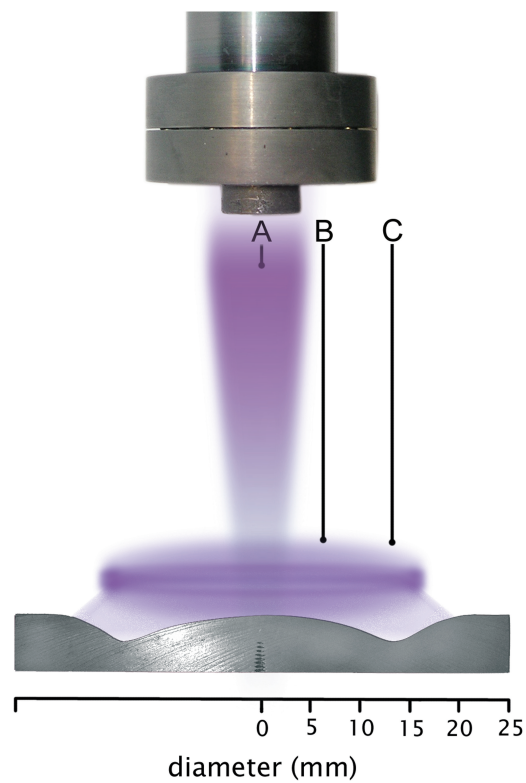


Figure 7.1: Cross section of the magnetron target with the characteristic erosion zone below the plasma race track, and the appearance of the plasma (schematic drawing). Three regions are indicated: A) the target center, from which the plasma extends towards the substrate due to the unbalanced magnetron field configuration, B) the outer target center and C) the target race track.

can be observed. In the present mass range, signals are obtained from sputtered titanium with a mass to charge ratio of 48 amu/q, and the main species in the discharge like Ar^+ at 40 and 36 amu/q, Ar_2^+ at 20 amu/q, N_2^+ at 28 amu/q and N^+ at 14 amu/q. In addition, the spectrum contains impurities of the gas which are, e.g. CO_2^+ at 44 amu/q, CO^+ at 28 amu/q, H_2O at 18 amu/q, and a large signal of H^+ at 1 amu/q which appears only during the discharge. This indicates that H atoms mainly originate from dissociation processes of H_2O , OH and C_XH_Y impurity molecules within the plasma. The latter molecules are seen as groups in the ranges 27-30 amu/q and 38-43 amu/q. Since the parameters of the spectrometer were optimized in order to detect particles with thermal energy the yield of sputtered Ti, which have a higher average energy, is comparably low.

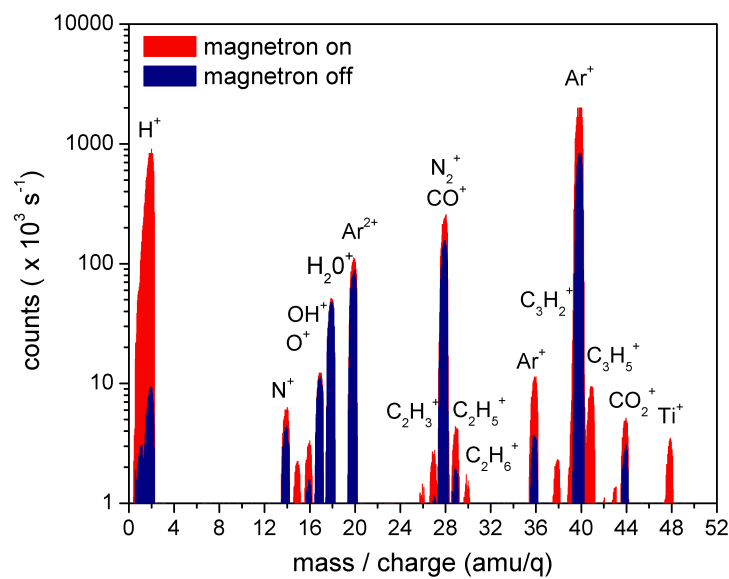


Figure 7.2: The typical mass spectrum measured in RGA mode, results from the plasma constituents Ar and N_2 , sputtered Ti atoms, and CO_2 , H_2O and C_XH_Y impurities. During deposition (red bars) the magnetron was operated at a total pressure of ~ 0.3 Pa, an N_2/Ar gas flow ratio of 0.06, and a target current of 300 mA resulting in a discharge voltage around 340 V. For the switched off magnetron the signal arising from sputtered Ti atoms disappears and the yield of Ar and H is significantly reduced. The parameters of the spectrometer were set in order to obtain neutral atoms and molecules at thermal incident energy.

7.1.3 Behavior of reactive gas partial pressure during sputtering

In reactive sputtering the relation between reactive gas flow and its partial pressure turns out as very complex. In general one can not control the deposition process and thin film stoichiometry by applying a certain flow ratio of inert and reactive gas. Often the ratio of gas partial pressures is influenced by various parameters and may deviate significantly from the adjusted flow ratio. The behavior of reactive gas partial pressure during sputtering is

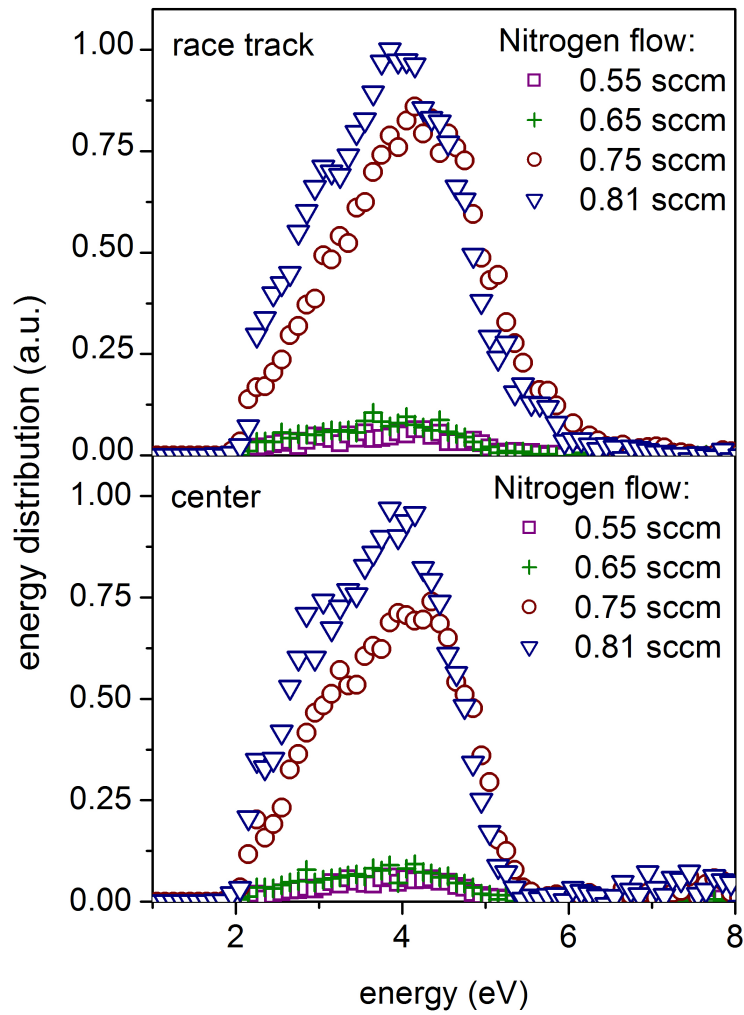


Figure 7.3: N_2^+ energy distribution functions at different N_2 -flow as measured at race track and center position of the target

issue of the here introduced measurement.

Figure 7.3 shows energy distributions of neutral Nitrogen molecules (N_2) obtained for the outer target center and the race track position of the magnetron target. The maximum of the EDF is around 4 eV independent of the observed target position and nitrogen flow. This is roughly consistent with a merely thermal motion of the particles, taking into account the 3 eV acceleration inside the mass spectrometer. From this it is concluded that N_2 mainly originates from the filling gas which is detected after direct ionization as (N_2^+) in the mass spectrometer. Any ion generated in the plasma would be accelerated in the plasma boundary accordingly to equation 2.52, which is not observed.

A major effect of target poisoning is the well known increase of partial pressure of the reactive gas at critical gas flow. This is reflected in figure 7.3, where the yields of detected N_2 species show a sudden increase of partial pressure by a factor of ~ 10 at a N_2 gas flow from 0.65 sccm to 0.75 sccm only. Even if the phenomena of this increase is well understood and can be described by modeling, the experiment shows impressively, how the reactive gas partial pressure may vary by one order of magnitude. It confirms the difficulties in thin film processing that arise from such instabilities especially in terms of achieving a desired layer stoichiometry.

7.1.4 Determination of plasma potential

Properties like microstructure, texture and stoichiometry of thin films are influenced by the average energy per deposited ion. Petrov et al. found that this average energy strongly depends on the flux ratio of sputtered and in the plasma ionized particles to sputtered neutrals (j_i/j_n) [74]. Thus the deposited energy further is affected by the potential drop in the sheath between plasma and substrate, where ionized particles will be accelerated towards the substrate. The knowledge of the plasma potential therefore can become of interest for the characterization of the deposition process.

As described in section 2.4, due to the different velocities of ions and electrons, the formation of an electrostatic potential takes place between plasma and a surrounding wall, which, e.g., is the substrate. Ions, which entering the sheath region between plasma bulk and substrate (see figure 2.5), get accelerated by the electrostatic field. Since the probe of the mass spectrometer, which extends into the plasma (c.f. figure 4.1) acts also like a grounded substrate, the formed potential can be determined by measuring the energy distribution functions (EDF) of plasma ions arriving at the probe. In the current setup the energy of ions is given by the floating potential $E_i = e\Phi_{fl}$. Thus, by measuring the EDF of plasma ions the electron temperature and plasma potential can be derived from equations (2.52) and (2.46).

Figure 7.4(a) shows EDF's of titanium ions as obtained with the mass spectrometer during magnetron operation in pure argon atmosphere. Since sputtered ions would not escape from the negatively biased magnetron target, it can be concluded that the yield of titanium ions originate from sputtered neutral atoms, which are ionized within the plasma. It is noted, that the integrated yield of titanium ions is direct proportional to the applied magnetron target current.

The measured EDF's show a maximum for the lowest power at an ion energy of around 5.5 eV, which increases slightly at higher magnetron powers. Furthermore a long high-

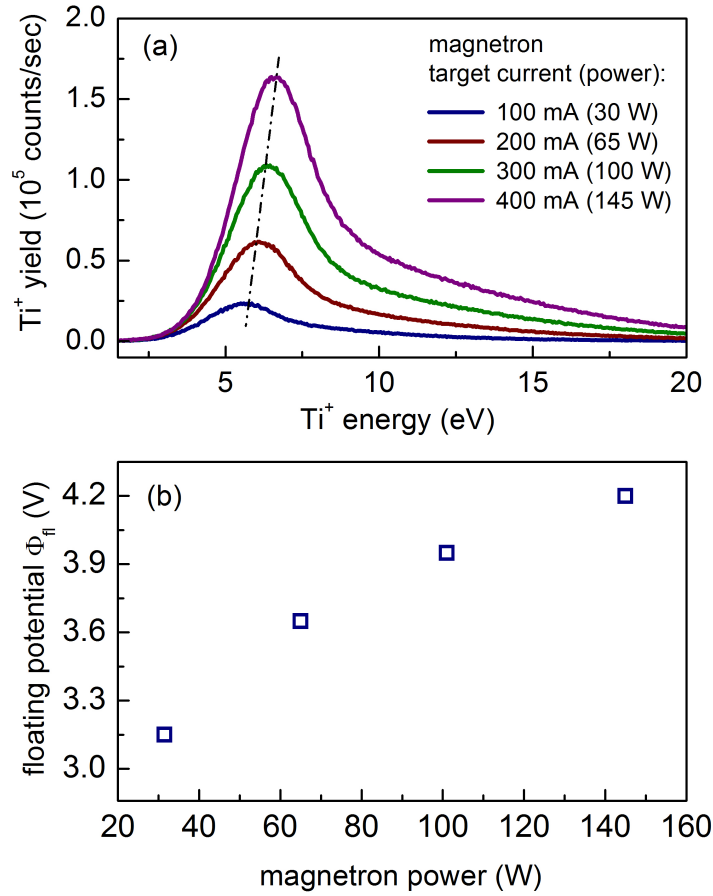


Figure 7.4: Ti energy distribution functions at different magnetron powers (a) and derived plasma potentials versus magnetron power (b)

energy tail is visible, which, however is much less pronounced than it is expected from Thompson sputter theory. (Most recent investigations of the angular and energy distribution of sputtered particles, gave evidences, that these deviations from Thompsons theory might be caused by a texture of the Ti sputter target, which is given by the fabrication process.) According to the Thompson formula (eq. (2.66), page 29) sputtered particles exhibit an EDF that possesses a maximum at half of the surface binding energy U_S of the sputtered material. This has to be regarded in the determination of the plasma potential from EDF's of sputtered particles. The maximum of the EDF as obtained from the mass spectrometer can be observed than at an ion energy $E_i = e\Phi_{fl} + U_s/2$.

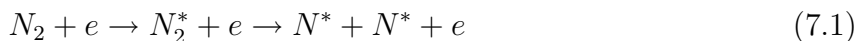
Figure 7.4(b) show the floating potential versus magnetron power, as derived from the peak positions of the EDF's in 7.4(a). With the surface binding energy of pure titanium $U_S = 4.9$ eV, the floating potential results from the maximum in the EDF, $E_{i,max}$ (eV) reduced by $U_S/2 = 2.45$ eV. In the present range of magnetron power, the potential varies between 3.15 V and 4.2 V. According to equation (2.52) the electron temperature in the plasma is

approximately 1 eV, which is reasonable for low temperature discharges [20].

7.1.5 Threshold ionization mass spectrometry of N-radicals

In order to distinguish the role of different plasma species and their contribution to target poisoning, the fraction of radicals within the Ar/N₂ plasma will be determined using the so called threshold ionization mass spectrometry (TIMS). This technique has been applied by several groups e.g. for characterization of SiN_x deposition [75–77].

The experiment is carried out in addition to the modeling of the radicals flux, introduced in section 3.1, which allows to evaluate the model results again. In the magnetron discharge of an Ar/N₂ gas mixture at a pressure of 0.3 Pa, nitrogen radicals are generated primarily in electron impact reactions. The electron impact **dissociation** reaction



leads to an electronically excited state of N₂ that subsequently dissociates into atoms with the release of translational energy, represented here by (*).

In the **dissociative ionization**



the knock on electron of the molecule is excited into an anti-binding state or to an higher energy level of the molecule which allows auto-dissociation.

In both cases predissociation of vibrational molecule levels produces a discrete release of translational energy to the atoms. However, while the cross section of the N₂ dissociation reaction are well known, only little information about the energy of the reaction fragments is available. For the N₂ molecule three vibrational levels can be observed and furthermore three low lying energy states need to be considered, the ⁴S ground state and two metastable states, ²SD and ²SP, respectively. From the possible combination of these states, the production of N(²D) + N(⁴S) states is the dominant dissociation channel in N₂ dissociation found by Cosby, where the two dissociates atoms posses kinetic energies of 0.797 eV and 1.071 eV, respectively. [42]

During mass spectrometry, the N radicals and N₂ molecules reaching the spectrometer can be separated due to their different ionization thresholds. The ionization of N radicals (N+e → N⁺+2e) posses a threshold energy of E_i = 15.2 eV [78], whereas dissociative ionization of N₂ molecules (N₂+e → N⁺+N+2e) demands an electron energy E_{di} >25.3 eV. [42] By scanning the energy of electrons, emitted by the filaments in the ionization source of the mass spectrometer, a significant change in the yield at a mass-over-charge (m/q) ratio of 14 can be expected at the respective threshold energies. This allows to distinguish between the different production processes of N radicals and with the knowledge of the cross sections σ_i(E) and σ_{di}(E) for ionization and dissociative ionization, respectively, the ratio N/N₂ can be established.

Figure 7.5 displays the yield of N radicals (m/q = 14) in a logarithmic scale versus the electron energy, as obtained with the mass spectrometer during magnetron operation in

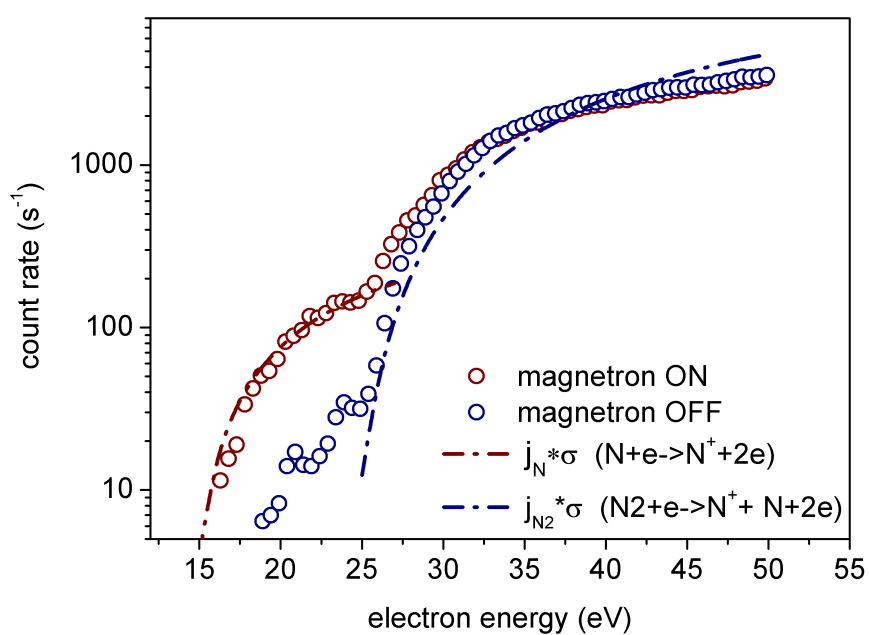


Figure 7.5: Detection of N radicals by threshold ionization mass spectrometry. The measurement was performed with the magnetron switched on (red circles) and off (blue circles), respectively. The experimental data are fitted using the cross sections for ionization of radicals (red dashed-dotted line) and for dissociative ionization (blue dashed-dotted line).

an Ar/N₂ gas mixture at ~20% nitrogen addition. The scan during magnetron operation (plasma on) shows the abrupt rise of the radicals signal at an electron energy of around 15 eV. In the discharge generated radicals, get ionized inside the mass spectrometer and can be detected, starting from that electron energy. A second rise in the N yield can be observed at an energy of around 25 eV. Now the electrons emitted from the filaments cause the dissociative ionization of N₂ molecules.

For the second measurement, shown in figure 7.5 all conditions were kept constant and only the magnetron was switched off. It can be seen, that the large signal of radicals appears only for electron energies above 25 eV. In the absence of the discharge no radicals are created outside the spectrometer, which could be detected at lower electron energies. Again at an energy of 25 eV the dissociative ionization of N₂ molecules starts inside the spectrometer. There is a small signal at lower energies, which can be attribute to the release of atomic nitrogen from the hot filaments or the dissociation/ionization of C_xH_y impurities in the plasma (see figure 7.2).

The flux ratio j_N/j_{N_2} can be derived from the measured yields of N radicals $Y(N)$ and N₂ molecules $Y(N_2)$, respectively. It is

$$\begin{aligned} Y(N, E) &= \sigma_i(E)j_N P_I(N) \\ Y(N_2, E) &= \sigma_{di}(E)j_{N_2} P_I(N_2) \end{aligned} \quad (7.3)$$

Due to the different translational energies of N and N₂ in the plasma the particle fluxes, although has to be corrected by the ionization probabilities inside the mass spectrometer P_I . The probability scales with the inverse of of particle velocity (see sec. 5.2.2), which yields

$$P_I(N) \propto 1/\sqrt{E_N} \quad \text{and} \quad P_I(N_2) \propto 1/\sqrt{E_{N_2}} \quad (7.4)$$

The cross sections for ionization $\sigma_i(E)$ of radicals and dissociative ionization $\sigma_{di}(E)$ of molecules are taken from reference [42]. The energy dependence $\sigma(E)$, which is shown in figure 3.1, can be approximated by the polynomials

$$\sigma_i(E) = \sum_{k=1}^9 a_k \log(E^k(e)) \quad \text{and} \quad \sigma_{di} = \sum_{k=1}^9 b_k \log(E^k(e)) \quad (7.5)$$

where the coefficients are

$$a_k = \begin{pmatrix} 44.95 \\ -48.88 \\ 16.27 \\ 0.09 \\ -1.29 \\ 0.33 \\ -0.04 \\ 2 \cdot 10^{-3} \\ -6 \cdot 10^{-5} \end{pmatrix} \quad \text{and} \quad b_k = \begin{pmatrix} -712.12 \\ 1201.33 \\ -860.76 \\ 342.11 \\ -82.56 \\ 12.40 \\ -1.13 \\ 0.06 \\ -0.001 \end{pmatrix} \quad (7.6)$$

Figure 7.5 shows the fit of the experimental data by applying equations (7.3). Inserting the above introduced cross sections (7.5), the energies of dissociated N atoms $E(N) \approx 1$ eV and the energy of N_2 molecules $E(N_2) \approx 50$ meV into equations (7.3), yields a flux ratio

$$\frac{j_N}{j_{N_2}} = 0.09 \quad (7.7)$$

which is in very good agreement with the result of 0.08 which was found by plasma modeling in section 3.2. The result approves again, that during reactive sputtering in an Ar/ N_2 atmosphere the adsorption of nitrogen molecules at the target surface plays a major role in target poisoning, whereas the role of the radical flux can be neglected.

7.2 Energy distribution functions of sputtered Titanium

The microstructure of thin films is often beneficially influenced by fast particle bombardment during growth [79–81]. Bombardment at some ten eV may increase the surface mobility of adatoms and simultaneously avoid bulk damage of the growing film [82], and thus, e.g., lead to densification of the growing film [83]. Being a well established tool for industrial production of thin films, magnetron sputtering delivers sputtered neutrals with a mean energy in the desired range (~ 20 eV) due to the physics of particle-solid interaction [25, 28]. An additional energetic particle flux is provided by the plasma ions. Petrov et al. have shown, that the microstructure e.g. film density and grain size of the growing film, is not only affected by the energy of impinging ions but also by the ratio j_i/j_n of ion to neutral particle fluxes, arriving at the substrate [84, 85]. Since magnetron discharges are laterally strongly non-uniform (see figure 7.1) due to the electron confinement, a laterally non-uniform particle bombardment of the growing film with a varying flux ratio of j_i/j_n at the substrate position is expected.

In addition, in case of reactive sputter deposition, the reactive gas incorporation at the target varies significantly across the surface, as shown in section 6.2. This may influence the energy distribution function (EDF) of sputtered particles, as the compound formation results in a variation of the surface binding energy of target material [86, 87].

Although particle fluxes from sputter magnetrons at the substrate position have been studied in numerous papers, [13, 47, 71, 87–95] the lateral variation has only been addressed in an early measurement of electrical currents across the substrate [87]. Therefore, the present work aims at investigating the lateral variation of particle fluxes at the substrate position by means of energy-resolving mass spectrometry.

7.2.1 Operating details of mass spectrometry

The mass spectrometer was run in two different operation modes in order to separate neutral and ionized particles. In residual gas analysis (RGA) operation with the ionization filaments

inside the mass spectrometer being switched on, incident neutral atoms, which are ionized in the spectrometer, and ions originating from the magnetron discharge are simultaneously detected. To separate the signals arising from the neutrals and the plasma ions, the spectrometer was alternatively operated in ion analysis (IA) mode with the ionization filaments being switched off, but all other settings of the ion optics kept constant. In this case only ions produced in the plasma are detected, so that the energy spectra of neutrals can be derived as the difference of the data acquired in the RGA and IA modes.

It should be noted that all particles gain an additional energy from a 3 V extraction potential inside the mass spectrometer. The spectra presented below have been corrected accordingly.

Furthermore obtained energy distributions of sputtered particles have been corrected accordingly to the details given in section 5.2.2.

7.2.2 Results

Non-reactive sputtering

In figure 7.6 EDF's of sputtered titanium atoms are displayed, as measured from the target race track and center positions. The data were taken during sputtering in pure argon without additional nitrogen flow. Significant differences between both locations are observed, with the average energy being clearly lower in the race track. Further, at the center the IA distributions do not differ significantly from the RGA ones, so that a reliable extraction of the energy spectrum of neutrals is not feasible. In contrast, a pronounced additional low energy peak from neutrals is obtained at the race track position.

Reactive sputtering

In order to obtain a reliable measurement of the energy distributions of sputtered titanium neutrals, the outer center position B (see figure 7.1) was chosen which still exhibits low erosion at the target, but passes by the central plasma plume.

Figure 7.7 shows the corresponding energy distributions of sputtered titanium neutrals in comparison with the race track position, being recorded during reactive deposition mode for different reactive gas flows. Again, clear differences between the two positions are found. The energy distributions from the race track show no distinct variation in shape and peak energy, which is constant at around 2.4 eV, in agreement with the data displayed in figure 7.6(a). There is a small increase of the sputter yield at increasing nitrogen flow, which may be attributed to the slight increase of target voltage after nitrogen addition. Under the same conditions, the measurements toward the target center show a significantly different behavior. With increasing nitrogen flow, the yield of sputtered Ti decreases. Furthermore, the peak maximum of the EDF shifts from 2.5 eV to 3.9 eV when increasing the reactive gas flow from 0.55 sccm to 0.75 sccm. A further increase of the reactive gas flow leaves the EDF unchanged.

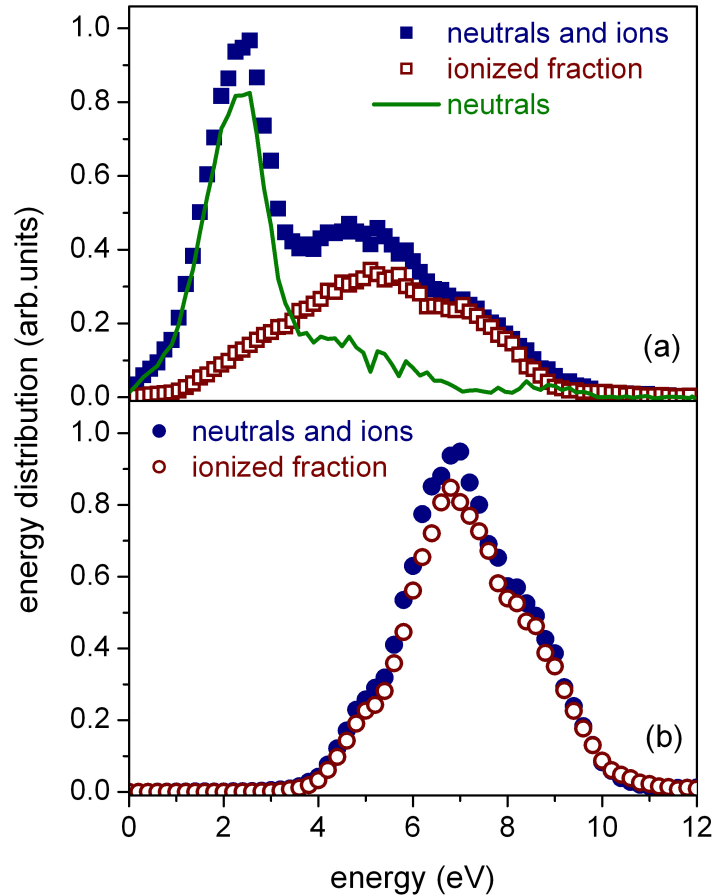


Figure 7.6: Energy distributions of Titanium sputtered from the target race track (position C of figure 7.1)(a) and the center (position A of figure 7.1) (b). The data represent the total amount of detected particles measured in RGA mode (full symbols) and the fraction of ionized species from the plasma (open symbols), as measured in IA mode with the filaments of the mass spectrometer being switched off. The solid line results from subtracting the IA yields from the RGA yields.

7.2.3 Discussion

The above results demonstrate a significant variation of the energy distributions measured at the substrate position in dependence on the emission region at the target. These non-uniformities may arise from both the local conditions at the target surface and the interaction of the particles with the plasma during their passage toward the analyzer. Starting with the latter, first it is stated, that positive ions cannot originate from the target surface, since they would be retained by the DC voltage between the plasma and the target. Thus, ions of sputtered material exclusively result exclusively from ionization in the plasma. From the similarity of the RGA and IA measurements at the center position (see figure 7.6(b)), the ionized fraction from there is significantly higher than from the target race track. This can be attributed to the ionization of neutral Ti atoms in the central plasma jet (see figure 7.1), which is due to the present unbalanced magnetron configuration. However, the contribution of these ions to the total energy balance at the target is small as the erosion yield from the center is small compared with the race track. Nevertheless, the effect of increasing the ion flux to the substrate in an unbalanced magnetron is well known [87,88] and is employed to increase the energetic particle bombardment of the substrate [34].

To explain the significant differences in the peak energies of the ion EDF's between the center and the race track, it is noted that the high electron temperature in the central plasma jet leads to an increased plasma potential and thus to an increased kinetic energy of the ions that impinge on the substrate. The change in plasma potential by applying balanced versus unbalanced magnetron configurations has also been reported by Hippler et al. [96]. The energy of ions from the central region might be further increased by ambipolar acceleration in an inhomogeneous magnetic field [97]. The magnetic moment $\mu = W_{\perp}B$ of an electron moving in a magnetic field B with a gyration energy W_{\perp} remains constant. Along the field lines in the center of the unbalanced magnetic field configuration, B decreases towards the substrate. Thus, for energy conservation, the electrons gain in energy W_{\parallel} parallel to the magnetic field lines at the expense of the perpendicular energy W_{\perp} . In this simple consideration which neglects the surrounding less dense plasma, the ion flux would follow that of the electrons due to electrostatic traction, which results in an increased energy also of the ions.

In non-reactive mode, there is a pronounced yield of neutrals emitted from the race track position (see figure 7.6(a)), which confirms that their ionization probability is significantly lower than in the plasma plume above the center. Their EDF peaks at around 2.4 eV. This is in accordance with sputter theory [28], with the maximum of the energy distribution being predicted at $E = 0.5 \cdot U^S$, with U^S denoting the surface binding energy. For an elemental substance, U^S is given by the enthalpy of sublimation, ΔH^S . With $\Delta H_{Ti}^S = 4.89$ eV for Ti, the resulting peak energy is in good agreement with the measurement. The mean energy of the ions from the race track position is significantly larger than that of the neutrals, which again is attributed to energy gain in the plasma boundary, which, however, is less than for the center position due to the smaller electron temperature.

The reactive mode results in target poisoning due to the partial or full formation of a TiN

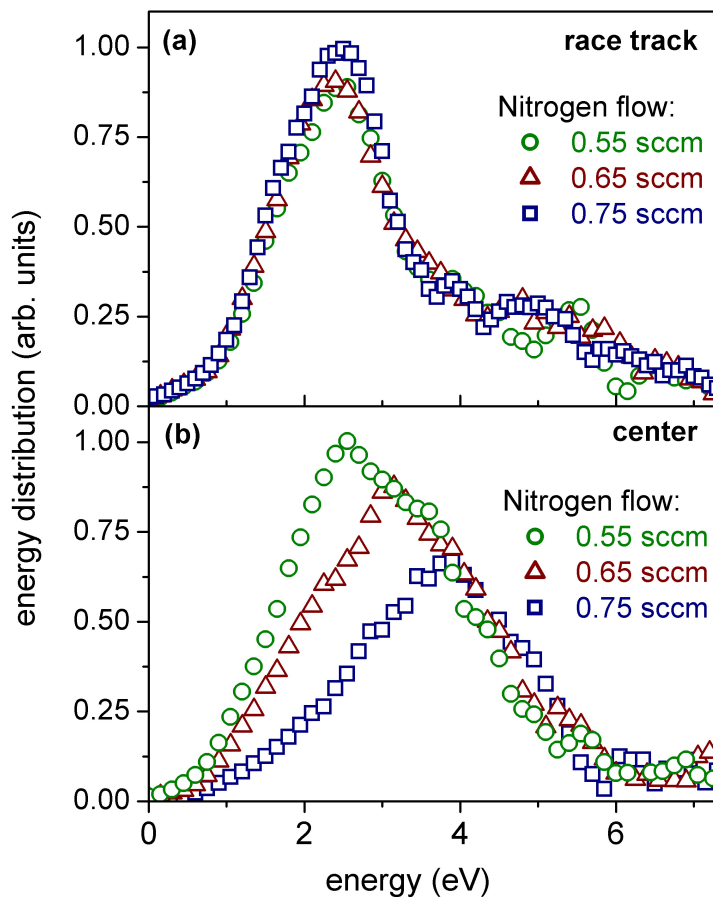


Figure 7.7: Energy distribution of sputtered titanium neutrals measured at different flow rates of nitrogen, i.e. at different states of target poisoning. Locations of the measurements were the target race track (a) and the outer target center (b) (positions C and B in figure 7.1, respectively).

layer on the target surface. Following the particle balance models, introduced in section 3.3, the surface is then composed of a compound fraction and a metallic fraction. For the metallic fraction, the EDF's are then expected to be similar to those obtained in non-reactive mode. This is indeed observed in figure 7.7(a), with a peak energy of ~ 2.5 eV as seen in figure 7.6(a). Moreover, it can be concluded that the race track region of the target remains essentially in metallic mode in the present range of nitrogen flow. This is consistent with the findings in section 6.2, where a strongly non-uniform target poisoning at sufficiently low reactive gas addition, was also obtained by means of ion beam analysis. Qualitatively, the intensive ion bombardment in the race track region shifts the balance of nitrogen incorporation and sputter erosion toward erosion, so that the compound fraction in the race track remains low compared to the target center.

In contrast, the mean energy of Ti atoms sputtered from the center region increases at increasing reactive gas flow (see figure 7.7(b)). This is qualitatively consistent with an increase in U^S , as the sputtering yield scales linearly with its inverse [28]. A linear model is proposed [99] for the surface binding energies of both components according to

$$U_{Ti}^S = c_{Ti}^S U_{Ti-Ti} + c_N^S U_{Ti-N} \quad (7.8)$$

$$U_N^S = c_{Ti}^S U_{Ti-N} + c_N^S U_{N-N} \quad (7.9)$$

where c_x^S represent the atomic fractions at the surface, and U_{x-y} matrix elements for the binary interaction of the constituents (x,y = Ti or N). This model corresponds to a continuous variation of the surface binding energies with the compound formation. For the pure metal, equation 7.8 results in $U_{Ti-Ti} = \Delta H_{Ti}^S$. In the stoichiometric case with $c_x^S = 0.5$, the sum of both surface binding energies must balance the enthalpy of formation of TiN, ΔH_{TiN}^f , the sublimation enthalpy of Ti, ΔH_{Ti}^S , and half the dissociation energy of the nitrogen molecule, $\Delta H_{N_2}^m$, i.e.

$$\frac{1}{2} (U_{Ti-Ti} + 2U_{Ti-N} + U_{N-N}) = \Delta H_{TiN}^f + \Delta H_{Ti}^S + \Delta H_{N_2}^m \quad (7.10)$$

Assuming a small interaction between two nitrogen atoms incorporated into the surface ($U_{N-N} \approx 0$) results in

$$U_{Ti-N} = \Delta H_{TiN}^f + \frac{1}{2} (\Delta H_{Ti}^S + \Delta H_{N_2}^m) \quad (7.11)$$

Recently, Rosen [100] gave evidence that compound formation is associated with discrete surface binding energies rather than a continuous transition from the pure metal to the stoichiometric compound. Qualitatively, also the present data support this picture, as a continuously varying surface binding energy would be in contradiction with the narrowing of the peak width at increasing nitrogen flow, which is observed in figure 7.7(b). In the above formalism, this translates to

$$U_{Ti}^S = U_N^S = U_{Ti-N} \quad (7.12)$$

for the compound fraction of the surface. Evaluating equation 7.11 results in $U_{Ti-N} = 7.7$ eV, so that the peak of the EDF is expected at ~ 3.9 eV. This is indeed observed in figure 7.7(b) for the highest nitrogen addition, indicating that almost full compound formation has taken place under these conditions at the target center. For the lowest nitrogen flow, the peak energy approaches the one for the pure metal. However, the EDF is significantly broader than that from the race track position, which indicates a fractional compound formation.

Thus, the energy distributions of sputtered Ti atoms demonstrate a transition from a local metallic mode to a local compound at the target center starting around a nitrogen flow around 0.55 sccm. This is in qualitative agreement with the global flux balance models [18, 19, 101] which predict a steep increase of the nitrogen incorporation at a critical value of the reactive gas flow. However, the present results indicate that the transition from metallic mode to compound mode occurs at different reactive gas flows on different locations of the target surface. From this and at a first glance, one might expect a significant broadening of the transition from the global metallic to the global reactive mode, which is not observed in experiments [19, 102]. However, due to the axial symmetry, the race track area contributes much more than the central area of the target to the global balance, so that the latter is mainly determined by the poisoning in the race track.

Following the above picture of discrete binding energies [100], the measured EDF's would be composed of two components, which correspond to the metallic and compound fractions of the surface, with peak energies of ~ 2.5 eV and ~ 3.9 eV, respectively. Accordingly, the distributions of figure 7.7(b) have been decomposed into two Gaussian distributions, with fixed peak energies of ~ 2.5 eV and ~ 3.9 eV. The resulting fits, which are shown in figure 7.8, have been obtained at a fixed width of 1.9 eV for all distributions, which corresponds to the experimental energy resolution. A good fit of the superposed EDF's to the experimental data is obtained, which confirms the validity of discrete surface binding energies. For the lowest nitrogen flow of 0.55 sccm, sputtering from the metallic fraction still dominates. At the higher nitrogen flows, the metallic fraction is significantly reduced in favor of the compound part. At 0.65 sccm, the yields from both surface fractions are about equal, which reflects the gradual transition from metallic to compound deposition mode. For the highest nitrogen flow of 0.75 sccm, the compound fraction largely dominates.

The shift of the peak energy resulting from the outer target center is accompanied by a decrease in sputter yield which merges into a constant low yield at high reactive gas flow, as shown in figures 7.7 and 7.8. According to sputtering theory this is again due to the increase in surface binding energy, and also indicates the development toward a fully poisoned target.

As shown in section 6.2 by measuring the local nitrogen incorporation at the target with the ion beam, a still metallic surface in the race track can coexist with a partially or a fully poisoned area in the center of the target. This is not described by conventional balance models [18, 19, 101] which assume a uniform reactive gas coverage in connection with constant rare and reactive gas fluxes ratio toward the target surface. In the following, results

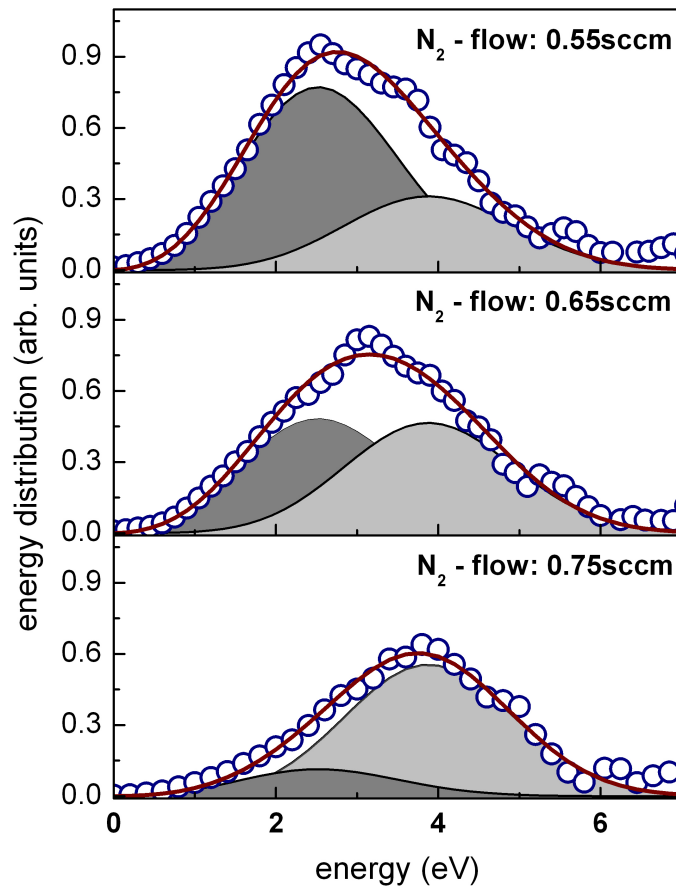


Figure 7.8: Energy distribution of sputtered titanium neutrals (open circles) measured at different flow rates of nitrogen, i.e. at different states of target poisoning. Location of the measurements was the outer target center (position B in figure 7.1). The EDF is decomposed into two contributions as sputtered from the pure metallic fraction (dark grey) and the compound fraction (light grey), respectively.

of the model calculation as described in section 3.3 are shown for the composition of the surface monolayer, as this represents the main origin of sputtered particles. (It is noted that, since there is no significant difference between the resulting compound fraction at the surface and in the bulk layer, a small contribution of sputtered particles from below would not visibly change the results.)

Figure 7.9 shows the compound fraction in the surface layer at increasing nitrogen gas flow, as resulting from the model. For these calculations, a sticking coefficient $S = 0.3$ of molecular nitrogen at the metallic fraction of the surface has been assumed. The difference between the outer target center and the centerline of the race track results from the radial variation of the ion bombardment. The above mentioned sudden change of the process regime is observed at both positions. However, at the outer target center the target poisoning starts at a reactive gas flow around 0.4 sccm, whereas it is significantly delayed at around 0.75 sccm in the race track. Furthermore the compound formation saturates quickly in the target central region, whereas there is a smoother increase in the race track. The calculated curves of figure 7.9 are in qualitative agreement with the experimental findings. They confirm that in a range of sufficiently low reactive gas flow, compound and metallic fractions may co-exist on the target surface. Safi [12] and Schiller et al. [103] already mentioned a differential poisoning of a magnetron cathode by introducing laterally varying balance situations for oxidation and sputtering rates.

Quantitatively, the results of the calculations suggest a minor poisoning also in the race track (between 5% and 25% for reactive gas flows between 0.55 sccm and 0.75 sccm. This is not in disagreement with the results displayed in figure 7.7(a), as a small compound fraction cannot be identified in the EDF's, with the sputter yield from the compound being substantially reduced.

Figure 7.10 shows the compound fraction θ at the outer target center, as derived from the experimental Ti yields of figure 7.8, according to

$$\theta = \frac{(I_C/Y_C)}{(I_C/Y_C) + (I_M/Y_M)} \quad (7.13)$$

where I_C and I_M denote the integrated yields from the compound and metallic fractions, respectively (as indicated by the light-grey and dark-grey areas in figure 7.8), and Y_C and Y_M the respective Ti sputtering yields. In the simplest approximation, the partial sputtering yields scale with the atomic fraction of the respective element and the inverse of the surface binding energy [28]. In accordance with the above, this results in $Y_C/Y_M = 0.5 \cdot (4.9/7.7) = 0.32$. This estimate, however, neglects differences of the collision cascade dissipation in the metallic and compound target fractions. Therefore, the sputter yields have alternatively been calculated by binary-collision computer simulation using the TRIDYN [51, 104] program for 350 eV Ar+ bombardment. (The addition of nitrogen has been neglected here. The main reactive ion species is N_2^+ , which dissociates upon impinging the surface. As the experiment is performed in constant current mode, a fraction of full-energy Ar atoms is thus replaced by two half-energy nitrogen atoms. This introduces only a small error as the nitrogen addition is small.) The results are $Y_M = 0.45$ and $Y_C = 0.07$ so that the quotient

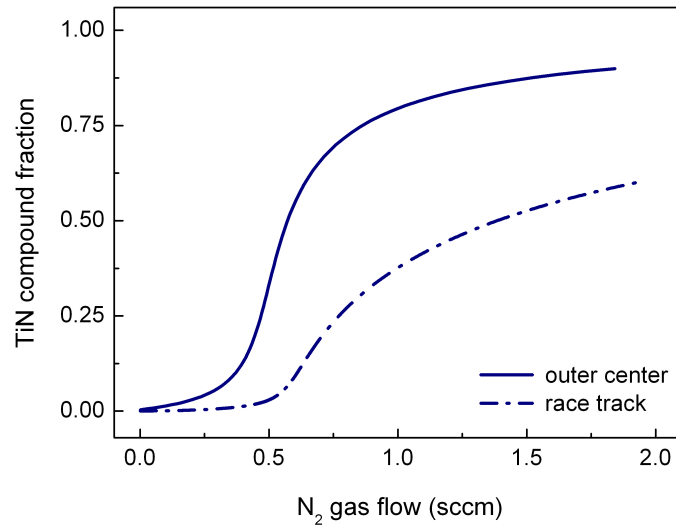


Figure 7.9: Compound fraction at the target surface versus N₂ gas flow as obtained from the analytical model assuming a N₂ sticking of $S = 0.3$, for the target race track (dashed-dotted line) and outer target center (solid line) positions.

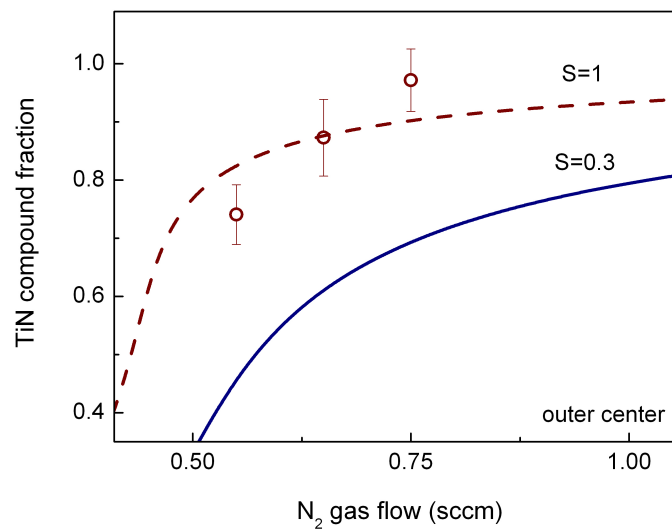


Figure 7.10: Calculated compound fractions (symbols) versus N₂ gas flow for the outer target center, as derived from the experimental yields of Ti sputtered from the outer target center (see figure. 7.8), and as calculated with the analytical model for N₂ sticking $S = 0.3$ (solid line) and $S = 1$ (dashed line). The compound fractions were calculated using TRIDYN values for the sputtering yield.

$Y_C/Y_M = 0.16$ deviates significantly from the above estimate. It should be noted that this reduction of the sputter yield by a factor of ~ 6 between metallic and compound mode is in good agreement with experience [18] (see also figure 3.9).

Figure 7.10 shows the experimental results obtained from equation 7.13 with the above relative sputtering data. The indicated maximum error of $\sim 15\%$ of the experimental data reflects only the error from the decomposition fits of the EDF, and neglects any other uncertainties involved in the experiments and their evaluation. Alternatively, a deviation from unity of the nitrogen zero-coverage sticking coefficient S has been admitted. Literature data of S , which have been derived from rather indirect experiments [64, 65], scatter between ~ 0.1 and 0.8 , with a mean value of ~ 0.3 . The latter is also given in reference [64] as the zero-coverage limit of a dependence on the coverage. Thus, the target coverage was also modeled with $S = 0.3$, in comparison to $S = 1$.

It can be seen that the target compound fraction, which is derived from the experimental yields, I_C and I_M , and TRIDYN relative sputtering data, is in good agreement with the modeled compound fraction, if unity sticking at the metallic surface is assumed for N_2 . The most probable literature value $S = 0.3$ for the N_2 sticking reduces the simulated target coverage by around 30%. In this view, one might be tempted to discard a non-unity zero-coverage sticking of nitrogen molecules. This, however, would hardly be justified in view of the simplicity of the analytical surface model and the experimental uncertainties. Nevertheless, the results confirm the predictive power of the flux-balance model with a radially varying ion current at the sputter target. On the other hand, the above decomposition of the measured EDF's appears to be convincing in spite of the numerous steps of the data handling and the corresponding uncertainties.

The evolution of nitrogen surface coverage in dependence on the nitrogen gas flow as shown in figure 7.10 is in qualitative agreement with the results of ion beam analysis. In accordance the nitrogen incorporation in the target race track, shown in figure 6.1 on page 69 increases abruptly at a reactive gas flow of 0.55 sccm and saturates at ≥ 1.5 sccm. The measured saturated nitrogen areal density of $\sim 1 \cdot 10^{16} N \text{ cm}^{-2}$ is associated there with the formation of a stoichiometric TiN layer, whereas in the non-saturated region a sub-stoichiometric layer is assumed. This picture can be validated now by the findings of figure 7.10. A coverage $\theta \leq 1$ in the non-saturated region derived from both, experiment and model calculations again confirms the presence of a sub-stoichiometric TiN layer on the target surface, which becomes stoichiometric at higher nitrogen gas flows. The target coverage in figure 7.10 remains below 1 even in the saturated region, which still corresponds to a slightly sub-stoichiometric layer. This however is due to the fact, that only the topmost surface layer is modeled, which is, in spite of the bulk material, mainly affected by sputter erosion. The ion beam analysis in figure 6.1 shows the nitrogen uptake of the whole target.

8 Conclusions

In the present work the reactive sputtering process was characterized by means of ion beam analysis (IBA) and energy-resolving mass spectrometry. For the investigations a planar circular magnetron was used for sputtering of titanium in the presence of nitrogen as reactive gas. The titanium-nitride system was chosen only as an example amongst the various material combinations, which are possible to demonstrate the characteristics of the reactive sputtering process. The experimental equipment was arranged in a way that enables both the real-time, *in-situ* ion beam analysis of the target and mass spectrometry.

In a first step plasma properties were analyzed by means of energy-resolving mass spectrometry and simple global plasma modeling. From the latter a quantification of the various particle fluxes towards the sputter target has been obtained. It can be concluded that the target is primarily affected by the thermal kinetic flux of reactive gas molecules, whereas the flux of ionized molecules and reactive gas radicals is of minor importance for the target poisoning. The amount of nitrogen radicals within the plasma was also investigated by ionization threshold spectrometry. The measurements confirm the results of plasma modeling, thus a radicals to molecules ratio of $N^0/N_2 \sim 0.08$ can be stated. The ion bombardment of the target at usually reactive gas additions is generally dominated by the inert gas (argon) ions. As an important plasma parameter, a plasma potential of ~ 4 V was obtained from the measurement of energy distributions of sputtered titanium by means of the energy resolving mass spectrometer.

Besides the particle fluxes, which were mainly obtained from the plasma simulations, further input quantities for the modeling of the reactive sputtering process are necessary. Therefore the plasma-target interaction was simulated additionally by the TRIDYN program. From these simulations input parameters as the reactive gas surface penetration depth and the different sputtering yields for the argon and xenon bombardment of the pure titanium and titanium nitride surface, respectively, were derived.

The existing model of reactive sputtering which includes all known mechanisms of plasma-target interaction was extended. The inclusion of an ion current distribution, which was derived from the erosion profile of a sputter target, allows to calculate absolute reactive gas concentration profiles across the target as function of the applied reactive gas flow into the deposition chamber. In addition, the model predicts the behavior of the reactive gas partial pressure and e.g. the deposition rates. With the modified model an over all very good agreement between experiment and simulation was achieved.

In a comparison between reactive sputtering with the inert gases argon and xenon, it was found from both, experiment and simulation, that the nitrogen incorporation for the Xe/N₂ gas mixture is with $\sim 0.9 \cdot 10^{16}$ N/cm² lower than using an Ar/N₂ mixture, where the incorporated concentration is $\sim 1 \cdot 10^{16}$ N/cm². In view of the higher applied voltage during Xe/N₂ sputtering this result is in contrast to expectations. However from modeling results, it can be concluded that sputter erosion is enhanced for Xe/N₂ sputtering due to a lower energy transfer in the xenon-nitrogen system and due to a higher Xe⁺/N₂ ratio in the Xe/N₂ discharge.

The measured nitrogen incorporations for both, sputtering in Ar/N₂ and in Xe/N₂ gas mixture, clearly exceed the value for one adsorbed monolayer and proofs that reactive gas implantation into the target surface takes place. Further the nitrogen concentration in the target saturates at a value, which correspond to the concentration of stoichiometric TiN of a layer thickness of 2.5 nm. From this it can be concluded, that nitrogen which is not chemically bound in the target diffuses out very quickly. Experiments with the magnetron (plasma) switched off shown, that there is no further mobile fraction of nitrogen in the target.

A laterally resolved ion beam analysis of nitrogen incorporation in the target show a significant variation of target poisoning across the target surface during reactive magnetron sputtering of TiN, which depends on the reactive gas admixture. For typical conditions of practical applications with a reactive gas addition of a few percent, the nitrogen incorporation in the race track may be reduced by almost 50 % compared to the target center and edge. Again the experimental results are consistent with the modeling of the local particle balance. The known mechanisms of plasma target interaction such as ion implantation, reactive gas adsorption in combination with recoil implantation and sputter erosion are confirmed as the main mechanisms of establishing the local target composition in the stationary state. In particular adsorption of nitrogen molecules connected with recoil implantation can be identified as primarily contribution for target poisoning. For modeling without this mechanism the characteristic profile of incorporated nitrogen across the surface can not be observed.

In order to broaden the understanding of poisoning mechanisms, sputtered particles have been investigated by energy resolving mass spectrometry. With this technique it was demonstrated that the ionization and the energy distributions of sputtered neutrals are influenced by the inhomogeneity of the magnetron discharge. An increased fraction of ions with a higher kinetic energy arrives at the substrate position within the central, unbalanced part of magnetron discharge. This effect is ascribed to an increased plasma potential and to an ambipolar acceleration of ions within this discharge region.

Additionally a significant energy shift in the EDF's has been observed associated with target poisoning during reactive sputtering. From this it can be concluded, that in addition to ion beam analysis the surface composition of the target in terms of the metallic or compound fraction can be also characterized by mass spectrometry.

The surface composition varies laterally, which is reflected by the energy distributions of the sputtered particles. The results are interpreted in terms of laterally different states of target poisoning, which results in a variation of the surface binding energy. In accordance to IBA it is demonstrated, that for sufficiently low reactive gas flows, a metallic fraction

within the center erosion zone may still exist whereas the residual target is poisoned. This shows that the adsorption/erosion balance is shifted towards erosion within the target race track and that adsorption as major poisoning mechanism is suppressed there.

The surface binding energy changes depending on the surface composition of the target. The EDF's were decomposed into a fraction originating from the metallic part and compound part of target surface, respectively. This decomposition supports the picture of discrete surface binding energies rather than a continuous transition from the metallic to the compound phase. This is in contraction to previous assumptions see e.g. reference [57]. Again the reactive gas target coverage as derived from the sputtered energy distributions is in reasonable agreement with predictions from model calculations.

As an outlook, target poisoning should be investigated more detailed depending on changed conditions for the adsorption of reactive gas molecules (N_2). Chau et al. observed the formation of volatile oxides at the surface of the hot target at very high target temperatures during reactive sputtering of silicon (1500 K) and niobium (2300 K). [105] Billard et al. later also investigated the influence of target temperature on the reactive sputtering process. [106] It was found there, that an increased temperature yields a stabilization of the discharge within the transition between metallic and compound sputtering mode. Further the possibility of high rate deposition of stoichiometric films in the metallic sputtering mode has been observed for hot target sputtering. A lower target poisoning is attributed, due to a lower accumulation of reactive species at the target. However, Billard described the effect as "paradoxically" since: "...an increase in the desorption kinetics as the target temperature rises..., is expected to play a minor role owing to the kinetics of the sputtering phenomenon."

Thus, in view of the results of the present work, where adsorption of reactive gas molecules in combination with recoil implantation was found to play a major role during target poisoning, the influence of target temperature on reactive sputtering process should be analyzed systematically. It can be expected that a higher target temperature increases the desorption rate of adsorbed reactive gas molecules, which finally reduces the target poisoning.

9 Appendix

9.1 Abbreviations

A	area, ampere
\vec{B}	magnetic field
CVD	Chemical Vapor Deposition
DC	Direct Current
d	thickness, distance
E	kinetic energy
EDF	Energy Distribution Function
ESA	Electrostatic Analyzer
\vec{E}	electric field
e, q	elementary charge
Φ_P	plasma potential
ΔH^S	sublimation enthalpy
IBA	Ion Beam Analysis
I_t	target current
j	current density, flux
k_B	Boltzmann constant
l	liter
λ_D	Debye length
n	atomic density
m	mass
μ	magnetic moment
Ω	solid angle
p	pressure
PVD	Physical Vapor Deposition
PAPVD	Plasma Assisted Physical Vapor Deposition
Q	reactive gas consumption
RF	Radio Frequency
r_L	Larmor radius
RT	Race Track
ρ	density
S	sticking coefficient
sccm	standard cubic centemeter, 1 sccm = 1 cm ³ at p=101325 Pa, T=298,15 K

SEEC, γ	Secondary Electron Emission Coefficient
SIMS	Secondary Ion Mass Spectroscopy
σ	cross section
T	temperature
TCO	Transparent Conductive Oxide
θ	compound fraction
U^S	surface binding energy
V_t	target voltage
W	kinetic energy
$Y(s)$	(sputtering) yield
Y_{mm}	sputter yield metal from metallic surface
Y_{mc}	sputter yield metal from compound surface
Y_{gc}	sputter yield gas from compound surface
Y_r	recoil implantation yield of gas into surface

9.2 Target temperature during magnetron operation

Due to the applied magnetron power of 100 W a heat flow \dot{Q} of towards the target of ≈ 75 W can be assumed [107]. The resulting target temperature T_t can be estimated by the equation:

$$\frac{\partial Q}{\partial t} = \lambda \frac{A}{d} (T_t - T_w) \quad (9.1)$$

where $\lambda=0.22$ W cm⁻¹K is the heat conductivity of Ti, $A=20$ cm² is the target area, $d=0.6$ cm denotes the target thickness and T_w is the temperature on the water cooled backside of the target. Inserting these values in equation 9.1 and assuming $T_w = 293$ K to be at room temperature, yields in a target temperature of $T_t \approx 303$ K.

9.3 Typical process parameters during magnetron operation

Table 9.1: Applied parameters during sputter deposition

Deposition parameter	Value
base pressure	$5 \cdot 10^{-6}$ Pa
operating pressure	0.3 Pa
inert gas flow	10 sccm
reactive gas flow	1 .. 3 sccm
pumping speed (turbo pump)	60 l/s
target current (constant)	0.3 A
target voltage	330-360 V
magnetron power	≈ 120 W

9.4 Simulation parameters

Table 9.2: Simulation parameters used in section 3.3.5

Parameter	Value
Figure 3.9 , parameters - current distribution	
gas temperature	580 K
argon partial pressure p_{ar}	0.3 Pa
pumping speed	60 ls ⁻¹
target area	0.002 m ²
substrate area	0.28 m ²
target current	300 mA
N_2 sticking coefficient S_t	1
Y_{mm}	0.45
Y_{mc}	0.07
Y_{gc}	0.28
Y_r	0.53
Figure 3.10 , differing parameters - variable pumping speed	
pumping speed	30 ls - 90 ls ⁻¹
substrate area	0.15 m ²
Figure 3.11 , differing parameters - variable sticking coefficient	
pumping speed	60 ls ⁻¹
target area	0.002 m ²
substrate area	0.15 m ²
N_2 sticking coefficient S_t	0 and 1

List of Tables

3.1	Electron-impact reactions with their threshold energies	39
3.2	Atomic and molecular species taking part in plasma surface interaction at the target, with their approximate incident energies and the corresponding interaction process.	44
6.1	Comparison of parameters, which are used for modeling of nitrogen areal densities versus nitrogen gas flow, displayed in figure 6.1	70
9.1	Applied parameters during sputter deposition	100
9.2	Simulation parameters used in section 3.3.5	101

List of Figures

2.1	Classification of space and laboratory plasmas	9
2.2	Energy distribution function of plasma particles	11
2.3	Electron impact ionization cross section for different noble gases	14
2.4	Spatial variation of magnetic field and particle motion	19
2.5	Qualitative behavior of sheath and pre sheath in contact of a wall	20
2.6	Interaction of ions with a surface	25
2.7	Schematic of an ion track and ion projected range	27
2.8	Schematic of saturated implantation depth profile	28
2.9	Energy distribution of sputtered atoms according to the Thompson formula .	29
2.10	Sticking coefficient as a function of compound fraction θ	31
2.11	Paschen law of the breakdown	34
2.12	Schematic of a planar cylindrical DC magnetron	34
2.13	Schematic of the hysteresis behavior of reactive magnetron sputtering.	38
3.1	Cross section for electron impact ionization and dissociation of Ar and N ₂ , respectively	40
3.2	Gas kinetic fluxes (Ar and N ₂) of plasma produced species	42
3.3	Lateral variation of particle fluxes	43
3.4	Ion current density along the target radius	44
3.5	Static ion range distribution of plasma species incident on TiN	46
3.6	Nitrogen depth profiles at increasing total ion fluence	47
3.7	Definition of target and substrate regions including various particle fluxes . .	48
3.8	Nitrogen recoil distribution	52
3.9	Modeling of partial pressure (b) and Ti sputter rate (a) for a homogeneous and inhomogeneous ion current distribution across the target	56

3.10	Modeling of partial pressure at different values of pumping speed	57
3.11	Nitrogen areal density (a) and compound (TiN) (b) fractions at Ti target vs reactive gas flow as obtained from the two layer model.	59
4.1	Experimental Setup	61
4.2	Pumping speed of the turpo pump versus valve aperture	61
5.1	Setup and geometry of magnetron target, particle detector and ion beam . .	63
5.2	NRA spectrum	63
5.3	Schematic view of the HIDEN EQP mass spectrometer	65
6.1	Stationary nitrogen areal densities for sputtering in Ar/ N_2 and Xe/ N_2 atmosphere	69
6.2	Radial distributions of the ion current and of the nitrogen areal density at the target surface at different nitrogen flows	72
6.3	Ratio of nitrogen injection by direct ion implantation and recoil implantation	74
7.1	Cross section of the magnetron target and the appearance of the plasma (schematic drawing).	76
7.2	The typical mass spectrum measured in RGA mode during and without magnetron operation.	77
7.3	N_2^+ energy distribution functions at different N_2 -flow	78
7.4	Ti energy distribution functions at different magnetron powers (a) and determination of plasma potential (b)	80
7.5	Detection of N radicals by threshold ionization mass spectrometry	82
7.6	Energy distributions of Titanium sputtered from the target center and the race track	86
7.7	Energy distribution of sputtered titanium neutrals measured at different flow rates of nitrogen.	88
7.8	Energy distribution of sputtered titanium neutrals (open circles) measured at different flow rates of nitrogen, decomposed into two contributions.	91
7.9	Calculated compound fractions versus N_2 gas flow for the race track and outer target center.	93
7.10	Calculated compound fractions versus N_2 gas flow (outer target center) . . .	93

Bibliography

- [1] W. Grove, On the electro-chemical polarity of gases, *Phil. Trans. Roy. Soc. (London)* 142 (1852) 87–101.
- [2] P. J. Kelly, R. D. Arnell, Magnetron sputtering: a review of recent developments and applications, *Vacuum* 56 (2000) 159–172.
- [3] J. M. Schneider, S. Rhode, W. Sproul, A. Matthews, Recent developments in plasma assisted physical vapour deposition, *J.Phys. D: Appl. Phys.* 33 (2000) R173–R186.
- [4] P. E. Hovsepian, D. B. Lewis, W. D. Münz, Recent progress in large scale manufacturing of multilayer/superlattice hard coatings, *Surface and Coatings Technology* 133 (2000) 166–175, 41.
- [5] R. F. Bunshah, *Handbook of Deposition Technologies for Films and Coatings: Science, Technology and Applications*, 2nd Edition, Noyes Publications, 1994.
- [6] B. Chapman, *Glow Discharge Processes: Sputtering and Plasma Etching*, John Wiley & Sons Inc, 1980.
- [7] R. Haefer, *Oberflächen- und Dünnschicht-Technologie, Teil I, Beschichtung von Oberflächen*, Springer Verlag, Heidelberg, New York, 1987.
- [8] D. M. Mattox, *Handbook of Physical Vapor Deposition (PVD) Processing: Film Formation, Adhesion, Surface Preparation and Contamination Control*, William Andrew Publishing, 1998.
- [9] W. D. Sproul, New routes in the preparation of mechanically hard films, *Science* 273 (1996) 889–892.
- [10] S. Schiller, G. Beister, W. Sieber, Reactive high rate d.c. sputtering: Deposition rate, stoichiometry and features of TiO_x and TiN_x films with respect to the target mode, *Thin Solid Films* 111 (1984) 259–268.
- [11] S. Schiller, U. Heisig, C. Korndörfer, G. Beister, J. Reschke, K. Steinfeldler, J. Strümpfel, Reactive d.c. high-rate sputtering as production technology, *Thin Solid Films* 33 (1987) 405–423.
- [12] I. Safi, Recent aspects concerning dc reactive magnetron sputtering of thin films: A review, *Surface and Coatings Technology* 127 (2-3) (2000) 203–219, 87.

- [13] I. Petrov, A. Myers, J. E. Greene, J. R. Abelson, Mass and energy-resolved detection of ions and neutral sputtered species incident at the substrate during reactive magnetron sputtering of Ti in mixed Ar+N₂ mixtures, *Journal of Vacuum Science & Technology A* 12 (5) (1994) 2846–2854, 52.
- [14] A. A. Voevodin, P. Stevenson, C. Rebholz, J. M. Schneider, A. Matthews, Active process-control of reactive sputter deposition, *Vacuum* 46 (7) (1995) 723–729, 20.
- [15] D. Severin, O. Kappertz, T. Kubart, T. Nyberg, S. Berg, A. Pflug, M. Siemers, M. Wuttig, Process stabilization and increase of the deposition rate in reactive sputtering of metal oxides and oxynitrides, *Applied Physics Letters* 88 (16) (2006) 3, 9.
- [16] T. Larsson, H.-O. Blom, C. Nender, S. Berg, A physical model for eliminating instabilities in reactive sputtering, *Journal of Vacuum Science & Technology A* 6 (1988) 1832–1836.
- [17] T. Nyberg, S. Berg, U. Helmersson, K. Hartig, Eliminating the hysteresis effect for reactive sputtering processes, *Applied Physics Letters* 86 (16) (2005) 3, 6.
- [18] S. Berg, H. O. Blom, T. Larsson, C. Nender, Modeling of reactive sputtering of compound materials, *Journal of Vacuum Science & Technology A* 5 (2) (1987) 202–207, 12.
- [19] S. Berg, T. Nyberg, Fundamental understanding and modeling of reactive sputtering processes, *Thin Solid Films* 476 (2) (2005) 215–230, 25.
- [20] M. Liebermann, A. Lichtenberg, *Principles of Plasma Discharges and Materials Processing*, John Wiley & Sons, Inc., New York, 1994.
- [21] D. Rapp, P. Englander-Golden, Total cross sections for ionization and attachment in gases by electron impact. I. positive ionization, *Journal of Chemical Physics* 43 (1965) 1464–1479.
- [22] P. T. Smith, The ionization of helium, neon, and argon by electron impact, *Physical Review* 36 (1930) 1293–1302.
- [23] B. L. Schram, F. Deheer, M. Vanderwi, J. Kistemak, Ionization cross sections for electrons (0.6-20 keV) in noble and diatomic gases, *Physica* 31 (1) (1965) 94, 36.
- [24] G. Franz, *Kalte Plasmen*, Springer-Verlag, Berlin, Heidelberg, New York, 1990.
- [25] M. Nastasi, *Ion-Solid Interactions: Fundamentals and Applications*, Cambridge University Press, 1996.
- [26] P. Sigmund, On number of atoms displaced by implanted ions or energetic recoil atoms, *Applied Physics Letters* 14 (3) (1969) 114.
- [27] P. Sigmund, Theory of sputtering. I. Sputtering yield of amorphous and polycrystalline targets, *Physical Review* 184 (2) (1969) 383.
- [28] R. Behrisch, *Sputtering by Particle Bombardment*, Springer-Verlag, 1981.

- [29] M. W. Thompson, The energy spectrum of ejected atoms during the high energy sputtering of gold, *Philosophical Magazine* 18 (1968) 377 – 414.
- [30] S. J. Lombardo, A. Bell, A review of theoretical-models of adsorption, diffusion, desorption, and reaction of gases on metal-surfaces, *Surface Science Reports* 13 (1-2) (1991) 1–72.
- [31] P. Kisliuk, The sticking probabilities of gases chemisorbed on the surfaces of solids, *Journal of Physics and Chemistry of Solids* 3 (1-2) (1957) 95–101, 21.
- [32] P. Kisliuk, The sticking probabilities of gases chemisorbed on the surfaces of solids .2, *Journal of Physics and Chemistry of Solids* 5 (1-2) (1958) 78–84, 22.
- [33] C. Li, J. H. Hsieh, Effects of variable sticking coefficients on the stability of reactive sputtering process, *Journal of Physics D* 37 (2004) 1065–1073.
- [34] S. Kadlec, J. Musil, W. D. Münz, G. Hakanson, J. E. Sundgren, Reactive deposition of TiN films using an unbalanced magnetron, *Surface and Coatings Technology* 39 (1-3) (1989) 487–497, 22.
- [35] J. L. Vossen, S. Krommenhoek, V. A. Koss, Some experiments that provide direct visualization of reactive sputtering phenomena, *Journal of Vacuum Science & Technology A* 9 (3) (1991) 600–603, 16 Part 1.
- [36] S. Schiller, U. Heisig, K. Steinfelder, J. Strümpfel, W. Sieber, Reactive d.c. high-rate sputtering with the magnetron-plasmatron for industrial applications, *Vakuum-Technik* 30 (1) (1981) 3–14, 0.
- [37] A. Rizk, S. B. Youssef, S. K. Habib, Glow-discharge characteristics when magnetron sputtering copper in different plasma atmospheres operated at low input power, *Vacuum* 38 (2) (1988) 93–95.
- [38] T. Larsson, H. O. Blom, C. Nender, S. Berg, N, A physical model for eliminating instabilities in reactive sputtering, *Journal of Vacuum Science & Technology A* 6 (3) (1988) 1832–1836, 9 Part 2.
- [39] S. Kadlec, J. Musil, H. Vyskocil, Hysteresis effect in reactive sputtering - a problem of system stability, *Journal of Physics D* 19 (9) (1986) L187–L190, 7.
- [40] H. C. Straub, P. Renault, B. G. Lindsay, K. A. Smith, R. F. Stebbings, Absolute partial and total cross sections for electron-impact ionization of argon from threshold to 1000 eV, *Physical Review A* 52 (2) (1995) 1115.
- [41] H. C. Straub, P. Renault, B. G. Lindsay, K. A. Smith, R. F. Stebbings, Absolute partial cross sections for electron-impact ionization of H₂, N₂, and O₂ from threshold to 1000 eV, *Physical Review A* 54 (3) (1996) 2146.
- [42] P. C. Cosby, Electron-impact dissociation of nitrogen, *Journal of Chemical Physics* 98 (12) (1993) 9544–9553, 50.
- [43] W. Möller, D. Güttler, Modeling of plasma-target interaction during reactive magnetron sputtering of TiN, *JAP* 102 (094501) (2007) 1–11.

- [44] M. Lewis, D. Glockner, J. Jorne, Measurement of secondary electron emission in reactive sputtering of aluminium and titanium nitride, *Journal of Vacuum Science & Technology A* 7 (1989) 1019–1024.
- [45] D. Hasselkamp, *Particle Induced Electron Emission II*, Springer-Verlag, 1992.
- [46] S. Kadlec, C. Quaeys, G. Knuyt, L. M. Stals, Energy-resolved mass spectrometry and monte carlo simulation of atomic transport in magnetron sputtering, *Surface and Coatings Technology* 97 (1-3) (1997) 633–641, 20.
- [47] J. Neidhardt, L. Hultman, B. Abendroth, R. Gago, W. Möller, Diagnostics of a N₂/Ar direct current magnetron discharge for reactive sputter deposition of fullerene-like carbon nitride thin films, *Journal of Applied Physics* 94 (11) (2003) 7059–7066, 33.
- [48] F. Debal, J. Bretagne, M. Jumet, M. Wautelet, J. P. Dauchot, M. Hecq, Analysis of d.c. magnetron discharges in Ar-N₂ gas mixtures. comparison of a collisional-radiative model with optical emission spectroscopy, *Plasma Sources Science & Technology* 7 (1998) 219–229.
- [49] J. Ziegler, J. Biersack, SRIM version 2008.03, www.srim.org (2008).
- [50] W. Möller, W. Eckstein, *Tridyn*, *Nucl. Instrum. Meth. B* (2) (1984) 814.
- [51] W. Möller, W. Eckstein, *Tridyn - a trim simulation code including dynamic composition changes*, *Nucl. Instrum. Methods Phys. Res. Sect. B* 230 (1-3) (1984) 814–818, 37.
- [52] S. Berg, H.-O. Blom, T. Larsson, C. Nender, Modelling of reactive sputtering of compound materials, *Journal of Vacuum Science & Technology A* 5 (1987) 202–207.
- [53] D. Depla, R. De Gryse, Target poisoning during reactive magnetron sputtering: Part 1: the influence of ion implantation, *Surface and Coatings Technology* 183 (2-3) (2004) 184–189.
- [54] D. Depla, R. De Gryse, Target poisoning during reactive magnetron sputtering: Part 2: the influence of chemisorption and gettering, *Surface and Coatings Technology* 183 (2-3) (2004) 190–195.
- [55] D. Depla, R. De Gryse, Target poisoning during reactive magnetron sputtering: Part 3: the prediction of the critical reactive gas mole fraction, *Surface and Coatings Technology* 183 (2-3) (2004) 196–203.
- [56] D. Güttler, B. Abendroth, R. Grötzschel, W. Möller, D. Depla, Mechanisms of target poisoning during magnetron sputtering as investigated by real-time in situ analysis and collisional computer simulation, *Applied Physics Letters* 85 (25) (2004) 6134–6136.
- [57] D. Rosen, I. Katardjiev, S. Berg, W. Möller, TRIDYN simulation of target poisoning in reactive sputtering, *Nucl. Instrum. Methods Phys. Res. Sect. B* 228 (2005) 193–197.
- [58] T. Kubart, O. Kappertz, T. Nyberg, S. Berg, Dynamic behaviour of the reactive sputtering process, *Thin Solid Films* 515 (2) (2006) 421–424, 8.

- [59] R. Ranjan, J. Allain, M. Hendricks, D. Ruzic, Absolute sputtering yield of Ti/TiN by Ar^+/N^+ at 400-700 eV, *Journal of Vacuum Science & Technology A* 19 (3) (2001) 1004–1007.
- [60] J. F. Ziegler, J. P. Biersack, U. Littmark, *The Stopping and Range of Ions in Solids*, Pergamon, New York, New York, 1985.
- [61] A. Okamoto, T. Serikawa, C, Reactive sputtering characteristics of silicon in an ar-n2 mixture, *Thin Solid Films* 137 (1) (1986) 143–151, 17.
- [62] S. Kadlec, J. Musil, H. Vyskocil, Hysteresis effect in reactive sputtering: a problem of system stability, *J. Phys. D:Appl. Phys.* 19 (1986) 187–190.
- [63] A. Spencer, R. Howson, R. Lewin, Pressure stability in reactive magnetron sputtering, *Thin Solid Films* 158 (1988) 141–149.
- [64] A. K. Gupta, J. H. Leck, Evaluation of titanium sublimation pump, *Vacuum* 25 (8) (1975) 362–372, 18.
- [65] D. J. Harra, Sticking coefficient of nitrogen on titanium films, *J. Vac. Sci. Technol.* 4 (5) (1967) 337, 0.
- [66] J. Tesmer, M. Nastasi, *Handbook of Modern Ion Beam Materials Analysis*, MRS, Pittsburgh, Pennsylvania, 1995.
- [67] R. Jarjis, *Nuclear Cross-Section Data for Surface Analysis*, Vol. 2, University Manchester, Manchester, 1979.
- [68] K. Bethge, Ion beam analysis of nitrogen, *Nucl. Instrum. Methods Phys. Res. Sect. B* B66 (1992) 146–157.
- [69] S. Pellegrino, L. Beck, P. Trouslard, Differential cross-sections for nuclear reactions $^{14}\text{N}(\text{d},\text{p}_5)^{15}\text{N}$, $^{14}\text{N}(\text{d},\text{p}_0)^{15}\text{N}$, $^{14}\text{N}(\text{d},\alpha_0)^{12}\text{C}$ and $^{14}\text{N}(\text{d},\alpha_1)^{12}\text{C}$, *Nucl. Instrum. Methods Phys. Res. Sect. B* B 219-220 (2004) 140–144.
- [70] R. Hippler, S. Pfau, M. Schmidt, K. Schoenbach, *Low Temperature Plasma Physics. Fundamental Aspects and Applications*, Wiley-VCH, Weinheim, Berlin; Weinheim u.a., 2001.
- [71] M. Low, C. Huan, A. Wee, K. Tan, An alternative method for determining the transmission function of secondary ion mass spectrometers, *Nucl. Instrum. Methods Phys. Res. Sect. B* 103 (4) (1995) 482–488, 19.
- [72] D. A. Dahl, Simion for the personal computer in reflection, *International Journal of Mass Spectrometry* 200 (2000) 3–25.
- [73] S. Rosnagel, Deposition and redeposition in magnetrons, *J. Vac. Sci. Technol. A* 6 (1988) 3049–3054.
- [74] I. Petrov, F. Adibi, J. E. Greene, L. Hultman, J. E. Sundgren, Average energy deposited per atom - a universal parameter for describing ion-assisted film growth, *Applied Physics Letters* 63 (1) (1993) 36–38, 27.

- [75] W. M. M. Kessels, F. J. H. van Assche, J. Hong, D. C. Schram, M. C. M. van de Sanden, Plasma diagnostic study of silicon nitride film growth in a remote Ar-H₂-N₂-SiH₄ plasma: Role of n and SiH_n radicals, *Journal of Vacuum Science & Technology A: Vacuum, Surfaces, and Films* 22 (2004) 96–106.
- [76] P. J. van den Oever, J. H. van Helden, J. L. van Hemmen, R. Engeln, D. C. Schram, M. C. M. van de Sanden, W. M. M. Kessels, N, NH, and NH₂ radical densities in a remote Ar-NH₃-SiH₄ plasma and their role in silicon nitride deposition, *Journal of Applied Physics* 100 (2006) 093303–10.
- [77] D. L. Smith, A. S. Alimonda, F. J. von Preissig, Mechanism of SiN_xH_y deposition from N₂-SiH₄ plasma, *Journal of Vacuum Science & Technology B: Microelectronics and Nanometer Structures* 8 (1990) 551–557.
- [78] Y. K. Kim, J. P. Desclaux, Ionization of carbon, nitrogen, and oxygen by electron impact, *Physical Review A* 66 (1) (2002) 12, 31.
- [79] A. Anders, *Handbook of Plasma Immersion Ion Implantation and Deposition*, Wiley & Sons, 2001.
- [80] M. Ohring, *The Materials Science of Thin Films*, Academic Press Inc., U.S., 1992.
- [81] I. Petrov, P. B. Barna, L. Hultman, J. E. Greene, Microstructural evolution during film growth, *Journal of Vacuum Science & Technology A* 21 (5) (2003) 117–128, 102 Suppl. S.
- [82] J. Y. Tsao, E. Chason, K. M. Horn, D. K. Brice, S. T. Picraux, Low-energy ion-beams, molecular-beam epitaxy, and surface-morphology, *Nucl. Instrum. Methods Phys. Res. Sect. B* 39 (1-4) (1989) 72–80, 26.
- [83] K. Müller, Ion-beam-induced epitaxial vapor-phase growth: A molecular-dynamics study, *Physical Review B* 35 (1987) 7906.
- [84] I. Petrov, F. Adibi, J. Greene, L. Hultman, J. Sundgren, Average energy deposited per atom - a universal parameter for describing ion-assisted film growth, *Applied Physics Letters* 63 (1993) 36–38.
- [85] L. Hultman, W. Münz, J. Musil, S. Kadlec, I. Petrov, J. Greene, Low-energy (-100 eV) ion irradiation during growth of TiN deposited by reactive magnetron sputtering - effects of ion flux on film microstructure, *Journal of Vacuum Science & Technology A* 9 (1991) 434–438.
- [86] R. Kelly, On the problem of whether mass or chemical bonding is more important to bombardment-induced compositional changes in alloys and oxides, *Surface Science* 100 (1) (1980) 85–107, 65.
- [87] B. Window, N. Savvides, Charged-particle fluxes from planar magnetron sputtering sources, *Journal of Vacuum Science & Technology A* 4 (2) (1986) 196–202, 23.
- [88] B. Window, N. Savvides, Unbalanced d.c. magnetrons as sources of high ion fluxes, *Journal of Vacuum Science & Technology A* 4 (3) (1986) 453–456, 14 Part 1.

- [89] K. Ellmer, D. Lichtenberger, Plasma diagnostics by energy-resolved quadrupole mass-spectrometry of a reactive magnetron sputtering discharge from an Fe target in Ar-H₂S atmospheres, *Surface and Coatings Technology* 74-5 (1-3) (1995) 586–593, 25.
- [90] R. Roth, J. Schubert, E. Fromm, Process-control of magnetron sputtering of TiN coatings studied by in-situ AES and plasma diagnostics, *sct* 74-5 (1-3) (1995) 461–468, 16.
- [91] S. Kadlec, C. Quaeyhaegens, G. Knuyt, L. M. Stals, Energy distribution of ions in an unbalanced magnetron plasma measured with energy-resolved mass spectrometry, *Surface and Coatings Technology* 89 (1-2) (1997) 177–184, 23.
- [92] Y. Takagi, Y. Sakashita, H. Toyoda, H. Sugai, Generation processes of super-high-energy atoms and ions in magnetron sputtering plasma, *Vacuum* 80 (6) (2006) 581–587, 11.
- [93] S. Mraz, J. M. Schneider, Energy distribution of O⁻ ions during reactive magnetron sputtering, *Applied Physics Letters* 89 (5) (2006) 3, 9.
- [94] J. M. Andersson, E. Wallin, E. P. Munger, U. Helmersson, Energy distributions of positive and negative ions during magnetron sputtering of an Al target in Ar/O₂ mixtures, *Journal of Applied Physics* 100 (3) (2006) 5.
- [95] L. R. Shaginyan, M. Misina, S. Kadlec, L. Jastrabik, A. Mackova, V. Perina, Mechanism of the film composition formation during magnetron sputtering of WTi, *Journal of Vacuum Science & Technology A* 19 (5) (2001) 2554–2566, 28.
- [96] R. Hippler, S. Wrehde, V. Stranak, O. Zhigalov, H. Steffen, M. Tichy, M. Quaas, H. Wulff, Characterization of a magnetron plasma for deposition of titanium oxide and titanium nitride films, *Contributions to Plasma Physics* 45 (5-6) (2005) 348–357, 11.
- [97] S. M. Rosnagel, J. J. Cuomo, W. D. Westwood, *Handbook of plasma processing technology*, Noeyes Publications, Park Ridge, New Jersey, USA, 1990.
- [98] D. Güttler, R. Grötzschel, W. Möller, Lateral variation of target poisoning during reactive magnetron sputtering, *Applied Physics Letters* 90 (263502) (2007) 1–3.
- [99] W. Möller, M. Posselt, TRIDYN-FZR User Manual, Scientific - Technical Report FZR-317, Forschungszentrum Dresden-Rossendorf, 2001.
- [100] D. Rosen, Defining the surface binding energy in dynamic monte carlo simulation for reactive sputtering of compounds, *Vacuum* 80 (9) (2006) 944–948, 16.
- [101] S. Berg, T. Larsson, C. Nender, H. O. Blom, Predicting thin-film stoichiometry in reactive sputtering, *Journal of Applied Physics* 63 (3) (1988) 887–891, 10.
- [102] L. B. Jonsson, T. Nyberg, S. Berg, Target compound layer formation during reactive sputtering, *Journal of Vacuum Science & Technology A* 17 (4) (1999) 1827–1831, 10 Part 2.

-
- [103] S. Schiller, U. Heisig, K. Goedicke, K. Schade, G. Teschner, J. Henneberger, Advances in high-rate sputtering with magnetron-plasmatron processing and instrumentation, *Thin Solid Films* 64 (3) (1979) 455–467, 45.
- [104] W. Möller, W. Eckstein, J. P. Biersack, TRIDYN - binary collision simulation of atomic-collisions and dynamic composition changes in solids, *Computer Physics Communications* 51 (3) (1988) 355–368, 19.
- [105] R. Chau, W. Ho, J. Wolfe, D. Licon, Effect of target temperature on the reactive d.c.-sputtering of silicon and niobium oxides, *Thin Solid Films* 287 (1996) 57–64.
- [106] A. Billard, D. Merces, F. Perry, C. Frantz, Influence of the target temperature on a reactive sputtering process, *Surface and Coatings Technology* 116-119 (1999) 721–726.
- [107] L. Maissel, R. Glang, *Handbook of Thin Film Technology*, McGraw Hill Higher Education, 1970.

Erklärung

Hiermit erkläre ich, dass ich die vorliegende Arbeit

An Investigation Of Target Poisoning During Reactive Magnetron Sputtering

ohne unzulässige Hilfe Dritter und ohne Benutzung anderer als der angegebenen Hilfsmittel angefertigt habe; die aus fremden Quellen direkt oder indirekt übernommenen Gedanken sind als solche kenntlich gemacht. Die Arbeit wurde bisher weder im Inland noch im Ausland in gleicher oder ähnlicher Form einer anderen Prüfungsbehörde vorgelegt.

Die Arbeit wurde am Institut für Ionenstrahlphysik und Materialforschung des Forschungszentrums Dresden-Rossendorf unter der wissenschaftlichen Betreuung von Herrn Prof. Dr. W. Möller angefertigt. Die Promotionsordnung der Fakultät für Mathematik und Naturwissenschaften der Technischen Universität Dresden erkenne ich an.

Dresden, 18. August 2008

Dominik Güttler